UNIVERSITY OF HELSINKI REPORT SERIES IN PHYSICS

HU-P-D196

MAGNETOHYDRODYNAMIC MODELING OF LARGE-AMPLITUDE WAVES IN THE SOLAR CORONA

JENS POMOELL

Division of Geophysics and Astronomy
Department of Physics
Faculty of Science
University of Helsinki
Helsinki, Finland

ACADEMIC DISSERTATION

To be presented, with the permission of the Faculty of Science of the University of Helsinki, for public criticism in auditorium E204 of the Department of Physics (Physicum), Gustaf Hällströmin katu 2a, on Thursday, July 26, 2012, at 12 o'clock noon.

Helsinki 2012

Author's Address: Division of Geophysics and Astronomy
Department of Physics
P.O. Box 64
FI-00014 University of Helsinki
jens.pomoell@helsinki.fi

Supervisors: Docent Rami Vainio, Ph.D.
Department of Physics
University of Helsinki

Dr. Ralf Kissmann
Institute for Astro- and Particle Physics
University of Innsbruck, Austria

Professor Hannu Koskinen, Ph.D.
Department of Physics
University of Helsinki

Pre-examiners: Research Professor Terry G. Forbes, Ph.D.
Institute for the Study of Earth, Oceans and Space
University of New Hampshire, USA

Associate Astronomer Ilia I. Roussev, Ph.D.
Institute for Astronomy
University of Hawai'i at Mānoa, USA

Opponent: Professor Stefaan Poedts, Ph.D.
Centre for Plasma Astrophysics
Katholieke Universiteit Leuven, Belgium

ISBN 978-952-10-8074-6 (printed version)
ISSN 0356-0961
Helsinki 2012
Helsinki University Printing House Unigrafia Oy

ISBN 978-952-10-8075-3 (PDF version)
http://ethesis.helsinki.fi
Helsinki 2012
Electronic Publications @ University of Helsinki (Helsingin yliopiston verkkojulkaisut)

Abstract

Solar eruptions are a consequence of the complex dynamics occurring in the tenuous, hot magnetized plasma that characterizes the solar corona. From a socio-economic viewpoint, solar eruptions can be argued to be the most important manifestation of the magnetic activity of the Sun due to their role as the main drivers of space weather, i.e., conditions in space that can have an adverse impact on space- as well as ground-based technologies such as telecommunication, electric power systems and satellite navigation.

The launch of new space-based solar observatories during the past two decades has resulted in a dramatic improvement of the instrumentation monitoring the inner heliosphere. In spite of the advances in the observational capabilities, the physics of the solar eruptions as well as the nature of the various transient large-scale coronal phenomena observationally associated with the eruptions remain elusive. Constructing models capable of simulating the coronal and heliospheric dynamics is a viable path for gaining a more complete understanding of these phenomena.

This thesis is concerned with developing a simulation tool based on the magnetohydrodynamic (MHD) description of plasmas and employing it for studying the characteristics of large-scale waves and shocks launched into the solar corona by the lift-off of a solar eruption such as a coronal mass ejection (CME). A particular focus is on discussing the role of large-amplitude waves in producing transient phenomena such as EIT waves and solar energetic particle (SEP) events that are known to appear in conjunction with CMEs.

A suite of MHD models of the solar corona are constructed that allow the study of the coronal dynamics in varying environments at several stages of the eruption. For this purpose, novel robust numerical methods for solving the equations of magnetohydrodynamics in orthogonal curvilinear geometries in multiple dimensions are derived, forming the basis of the numerical simulation tool developed for the thesis.

The results show that a dynamically intricate global shock front degenerating to a fast-mode MHD wave towards the surface of the Sun is an essential and natural part of the eruption complex that plays a key role in the generation of eruption-related transient phenomena. For instance, the close resemblance between the on-disk signatures produced by the fast-mode wave and EIT waves suggest a wave interpretation of the latter. The simulations also reveal that a highly non-trivial evolution of the shock properties on coronal field lines occurs even for simple coronal conditions, highlighting the need for more sophisticated models of particle acceleration than generally used so far. The results of the thesis are of particular importance for the continuing efforts to construct reliable physics-based models of the inner heliosphere for use in space weather applications.

Contents

Preface **vi**

List of Abbreviations **viii**

1 Introduction **2**

1.1 Goals 3

1.2 Thesis structure 3

1.3 Author's contribution 6

2 Observational Overview **8**

2.1 Moreton waves 8

2.1.1 The Uchida model 10

2.2 EIT waves 10

2.2.1 3D morphology and relation to the CME 11

2.2.2 Kinematics and dynamics 13

2.2.3 Shock identification 14

2.2.4 Relation to Moreton waves 15

2.3 White-light coronagraph shock observations 16

2.4 Type II bursts 17

2.5 Energetic particle events 20

3 Modeling Coronal Dynamics **24**

3.1 Governing equations 24

3.2 Model idealizations 25

3.2.1 Background corona model 26

3.2.2 CME model 27
3.2.3 Domain and Geometry 27
3.3 Local modeling 28
3.4 Two-dimensional global modeling 29
3.4.1 Azimuthal symmetry 29
3.5 Towards three-dimensional global modeling 31
3.5.1 Axisymmetric wind solution in three dimensions 32
3.5.2 Event-oriented three-dimensional modeling 32

4 Computational MHD **36**
4.1 Constructing the FV scheme 37
4.1.1 Alternative discretization methods 41
4.1.2 Reconstruction algorithms 43
4.1.3 Upwinding the numerical flux 45
4.1.4 Time integration 47
4.2 Constrained transport for divergence-free fields 48
4.2.1 Reconstructing the magnetic field 52
4.3 Extension to curvilinear geometries 53
4.4 The second-order scheme 55
4.5 Further remarks 57
4.5.1 Splitting the magnetic field 58
4.5.2 Employing stretched grids 58

5 Results and Discussion **60**
5.1 Overview of eruption dynamics 60
5.2 Driven vs. blast wave scenario 61
5.3 CME - EIT wave - cavity connection 63
5.4 Dependence on heating formulations 65
5.5 Comparing 3D and axisymmetric simulations 67
5.6 Implications for particle acceleration 70

6 Conclusions **72**
6.1 Summary and conclusions 72
6.2 Future prospects 73

A Details of the Model Initial Configurations **76**

A.1 Local model 76

A.2 Event-oriented model 78

Bibliography **80**

Preface

The seeds of this work were planted as early as the summer of 2005 when I took my first stumbling steps towards constructing a MHD model of the solar corona as a research assistant at the Division of Theoretical Physics. Over the long years that this thesis has been in the making numerous colleagues and friends have generously assisted and encouraged me, for which I am sincerely grateful. I want to take this opportunity to thank a few of you by name.

First of all, I wish to thank Doc. Rami Vainio for the patience, advice and remarkable understanding of physics (and other matters) that you so willingly have shared – you have certainly set an example for me and others as well. Secondly, I want to thank Dr. Ralf Kissmann for our shared adventures into the dark jungles of numerical MHD. I haven't had nearly as much fun at work as during our collaborations. I thank Prof. Hannu Koskinen for giving me the opportunity to pursue doctoral studies in the field of space plasma physics. I am grateful for your elucidation of the natural science aspect of physics – the reason I got fascinated about physics and started studying it in the first place. I also want to thank Prof. Kai Nordlund for kick-starting my career as a scientist, and introducing me to the art of computational physics.

Our small but dynamic space physics group has been a source of good-spirited discussions and collaboration over the years, for this I wish to thank Dr. Alexandr Afanasiev, Dr. Neus Agueda, Dr. Katerina Andréeová, Heli Hietala, Alexey Isavnin, Dr. Emilia Kilpua and Dr. Arto Sandroos.

Due to the collaborative nature of the projects of the group, I have had the privilege to get acquainted with a number of colleagues, both international as well as national, to whom I owe a debt of gratitude. In particular, I wish to thank PD. Dr. Horst Fichtner for all the support and making me feel welcome during my visits to Bochum, and Dr. Jens Kleimann for our open-hearted discussions of the abstrusities of solar wind modeling. I thank Dr. Felix Spanier and Urs Ganse for all the profound – as well as not so profound – discussions that we have had during the past years. On the national level, Dr. Timo Laitinen and Markus Battarbee have made the visits to Turku both enjoyable and productive. I also want to thank Ilja Honkonen, Dr. Minna Palmroth and the others at the space research group of the FMI for the interest towards my work as well as for the contagious enthusi-

asm. Epitomizing this positive spirit, I want to thank Dr. Riku Järvinen for our discursions into the most varied of topics.

The hours spent at the office, as well as at conferences, would not have been as enjoyable were it not for your good company I have had the fortune of enjoying. In addition to all of you already mentioned, I want to thank fellow officemate Dr. Reijo Keskitalo for the numerous (and sometimes overlong) jogs, Dr. Tomáš Kohout for the uplifting lunches and Dr. Miklos Långvik as well as Marcus Peth for the countless times that you have managed to divert my thoughts from work-related matters during working hours. Moreover, I want to thank my fellow students and friends at the Kumpula campus for the many invaluable shared experiences.

Finally, I thank my family for the continuing support and encouragement. My greatest dept of gratitude is reserved for my wife Anna and to our Saga and Liam – you are my reflections of reality.

In spite of all the great people I have had the privilege to work with, this project would not have been possible without extensive financial support from several sources. Funding from the Magnus Ehrnrooth Foundation, the Vilho, Yrjö and Kalle Väisälä Foundation, the Finnish Graduate School in Astronomy and Space Physics, the Academy of Finland and the University of Helsinki Funds, is gratefully acknowledged.

Jens Pomoell
Kilo, 27th of June, 2012

List of Abbreviations

AIA	Atmospheric Imaging Assembly
AR	Active region
AU	Astronomical unit
CFD	Computational fluid dynamics
CH	Coronal hole
CME	Coronal mass ejection
CT	Constrained transport
CCT	Consistent constrained transport
EIT	Extreme ultraviolet Imaging Telescope
EUV	Extreme ultraviolet
EUVI	Extreme Ultraviolet Imager
FD(M)	Finite Difference (Method)
FV(M)	Finite Volume (Method)
GONG	Global Oscillation Network Group
HLL	Harten-Lax-van Leer
LASCO	Large Angle and Spectrometric Coronagraph Experiment
MHD	Magnetohydrodynamics
ODE	Ordinary differential equation
PDE	Partial differential equation
PFSS	Potential field source surface
RK	Runge-Kutta
SDO	Solar Dynamics Observatory
SEP	Solar energetic particle
SOHO	Solar and Heliospheric Observatory
SSP	Strong Stability Preserving
ST(A/B)	STEREO (Ahead / Behind)
STEREO	Solar Terrestrial Relations Observatory
TVD	Total variation diminishing
WENO	Weighted essentialy non-oscillatory
WSA	Wang-Sheeley-Arge

Chapter 1

Introduction

The space-based solar observatories of the digital age have unveiled the outermost regions of the solar atmosphere to be a theater of dynamic activity on a large variety of spatial and temporal scales driven by the energy stored in the coronal magnetic field. Indeed, by virtue of its proximity, the Sun offers a unique possibility to study the fundamental physics governing astrophysical plasmas by enabling in situ measurements of the emitted plasma in the vicinity of the Earth in addition to imaging and spectrographic observations of the solar source regions.

Yet, the strive to reach a quantitative understanding of the dynamical nature of the solar activity is not only of academic interest. Solar flares and coronal mass ejections, the most energetic explosions occurring in the solar system, are the main actors behind space weather, i.e., conditions in space that can have an adverse effect on the performance of space-borne or ground-based technological systems and that can endanger human life or health. The path towards reliable space weather forecasts is intimately tied to advancements in our knowledge of the physical processes operating in solar eruptions.

A variety of transient phenomena are commonly observed in the solar corona during the lift-off of coronal mass ejections (CMEs), such as propagating large-scale wave-like disturbances observed in extreme ultraviolet images, radio bursts at various wavelengths as well as solar energetic particle events. Despite the incredible detail and quality of the data produced in particular by the latest generation of space-based observatories, the exact nature and cause of the various observed coronal disturbances remain veiled and an active topic of research. Nevertheless, it is clear that erupting CMEs induce large-amplitude waves in the solar corona during the lift-off process that influence the coronal environment. Therefore, the nature of the waves and shocks produced by evolving CMEs is a key topic in the efforts to understand the physics behind eruption-associated phenomena. This is also the topic of this thesis.

The task at hand is made complicated by the fact that many of the parameters needed in order to test current theories of the phenomena are generally not known

from observations. A viable path to overcome this fundamental difficulty is to construct models capable of describing the coronal dynamics. Due to the complexity of the coronal system it is, however, difficult to construct realistic models without resorting to numerical calculations. Therefore, the purpose of this thesis is to develop a simulation tool capable of describing the dynamical response of the corona to eruptive events.

1.1 Goals

The main goal of this thesis is to develop a magnetohydrodynamic simulation code applicable to solar eruptions. The main objectives can be summarized as follows:

- Develop robust numerical methods for solving the equations of magnetohydrodynamics (MHD) that can accurately resolve shocks as well as smooth flows in Cartesian as well as in spherical geometries.
- Construct a range of coronal models of various complexity starting from highly idealized Cartesian two-dimensional models. Idealized models are important for studying the essential processes at play in the corona. Also, the performance of the numerical methods can be assessed with such modeling.
- Study the effect of shocks interacting with coronal structures in a global setting that includes a solar wind solution. Identify sites and geometries favorable for generating energetic particles.
- Study waves and shocks in a complex coronal environment based on a specific event. Compare the shock structure and on-disk wave features with observed extreme ultraviolet imagery.

1.2 Thesis structure

The contents of this thesis are divided into two parts: the introduction or synthesis part and the original research articles.

The synthesis part is organized into five chapters and one appendix. Chapter 2 presents an observational overview of a selection of the various coronal transient phenomena that are believed to be intimately connected to shocks and/or large-amplitude large-scale waves in the corona. In chapter 3 the magnetohydrodynamic models considered in this work are presented. Preceding the description of the various model configurations, the governing equations as well as the basic assumptions of the models are elucidated. Chapter 4 provides an account of

the computational methods used for numerically solving the equations. The main results of the numerical experiments are presented and discussed in chapter 5. Finally, chapter 6 provides a short summary and the main conclusions of the thesis. Additionally, details of the new modeling not included in the attached articles are given in the Appendix.

The second part of the thesis consists of five research articles published in peer-reviewed journals. The majority of the work presented in the introduction part is based on the research material described in the articles. There is, however, also new original work presented in the introduction part. The novel, previously unpublished material is:

- The formulation of a numerical scheme of arbitrary order in curvilinear coordinates, presented in section 4.3, as an extension of the second-order scheme derived in Article IV and Article V.
- The two-dimensional local modeling in a different parameter regime complementing the modeling in Article I. This is presented in section 3.3 and discussed in section 5.2 together with the novel confined eruption simulation.
- The three-dimensional modeling introduced in section 3.5 and discussed in section 5.3 and section 5.5.

The included articles are:

Article I

Pomoell J., Vainio R. and Kissmann R., *MHD Modeling of Coronal Large-Amplitude Waves Related to CME Lift-off*, Solar Physics, 253 (1), p. 249-261, 2008

Summary: A two-dimensional magnetohydrodynamic model is used to study the waves and shocks induced by the lift-off of a CME. The initial equilibrium configuration consisting of a high-density flux rope filament in a gravitationally stratified ambient corona with a quadrupolar magnetic field is made to erupt by an artificial force acting on the plasma inside the flux rope. The line-of-sight emission measure is analyzed as well the kinematics, morphology and plasma parameters of the induced shock structure.

Article II

Pomoell J., Vainio R. and Kissmann R., *MHD Simulation of the Evolution of Shock Structures in the Solar Corona: Implications for Coronal Shock Acceleration*, Astrophysics and Space Sciences Transactions, 7 (3), p. 387-394, 2011

Summary: A two-dimensional azimuthally symmetric MHD model employing spherical coordinates is used to study the dynamics of shocks caused by an erupting CME in a solar minimum-like corona including a solar wind solution. A heating term that retains an adiabatic polytropic index and at the same time producing

the same steady-state solar wind solution obtained by a constant non-adiabatic polytropic index is derived. Favorable sites for particle acceleration are assessed by comparing to results of test particle simulations employing a simplified shock model.

Article III

Pomoell J. and Vainio R., *Influence of Solar Wind Heating Formulations on the Properties of Shocks in the Corona*, Astrophysical Journal, 745 (2), p. 151-159, 2012

Summary: Using two-dimensional azimuthally symmetric models, the effect of the heating prescription applied in two popular solar wind models on the dynamics of shocks is studied. This is done by comparing the results with the dynamics in models with identical steady-state solar wind solutions by employing an equivalent heating formulation that retains the Rankine-Hugoniot relations of adiabatic ideal MHD. The heating formulation is a generalization of the one used in Article II.

Article IV

Kissmann, R., Pomoell J. and Kley, W., *A Central Conservative Scheme for General Rectangular Grids*, Journal of Computational Physics, 228 (6), p. 2119-2131, 2009

Summary: A semidiscrete finite volume method to solve hyperbolic conservation laws using arbitrary orthogonal curvilinear coordinates is derived. The numerical algorithm is constructed in a manner so that the order of the scheme is not fixed during the derivation, opening the possibility for high-order extensions. The performance of the scheme is elucidated by performing numerical experiments on a second-order scheme in cylindrical coordinates explicitly constructed from the general framework.

Article V

Kissmann, R. and Pomoell J., *A Semidiscrete Finite Volume Constrained Transport Method on Orthogonal Curvilinear Grids*, SIAM Journal on Scientific Computing, 34 (2), p. A763-A791, 2012

Summary: The framework of Article IV is extended to solving the evolution of divergence-free vector fields in orthogonal curvilinear coordinates using the constrained transport method. By doing so, the desired upwind and nonoscillatory characteristics of the scheme of Article IV are carried over to the constrained transport solver. The accuracy of the scheme is demonstrated by applying the method to a suite of numerical test problems familiar from the literature, an emphasis being on the solution of the equations of magnetohydrodynamics.

1.3 Author's contribution

The research conducted in this thesis was done in close collaboration with the author's supervisors Dr. Rami Vainio (RV) and Dr. Ralf Kissmann (RK). The topics of Articles I-III were worked out together with RV, and with RK in the case of Articles IV-V.

All the simulation runs conducted in Articles I-III as well as the runs presented in the introduction part in this thesis were done by the author (JP). The simulation code used for producing the results in Articles II and III as well as for the new runs presented in the introduction was written solely by JP. Also the implementation of these models was done by JP. The code used for Article I was provided by RK, although new features needed for that study were added by JP. Also, RK aided in setting up the initial condition considered in Article I. The writing of Articles I-III was mainly done by JP.

The derivation of the numerical methods presented in Articles IV-V was done in a collaborative effort with RK. The bulk of the articles was written by RK. Also, most of the simulation runs were produced by RK. JP produced the advection tests in section 3.2 in Article V.

Chapter 2

Waves and Shocks in the Corona: Overview of Observations

From a basic theoretical viewpoint, any perturbation in a medium will cause a propagating disturbance to be initiated. Following such a train of thought, it is natural to conjecture that the impulsive energy release associated with solar eruptive phenomena such as flares, CMEs and filament eruptions should launch waves and shocks that propagate in the solar corona.

A patchwork of evidence to support this claim has been accumulating since the mid 1940s following the discovery of type II radio bursts (Payne-Scott et al., 1947, Wild and McCready, 1950) as well as the observation of the activation of distant filaments by flares (Dodson, 1949). Indeed, type II bursts remain one of the primary observational signatures of shocks propagating in the corona.

The launch of new high-cadence space-based solar observatories in the 1990s ignited a renaissance in observations of coronal waves following the direct imaging of global propagating wave-like disturbances at extreme ultraviolet (EUV) wavelengths. *EIT waves* (section 2.2) continue to be intensely studied with the debate about their exact physical nature remaining active. Indications of shocks and waves have been observed in other wavelengths as well, including the X-ray and optical regimes, providing further input on the characteristics of the coronal waves.

In this chapter, a short overview of the observational indications of large-amplitude waves and shocks in the corona is presented.

2.1 Moreton waves

The first direct imaging observations of large-scale propagating disturbances in the solar atmosphere were reported by Moreton (1960) and Moreton and Ramsey

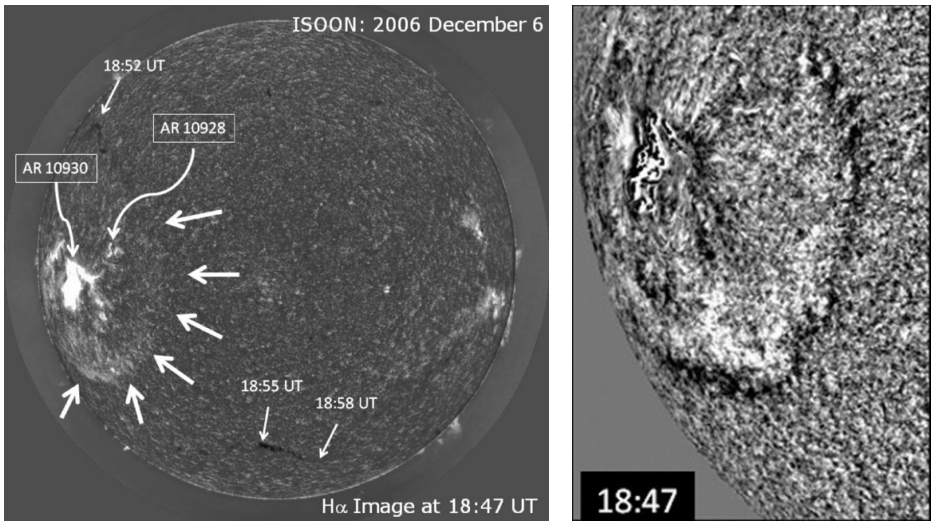

Figure 2.1: Left: Enhanced Hα image clearly showing the Moreton wave front. Smaller arrows indicate positions of filaments disrupted by the wave, a common phenomena observed in conjunction with Moreton waves. Right: red-wing minus blue-wing doppler image. Both images from Balasubramaniam et al. (2010).

(1960) using the Hydrogen Alpha (Hα) cinematograph at the Lockheed Solar Observatory. Dubbed *Moreton waves*, they appear as propagating arc-shaped fronts in the centerline as well as in the wings of the Hα spectral line. Reviews of their observational characteristics are provided, for instance, by Svestka (1976), Warmuth (2007).

The Moreton waves exhibit a directional bias propagating most often within a rather restricted angular sector of $\sim 100°$. Often appearing circular and rather sharp in the first images, the perturbation becomes more irregular and diffuse as it travels, often no longer traceable at distances of ~ 300 Mm from the source active region (AR) (Warmuth, 2007). Only more recently have a few cases of global propagation been reported (e.g., Muhr et al., 2010, Balasubramaniam et al., 2010). Figure 2.1 shows the unusually large and pronounced wave front observed on 6 December 2006 discussed by Balasubramaniam et al. (2010).

The speed of the Moreton wave is typically in the range of $\sim 500-1500$ km/s, and generally shows a deceleration of the order of ~ 1 km/s^2 (Warmuth et al., 2004). In a well-observed event, the disturbance was observed to accelerate from the initial speed of 400 km/s up to 1100 km/s after which a deceleration started (Temmer et al., 2009). Encountering ARs, the wave fronts experience refraction and reflection, effectively avoiding strong magnetic field concentrations. When encountering a coronal hole (CH), the disturbance generally stops at the CH boundary. Transmission into the CH has also been observed (Veronig et al., 2006).

When discussing the general characteristics of Moreton waves, it is important to

keep in mind that they are observed rather infrequently: for example, for the entire solar cycle 23 (1997–2006), only 27 events have been reported (Warmuth, 2010).

A particularly interesting feature of the Moreton wave is revealed by intensity changes in the wings of the line: the leading edge of the wave front is observed in emission in the blue wing and in the centerline, but in absorption in the red wing. With the Hα line forming in the chromosphere, the feature has been suggested to be "caused by an invisible agency depressing the chromosphere" (Moreton, 1964). Furthermore, a second fainter front following the first with reversed intensity changes is also often seen, suggesting a subsequent relaxation of the compressed chromosphere (Warmuth, 2007). Such a feature is seen in the December 6, 2006, event as shown in the right panel of Fig. 2.1.

2.1.1 The Uchida model

Guided by the characteristic up-down swing of the front as well as the fact that the wave speeds in the chromosphere are much slower than the Moreton wave, Uchida (1968) suggested that the wave actually propagates in the corona. Thus, he constructed the so-called 'sweeping skirt' model in which the Moreton wave is just the chromospheric signature of a fast magnetosonic MHD wave or shock propagating through the corona and sweeping the chromosphere. The model naturally accounts for several of the wave characteristics, for instance the up-down oscillation is explained by the refraction of the wave packets downwards eventually reaching the surface, and the avoidance of regions with high Alfvén speed as well as the narrow angular spans similarly due to refraction of the ray paths. Uchida's freely propagating (non-linear) fast-mode MHD hypothesis remains the only model put forth to explain Moreton waves. In order to confirm the theory, a detection of propagating large-scale coronal fast-mode waves is needed.

2.2 EIT waves

Already during the first CME watch campaign of the Solar and Heliospheric Observatory (SOHO), images of coronal large-scale wave-like disturbances traveling over significant fractions of the solar disk were captured by the Extreme-ultraviolet Imaging Telescope (EIT) (Moses et al., 1997). To acknowledge the instrument responsible for the landmark discovery, they are often (but not universally: for a discussion on terminology, see Zhukov, 2011) referred to as *EIT waves*. The first more detailed reports (Thompson et al., 1998, 1999) characterize the phenomena as a large, bright diffuse wave traveling across the solar disk quasi-radially away from the eruption site at a speed of a few hundred km/s in a non-homogeneous fashion, being most pronounced in quiet-Sun regions and less observable near strong magnetic features. Indeed, exhibiting such properties, it

was immediately proposed that the EIT waves could be the signature of the long-sought coronal fast-mode wave predicted by Uchida's model of Moreton waves.

Rather than solidifying the initial interpretation the continuous data stream of the EIT instrument and, as a consequence, the rapid growth of the number of observed events led to the discovery of several puzzling features contesting the wave picture. In particular (e.g., Chen, 2011): (1) If the EIT waves really are the coronal counterparts of the Moreton waves, why are they typically a factor two to three slower and why is their morphology typically so different (broad and diffuse vs. sharp and arc-like)? Furthermore, how can the speed in some cases be smaller than that of the coronal sound speed? (2) Why are the EIT wave velocities not correlated with the velocity of type II bursts if they indeed are shocks? (3) Why does the EIT wave front at times stop at magnetic separatrices?

Fueled by such arguments, a number of alternative interpretations have been proposed. Common for the *pseudo-wave* models is that the observed disturbance is not a wave at all, but instead a signature of phenomena related to the expansion of the eruption complex and its interaction with the surroundings. More recently, a *hybrid* interpretation has emerged as an attempt to reconcile the two opposing views, suggesting that both wave and non-wave components can be present simultaneously. In-depth discussions of the various models and their shortcomings with respect to the observed properties of the disturbances, primarily from the SOHO/EIT-era, have been provided by several authors (e.g., Warmuth, 2007, Vršnak and Cliver, 2008, Wills-Davey and Attrill, 2009, Warmuth, 2010, Gallagher and Long, 2011, Zhukov, 2011, Warmuth, 2011) and will not be repeated here.

As elucidated in the works mentioned above, a major reason for the lingering controversy can be attributed to the inadequacies of the EIT as an instrument for observing fast coronal phenomena, primarily due to the low cadence of the instrument, being at best 12 minutes. Also the lack of inner coronagraph data as well as the availability of observations from only a single vantage point significantly encumber the interpretation of events observed solely by SOHO. With the next generation of space-based observatories now operational, new high-cadence multi-viewpoint observations have become available drastically improving the observational capabilities. A particularly important recent result is the unambiguous identification of a global large-amplitude wave launched and subsequently separating from the erupting CME, strongly suggesting a hybrid interpretation of the various wave-like disturbances observed. In the following, a selection of these recent results utilizing the new facilities are presented. A thorough review of recent results has been complied by Patsourakos and Vourlidas (2012).

2.2.1 3D morphology and relation to the CME

With the launch of the twin Solar Terrestrial Relations Observatory (STEREO) spacecraft, near-simultaneous observations from multiple vantage points has be-

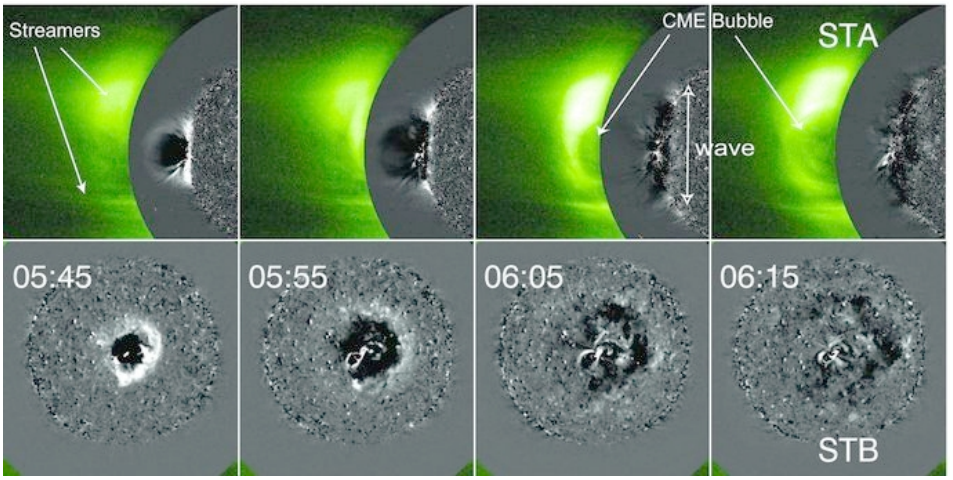

Figure 2.2: Composite of STEREO-A/COR-1 total brightness and STEREO-A/EUVI 195 Å running difference (RD) images (top) as well as STEREO-B/EUVI 195 Å RD images (bottom) (Patsourakos and Vourlidas, 2009).

come available. A particularly striking example of the importance of such data for analyzing EIT waves is provided by the event of February 13, 2009, detailed by Patsourakos and Vourlidas (2009) as well as by Kienreich et al. (2009). Figure 2.2 shows the development of the wave and the CME observed on-disk with the source at the very center of the solar disk in the field of view (FOV) of the Extreme Ultraviolet Imager (EUVI) on STEREO-B, while appearing as a limb event for the COR1 and EUVI instruments on STEREO-A being in near-perfect quadrature with STEREO-B. The EUV data reveal a set of erupting loops giving rise to a propagating bubble-like feature preceded by a wave-like disturbance, with the time of the wave onset coinciding with the time of fast CME lateral expansion. From roughly 05:45 UT onwards, the extent of the wave becomes clearly larger than that of the bubble, and appears to propagate freely. Entering the COR1-A FOV, the EUV bubble and CME cavity are seen to be the same structure, and the the flanks of the CME map accurately to the EUV dimmings around the AR. Furthermore, Kienreich et al. (2009) determine that the bulk of the EUV emission of the wave originates from a height of $\sim 80 - 100$ Mm above the solar surface.

This set of observations clearly shows that the CME ejection and EIT wave, while initially connected, later on decouple to become separate, distinguishable phenomena. The separation of the wave from the ensuing CME has since been observed in remarkable detail for several off-limb events in which the full dome of the wave is visible (e.g., Veronig et al., 2010, Ma et al., 2011, Cheng et al., 2012). In particular the Atmospheric Imaging Assembly (AIA) instrument on board the Solar Dynamics Observatory (SDO) spacecraft provides unprecedented opportunities for such studies by providing images with a cadence of $\sim$ 12 s in seven EUV passbands. Figure 2.3 displays AIA 193 Å observations of the June 13,

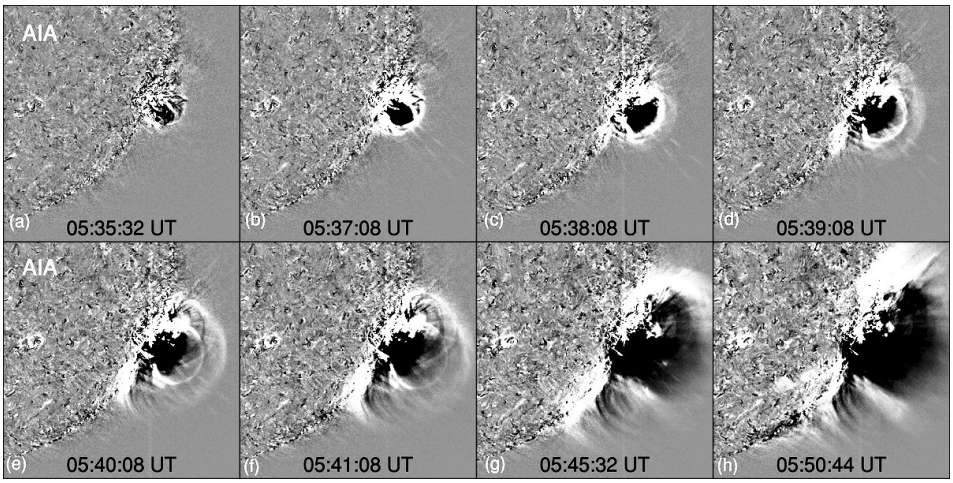

Figure 2.3: Contrast-enhanced SDO/AIA 193 Å base difference images obtained on June 13, 2010. Adapted from Ma et al. (2011).

2010, event in which a sharp dome-shaped structure is seen to separate from the CME bubble, and subsequently attains a much larger lateral extent than that of the dimming region. Furthermore, the perfect connection of the dome to the wave signatures on the disk is evident.

2.2.2 Kinematics and dynamics

Detailed information of the kinematics and shape of the EIT wave pulse is vital for a full understanding of the phenomena. With the availability of high-cadence data as well as the development of automated or semi-automated feature detection methods, high-fidelity measurements of the pulse characteristics have become possible.

Long et al. (2011) analyze the kinematics of the August 14, 2010, event observed by both SDO/AIA as well as STEREO-A/EUVI. In both data sets, the pulse is found to show significant deceleration. The constant acceleration and initial velocity deduced from the EUVI 195 Å data are, however, significantly lower (by a factor of ~ 4.5 and ~ 1.2, respectively, as compared to the AIA 193 Å result presented in Table 1 in (Long et al., 2011)), suggesting a strong influence of the lower cadence of the EUVI instrument. In the AIA data, the kinematics are found to depend on the pass band studied, with an inverse relation between the speed and acceleration and the peak formation temperature of the pass band. The authors interpret this as evidence for the pulse having a higher velocity in cooler and denser plasma which they argue indicates compression. Furthermore, clear pulse broadening indicating dispersion is observed in both data sets. These kinematic properties all suggest a wave interpretation of the phenomena.

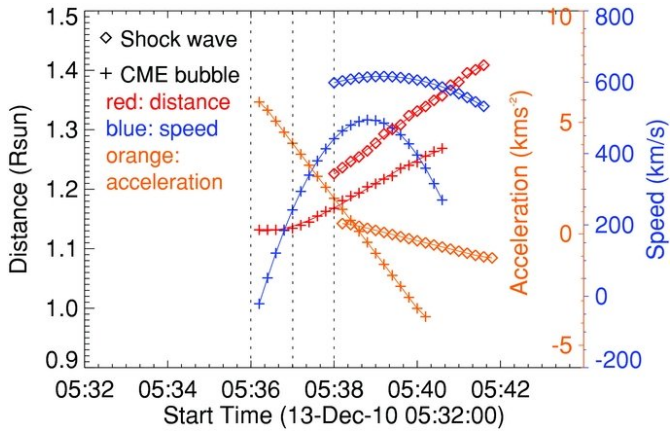

Figure 2.4: Kinematics of the wave and bubble of the June 13, 2010 event derived from stacked plots of 193 Å intensity along a Sun-centered radial slit (Ma et al., 2011).

Strong deceleration of the EIT wave has also been reported for the case when the wave is observed above the limb, such as in the June 13, 2010, event (Fig. 2.3). The kinematics, derived from a time-distance plot of the 193 Å intensity along a radial line, is shown in Fig. 2.4. When measured along lines parallel to the solar surface, Ma et al. (2011) find the velocity of the wave to depend on height (397 km/s at a height $r = 1.11R_{\odot}$ while 246 km/s at $r = 0.98R_{\odot}$) in addition to being asymmetric in the north-south direction.

On the other hand, the wave is often observed to propagate at an almost constant speed. Kienreich et al. (2011) report on the first observations of four consecutive EIT waves by STEREO-B/EUVI. As all four disturbances were launched from the same AR, propagated in the same direction and had similar appearance as well as angular extent, the authors characterize the waves as begin homologous. Furthermore, all waves propagated with a nearly constant velocity, ranging from 340 km/s for the fastest and 220 km/s for the slowest wave.

2.2.3 Shock identification

Although EIT waves, at least in a number of events, appear to exhibit characteristics reminiscent of large-amplitude waves, determining conclusively whether the disturbance actually is a wave remains difficult. Hints at their nature can be obtained by analyzing the dynamics of the wave pulse characteristics in well-observed events, as for example done in the work of Long et al. (2011) described in the previous section.

In the homologous wave event, Kienreich et al. (2011) find that the perturbation profiles (i.e., the intensity across the wave front relative to a pre-event intensity)

of the four waves in a sector away from the nearby active regions and coronal holes show a strong initial steepening. Then, assuming that the EUV intensity brightening of the wave is primarily due to compression (see also discussion in Zhukov, 2011), the density jump can be estimated as $X = N/N_0 \sim (I/I_0)^{1/2}$. Further, using the Rankine-Hugoniot jump condition for a perpendicular shock and assuming the plasma beta to be $\beta = 0.1$, the magnetosonic Mach numbers can be estimated. Kienreich et al. (2011) find the fastest wave to have Mach number of 1.09 and the slowest 1.04. Indeed, a strong correlation between the estimated Mach number and speed of the waves is found, as expected for a wave interpretation. Also, the low Mach numbers are consistent with the waves not showing a strong deceleration. Therefore, the authors conclude the waves to be low-amplitude fast-mode waves.

For the June 13, 2010 event, Ma et al. (2011) use a different approach to verify their assumption that the EIT wave dome is a shock. First, they obtain the compression ratio r of the shock from the band-splitting of the associated type II radio burst (see section 2.4) and the upstream temperature from the differential emission solutions of the event provided by Kozarev et al. (2011). With the velocity of the (presumed) shock, the upstream sonic Mach number can be determined. Then, assuming the shock to be perpendicular, the temperature jump of the shock can be estimated. The obtained downstream temperature is used to determine the ionization timescales which are, finally, compared with the observed timescales of the intensity ratios 211 Å / 193 Å and 335 Å / 193 Å. The authors find that the two timescales are consistent using the downstream temperature estimated from the Rankine-Hugoniot conditions and, therefore, conclude the dome to be a shock wave.

2.2.4 Relation to Moreton waves

Simultaneous observations of EIT and Moreton waves have the potential of elucidating whether EIT waves indeed are the coronal counterparts of the Moreton waves. Asai et al. (2012) report on such observations using high-cadence Hα imagery and SDO/AIA EUV data for an event that occurred on August 9, 2011. The wave front of the Moreton wave was found to coincide with a sharp EUV wave front appearing as an expanding dome structure, shown in Fig. 2.5. The fronts in both wavelengths initially traveled at a speed of $\sim$ 760 km/s or faster.

While both fronts were found to be directional, the EUV front spanned a larger angle in addition to being visible for a longer period of time. Constructing time-distance plots of the EUV images along three different arcs, the temporal features of the EUV waves were examined. In all three sets, a fast wave-like disturbance is seen. At larger distances from the source, however, the authors find the bright front to rapidly decelerate and disappear whereas the fast front seems to continue. The timing of the separation coincides roughly with the disappearance of the Moreton wave as well as with the encounter of nearby active regions. Finally,

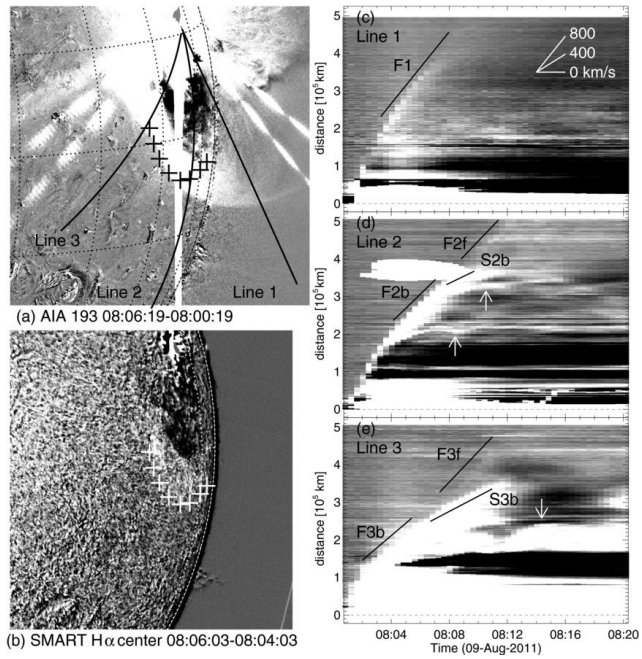

Figure 2.5: Difference images of August 9, 2011 event. Top-left: SDO/AIA 193 Å . Bottom-left: SMART Hα centerline. Right: Time-distance plots along the lines indicated in the top left image (Asai et al., 2012).

a subsequent activation of a distant filament/prominence is noticed, temporally consistent with the fast front interacting with the structure. The conclusion of Asai et al. (2012) is that the EUV wave consists of a fast-mode MHD wave as well as a different slower component that they refer to as a ”typical EIT wave”.

2.3 White-light coronagraph shock observations

Searches for signatures of CME-driven shocks in white-light coronagraph observations have been conducted since the mid 1970s following the deployment of the coronagraph on-board Skylab. Despite the large number of observed CMEs, only more recently have unambiguous shock detections been reported (see Vourlidas and Ontiveros, 2009, for a review).

Bemporad and Mancuso (2010) present a detailed case study of the fast ($v \sim 1750$ km/s) 22 March 2002 event. Figure 2.6 displays SOHO/LASCO-C2 base-differenced images showing an arc-like intensity enhancement preceding the CME front. The deflection of a coronal streamer in the south due to the shock is visible in the rightmost image as a sharp dark streak preceded by a more diffuse brightening.

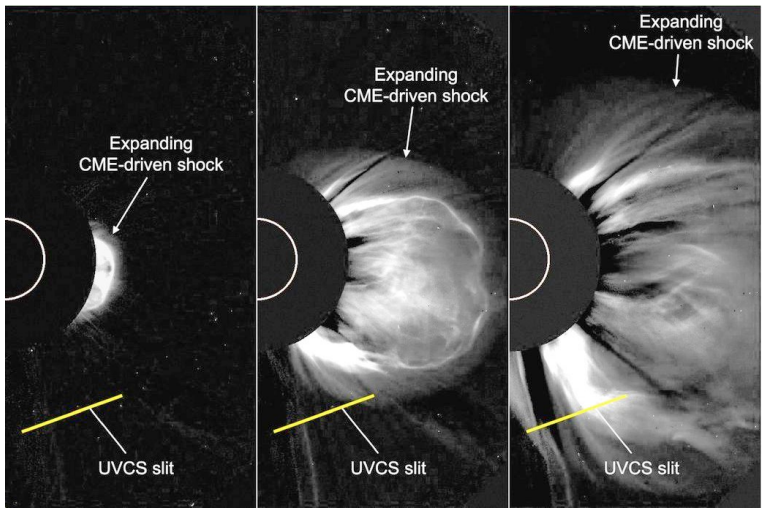

Figure 2.6: Sequence of contrast-enhanced base-difference SOHO/LASCO-C2 images showing the CME event of 22 March 2002. The images are separated in time by 24 minutes with the first image at 11:06 UT. Also shown is the SOHO/UVCS slit position. Adapted from Bemporad and Mancuso (2010).

The white-light shock observations are particularly important in that several parameters of the shock, such as the density compression ratio as well as kinematic parameters, can be inferred. For the March 22, 2002 event, Bemporad and Mancuso (2010) find a value of 2.06 for the density compression. Ontiveros and Vourlidas (2009) studied SOHO/LASCO observations of fast ($v > 1500$ km/s) CMEs that occurred in the ascending phase of solar cycle 23 (1997-1999). Analyzing 15 events satisfying these criteria, shock-like signatures were found in 13 of the events. In 11 of the events, the shock compression ratio could be determined, giving values ranging from 1.2 to 2.8. Also, by fitting the observed shock shape to a three-dimensional bow shock model for three of the events, the direction of the shock could be determined. Recently, Kim et al. (2012) analyzed 10 CME events that showed a clear shock signature in at least three SOHO/LASCO images. Calculating the density compression ratios, they found values in range 1.00-1.91 with the mean being 1.18.

2.4 Type II bursts

Type II radio bursts are identified as narrow-band emission lanes in dynamic radio spectra that slowly drift, typically at rates below 1 MHz/s, towards lower frequencies. Often the bursts show a fundamental-harmonic structure manifested as two emission bands with a frequency ratio $\sim 1 : 2$, although the spectral characteristics are often complex with a variety of observed morphological fine structures

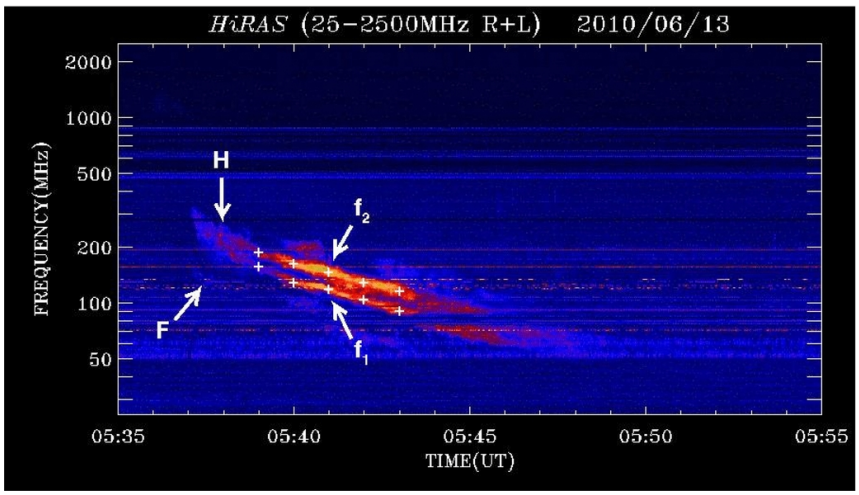

Figure 2.7: Dynamic radio spectra from the Hiraisio Radio Spectrograph (HiRAS) observed on June 13, 2010. The weak fundamental is marked by the capital F, while the harmonic by capital H. Note the clear band-splitting of the harmonic lane (Gopalswamy et al., 2012).

such as band splittings, multiple lanes or fibers as well as so-called herringbones (e.g., Mann et al., 1995, Nindos et al., 2008, for reviews).

Since soon after their discovery, type II bursts have been interpreted as emission at approximately the fundamental and harmonic of the local plasma frequency originating from the vicinity of a shock propagating through the corona and heliosphere. The current picture of the process, supported by *in-situ* observations (Bale et al., 1999), holds that electrons, accelerated at the shock, form beam distributions in the foreshock region that can generate Langmuir waves as a result of the instabilities driven by the beams. The Langmuir waves, in turn, take part in a nonlinear three-wave interaction process leading to emission of the electromagnetic waves of the radio burst (e.g., Knock et al., 2001).

The shocks responsible for generating interplanetary type II bursts occurring at decameter or longer wavelengths are well established to be linked to CMEs propagating in interplanetary space. On the other hand, the origin of the coronal type II bursts at metric wavelengths continues to be a source of controversy. Evidence to support the interpretation of the shock as, on the one hand, an undriven flare-ignited blast wave or, on the other hand, a piston-type shock driven by the CME have been presented in numerous studies (e.g., Pick et al., 2006, Vršnak and Cliver, 2008, Nindos et al., 2011, for references).

The high-cadence EUV imaging observations of the early stages of the eruptions that recently have become available can help in clarifying the role of CMEs in the generation of coronal type II bursts. Figure 2.7 depicts the dynamic spectrum of the June 13, 2010, event that was observed in unprecedented detail by AIA/SDO

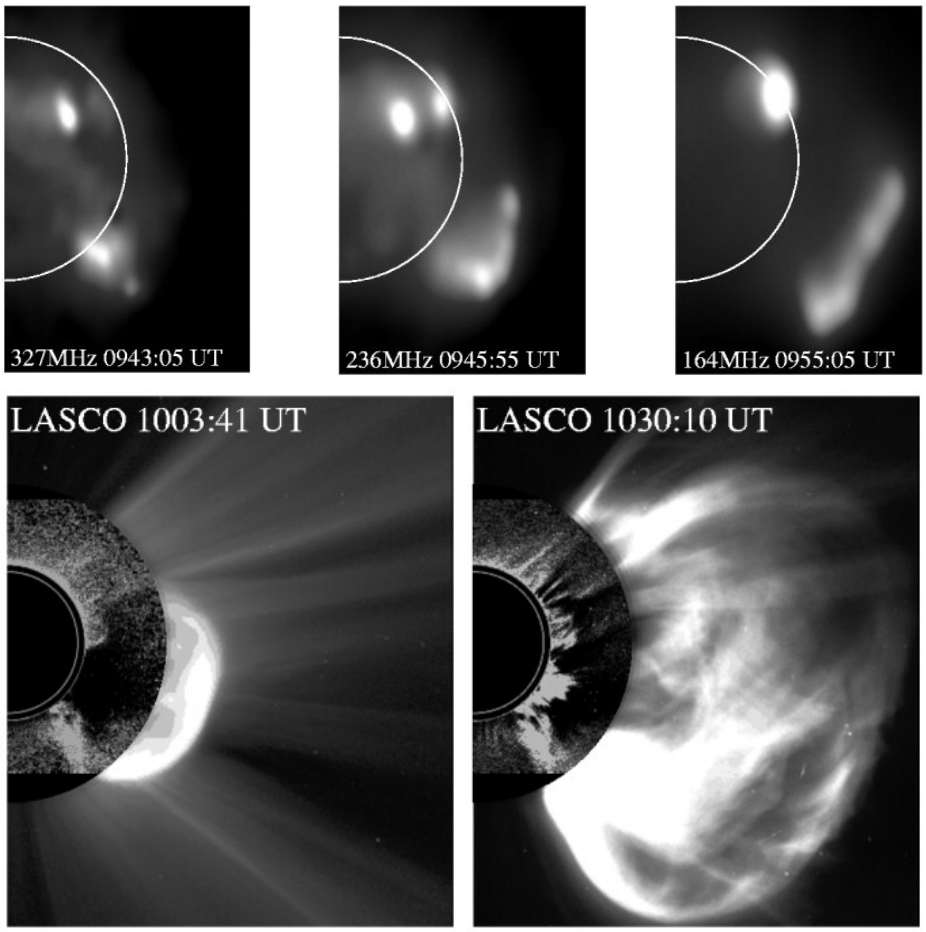

Figure 2.8: Above: Radio emission at three different frequencies at three subsequent times observed by the Nancay radioheliograph (NRH). Below: Combined SOHO/LASCO C1 and C2 images showing the temporal association of the CME. Note the different scaling compared to the NRH images (Maia et al., 2000).

(Fig. 2.3). The fundamental, starting at a frequency of ~ 150 MHz at 05:37 UT, is less visible than the clear harmonic emission. Comparing with the EUV images, it is interesting to note that the start time of the type II coincides with the time that the sharp dome-like structure is first distinctly visible. Furthermore, as registered by Gopalswamy et al. (2012), this also coincides with the rapid lateral expansion phase of the EUV bubble. In at least two other off-limb events has a similar connection between the appearance of the dome and the start of a type II burst been noted (Veronig et al., 2010, Cheng et al., 2012). Combined with imaging observations at radio wavelengths, such connections could be studied directly. Unfortunately, imaging observations of type II bursts are rare, with the 1998 April 20 event shown in Fig. 2.8 being one prominent candidate.

The fine structure of the type II bursts can disclose information of the characteristics of the shock that produced the emission. Especially interesting is the band-splitting feature, in which the emission lane is split into two separate lanes with a frequency difference of 10-20 %. Often, the difference is interpreted as stemming from plasma emission originating from the upstream and the downstream of the shock. If correct, the compression ratio of the shock could be determined for cases in which the band-splitting is visible. In the type II burst associated with the June 13, 2010 event shown in Fig. 2.7, the harmonic lane shows a clear splitting of the band. In this case, the frequency difference implies a compression ratio $r \sim 1.5$ (Gopalswamy et al., 2012). It must be kept in mind that there is no theoretical justification or observational evidence for plasma emission from the downstream region (Cairns, 2011).

2.5 Energetic particle events

The accumulation of observational data of solar energetic particle events in the 1970s and 1980s led to the demise of the "flare myth" and the emergence of a new standard picture, by which SEP events can be divided into two categories: gradual and impulsive (e.g., Reames, 1999, Klecker et al., 2006). According to this paradigm, the two types of events differ in a number of attributes such as size, spatial distribution of the source region, duration as well as compositional signatures. Impulsive events originate from a relatively narrow range of solar longitudes, have durations ranging from hours to a day, are electron-rich and enhanced in heavy ions and the rare ^{3}He isotope, and have higher mean ionic charge states. The gradual events, on the other hand, yield larger particle intensities and fluences, have durations from days to a week, and have ion abundances and charge states comparable to nominal coronal values. Moreover, in this framework, the two event types are related to the likely sites and mechanisms of particle acceleration: impulsive events are believed to be accelerated at sites associated with flares, whereas gradual events are produced by shock waves driven by fast CMEs.

With new instruments with improved collecting power and resolution on-board the armada of spacecraft launched since the early 1990s, data collected during solar cycle 23 have, however, revealed features challenging the standard picture. At energies above a few MeV per nucleon, gradual events exhibit a dramatic event-to-event variability especially in the elemental abundance ratios and charge states. In fact, some gradual events exhibit Fe/O and ^{3}He/^{4}He ratios and mean Fe charge states close to those typically ascribed to impulsive events, thereby questioning the validity of the two-class paradigm.

An example of such high-energy variability is presented in Fig. 2.9 that shows the event-integrated Fe/O ratio of the April 21 and August 24 2002 large SEP events discussed at length in Tylka et al. (2006). While for energies $\sim 0.5 - 10$ MeV per nucleon the ratios are nearly identical, at higher energies the ratios diverge with

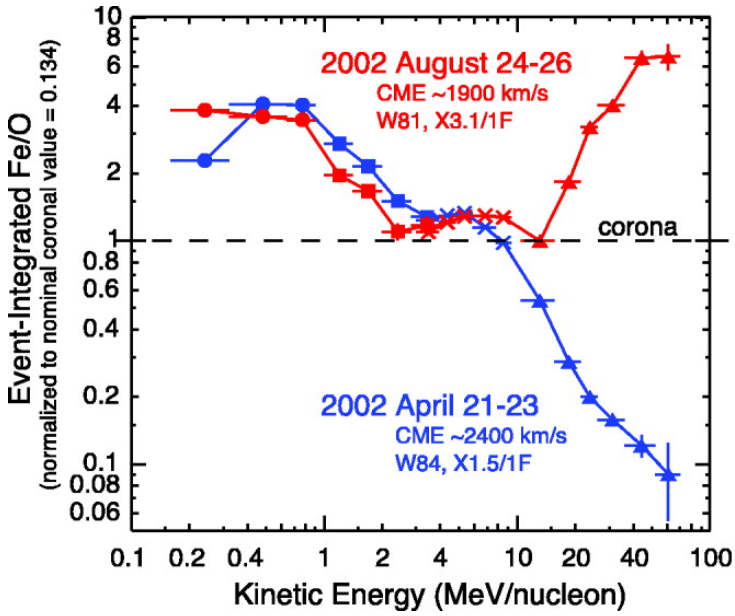

Figure 2.9: Event-integrated Fe/O as a function of energy for the 2002 April 21 (blue) and 2002 August 24 (red) SEP events (Tylka et al., 2006).

the difference being nearly 2 orders of magnitude at ~ 60 MeV/nuc. The energy dependence of the ratio is a reflection of the spectral differences between the two species, as shown in Fig. 2.10: Fe has a softer spectrum than O at high energies in the April event, and vice versa in the August event. The curves in the figure are fits to the data, with the Ellison-Ramaty $F \propto E^{-\gamma} \exp(-E/E_0)$ functional form that includes an exponential cutoff used in the April event, while in the August event a smooth double power law better fits the data.

The fascinating aspect about the two events is that they both arose from seemingly identical solar progenitors: both events were associated with very similar solar flares in terms of their size and solar locations as well as with similarly fast and wide CMEs. Therefore, more subtle effects are likely to be causing the dramatically different high-energy behavior than factors such as CME speed and source location that are generally held important for causing variability of SEP events.

Two plausible explanations have been proposed to account for the unusual characteristics. In the first one, the ions responsible for the flare-like compositional signatures are in fact suggested to be accelerated in a flare occurring during the time of the event. Thus, the event is a combination of a gradual and impulsive event (Cane et al., 2006). The second explanation, extending the picture of the mechanisms of "regular" gradual events, selective acceleration at the CME-driven shock is held responsible for producing the atypical ion enhancements (Tylka et al., 2005). In the phenomenological model of Tylka and Lee (2006), this requires

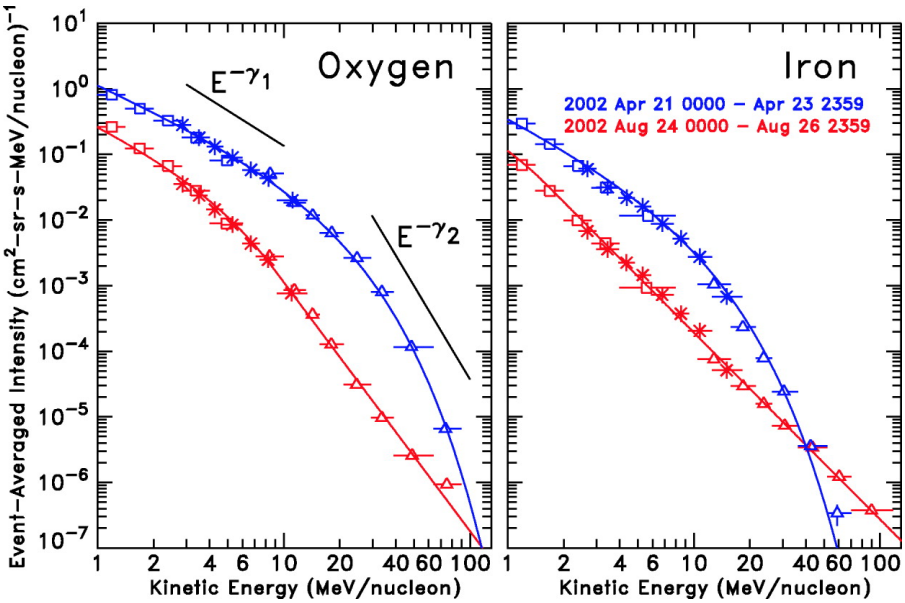

Figure 2.10: Event-averaged oxygen (left) and iron (right) spectra for the 2002 April 21 (blue) and 2002 August 24 (red) events (Tylka et al., 2005).

two essential ingredients to work. First, a compound seed population consisting of energetic ions with properties typical to that observed in impulsive events in addition to the suprathermal population from the corona or solar wind. Presumably, such a impulsive-like population could either be a remnant population from previous flaring activity or a pre-accelerated population originating from the accompanying flare. The second ingredient involves the shock geometry. Generally, for efficient acceleration to occur, quasi-perpendicular shocks require seed particles with higher speeds than quasi-parallel shocks. Therefore, the flare suprathermals are more likely to provide seed particles for quasi-perpendicular shocks, and are selectively accelerated to higher energies than ions from the coronal bulk population. As the shock moves outward and the shock angle decreases, the injection threshold is lowered and the coronal component increasingly dominates the accessible seed population. As a result, the characteristics of the flare suprathermal population is reflected among the higher energy particles. A schematic of the model is shown in Fig. 2.11.

If proven correct, the Tylka and Lee (2006) model has important implications for SEP modeling efforts: new models that consider shock acceleration in less idealized situations with evolving shock obliquity must be constructed. The first steps in such a direction have already been undertaken (e.g., Sokolov et al., 2004, Sandroos and Vainio, 2009a). In fact, applying a test-particle model including diffusive shock acceleration to the Tylka and Lee (2006) scenario, Sandroos and Vainio (2009a) find results that are in good agreement with the semi-empirical model.

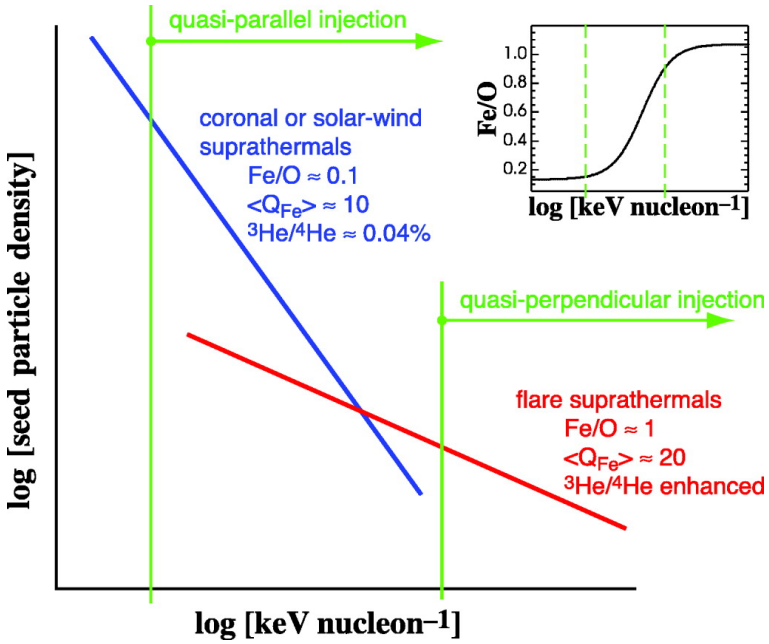

Figure 2.11: Schematic of the Tylka and Lee (2006) model for explaining the high-energy variability of SEPs.

Chapter 3

Modeling Coronal Dynamics

A wealth of observational data, a small fraction of which has been presented in the previous chapter, clearly shows that the solar corona is characterized by a magnetized plasma in which various large-scale large-amplitude wave phenomena are excited following the onset of an eruptive event. Accounting for this fundamental aspect of the nature of the corona is a prerequisite for any theory describing the dynamics of the plasma to be applicable to the study of coronal transient phenomena. In this chapter, the magnetohydrodynamic models considered in this thesis are presented.

3.1 Governing equations

On a general level, in order for any modeling approach of large-scale coronal dynamics to be successful, the model should:

- include a physically self-consistent description of the interaction of the flows with the coronal magnetic fields
- include a physically self-consistent description of waves and shocks
- be given by a set of equations solvable with a reasonable workload for a system of global spatial dimensions

Only then can the model be deemed feasible, at least in principle, for addressing the chief topics of this thesis laid out in section 1.1.

In the widely applied magnetohydrodynamic description, the plasma is treated as a magnetized, electrically conducting continuous fluid. Since the theory can be viewed as an extension of classical hydrodynamics so that the interaction of the fluid with the electromagnetic fields is included, it is evident that the two first

criteria laid out above are satisfied. Further, the third requirement can, to a certain degree, be satisfied by employing numerical methods.

In this thesis, MHD is the plasma theory of choice for studying solar coronal dynamics. Specifically, the ideal MHD realization is applied, in which the plasma flow is assumed to be inviscid, infinitely conductive as well as adiabatic. Although constituting a significant simplification compared to more involved non-ideal, multi-fluid or kinetic descriptions, ideal MHD has the benefit of being a relatively well understood theory that has been studied and applied extensively in a variety of astrophysical settings. Particularly important is the fact that the equations of ideal MHD constitute a set of conservation laws, expressing the conservation of mass, momentum, energy and magnetic flux, and are given by

$$\frac{\partial \rho}{\partial t} + \nabla \cdot (\rho \mathbf{v}) = 0 \tag{3.1}$$

$$\frac{\partial (\rho \mathbf{v})}{\partial t} + \nabla \cdot \left[\rho \mathbf{v}\mathbf{v} + \left(P + \frac{\mathbf{B}^2}{2\mu_0} \right) \mathcal{I} - \frac{1}{\mu_0} \mathbf{B}\mathbf{B} \right] = \mathbf{f} \tag{3.2}$$

$$\frac{\partial E}{\partial t} + \nabla \cdot \left[\left(E + P - \frac{\mathbf{B}^2}{2\mu_0} \right) \mathbf{v} + \frac{1}{\mu_0} \mathbf{B} \times (\mathbf{v} \times \mathbf{B}) \right] = Q + \mathbf{v} \cdot \mathbf{f} \tag{3.3}$$

$$\frac{\partial \mathbf{B}}{\partial t} - \nabla \times (\mathbf{v} \times \mathbf{B}) = 0 \tag{3.4}$$

$$\nabla \cdot \mathbf{B} = 0 \tag{3.5}$$

where ρ is the mass density, $\mathbf{v}$ the velocity field, P the gas pressure, $\mathbf{B}$ the magnetic field and E the total energy density given by

$$E = \frac{1}{2} \rho \mathbf{v}^2 + \frac{P}{\gamma - 1} + \frac{\mathbf{B}^2}{2\mu_0} \tag{3.6}$$

with γ the polytropic index and μ_0 the vacuum permeability. As will be detailed in the forthcoming sections, the system of equations actually considered are those of ideal MHD augmented by specific source terms, namely a force density $\mathbf{f}$ representing additional external forces such as gravity, as well as an extra energy source Q. Also, an ideal gas law given by $P = (\rho/m) k_{\mathrm{B}} T$ where m is the mean molecular mass, k_{B} Boltzmann's constant and T the temperature is invoked in order to obtain the temperature.

3.2 Model idealizations

Given initial and boundary conditions appropriate for the particular problem under study, the complete time evolution of the system governed by the MHD equations can, in principle, be solved using the computational methods presented in the next chapter. When attempting to model the complex coronal dynamics, however, two major difficulties must be dealt with. First, the spatial distribution of the quantities that would be needed in order to construct an initial condition representing

the solar corona at a given time as well as the boundary conditions driving the dynamics are not known from observations. Second, the computational intensiveness of MHD calculations puts severe limitations on the problems currently solvable. Therefore, modeling coronal dynamics necessarily requires a high degree of idealization.

3.2.1 Background corona model

The prevailing practice in most simulations involving coronal dynamics is to begin by seeking a steady-state solution representing the ambient corona. When considering a global solution, this is typically accomplished by starting from some reasonable initial state and solving the MHD equations applying appropriate boundary conditions until an approximate steady-state is reached. The configuration will then include a self-consistently generated solar wind solution. As a further simplification, if a solar wind outflow is not deemed necessary, a static equilibrium solution of the plasma can be sought. Setting $\mathbf{v} = 0$ and including gravity, such a solution of equations Eq. (3.1)-Eq. (3.5) (with $Q = 0$) is obtained when the force balance given by

$$-\nabla P + \mathbf{J} \times \mathbf{B} + \rho \mathbf{g} = 0, \tag{3.7}$$

where $\mathbf{J} = \nabla \times \mathbf{B}/\mu_0$, is satisfied. For a force-free magnetic field, the pressure gradient need only balance the gravity, which can most easily be accomplished by applying the ideal gas law and assuming a given temperature distribution.

When seeking a steady-state solution including a solar wind-like outflow, a fundamental problem is the fact that the mechanisms that heat the solar corona and cause the solar wind to accelerate to the observed velocities have not been unambiguously identified. Therefore, additional measures that supply the required heating need to be included in the model. As shortly reviewed in Article III , most multidimensional MHD models utilize one (or more) of the following strategies:

- Employment of a constant or spatially varying non-adiabatic polytropic index $\gamma < 5/3$
- Addition of explicit momentum and/or energy source terms
- Inclusion of effects due to waves/turbulence

Since such methods rely on ad hoc rates of energy and/or momentum deposition, they should be contrasted with the attempts at physically self-consistent solar wind modeling striving to uncover the basic processes responsible for the observed heating and consequent acceleration (e.g., Hollweg and Isenberg, 2002, Cranmer, 2010, for reviews). Nevertheless, solar wind models using pragmatic heating prescriptions and showing a reasonable agreement with in situ observations at 1 AU have successfully been constructed (e.g., Cohen et al., 2008, Jin et al., 2012).

3.2.2 CME model

In the most generally accepted paradigm (Forbes et al., 2006, and references therein), solar eruptions are caused by a sudden rapid release of magnetic energy that has gradually been built-up in the corona as a result of quasi-static changes of the photospheric magnetic field. A basic premise of such so-called *storage models* is that the magnetic field is *line-tied*, i.e., the photospheric foot-points of the magnetic field lines remain fixed during the course of the eruption. Thus, the only magnetic energy available for driving the eruption is due to currents flowing in the corona. By further assuming the plasma beta to be small, the magnetic field must be nearly force-free, which suggests that the currents in the low corona predominantly flow along the field.

Essentially for this reason (see also discussion in Chen, 2011), the magnetic field configuration for the progenitor of the CME in most dynamic MHD models has been taken to be that of a flux rope. This approach is also employed in the modeling considered in this work. The mechanisms responsible for triggering the energy release and initiating the eruption are, however, still not fully known. Among others, the onset of an ideal-MHD instability or a sudden loss of an equilibrium have been suggested as potential mechanisms for the initiation. Thus, for studies where the primary interest is in studying the dynamics caused by the acceleration or propagation phase of the eruption, the initiation phase is often omitted from the calculations. Instead, highly idealized eruption models are generally employed. A commonly applied method is to superimpose a non-equilibrium configuration on the ambient solution, and will be the method of choice for the global modeling studied in this work.

3.2.3 Domain and Geometry

Restricting the spatial scale of the domain under study as much as possible is necessary in order for the limited number of grid cells of the computational mesh to be able to capture the gradients of the flow variables. In global coronal applications, the lower radial boundary is often set to be at the coronal base, thereby omitting the photosphere and the extreme gradients appearing in the transition region. Special attention must then be made to choose boundary conditions such that the essential characteristics of the lower atmosphere is preserved, such as the line-tying of the magnetic field.

A significant simplification applied in most of the modeling work done in this thesis is that of restricting to spatially two-dimensional domains by assuming the existence of a symmetry in the system. Furthermore, if the intent is to study dynamics occurring on a length scale a fraction of the solar radius, the curvature of the solar surface can be neglected and a Cartesian domain employed. This is the case for the local modeling performed in Article I, where a Cartesian domain with a translational invariance in one of the directions parallel to the (flat) solar surface

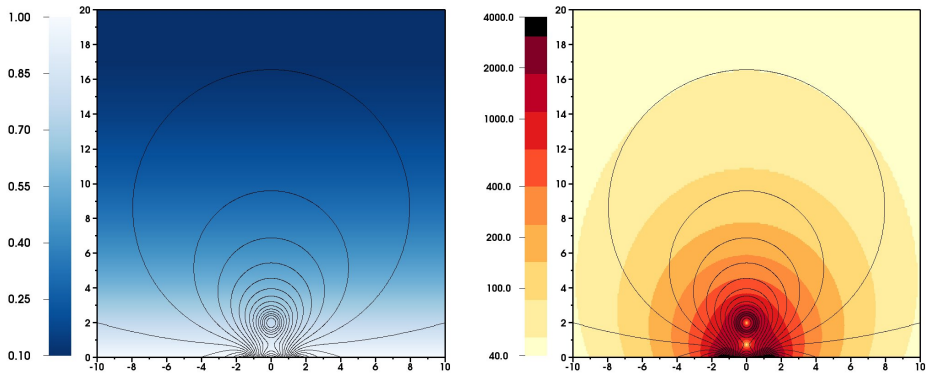

Figure 3.1: Initial condition for the local model. Left: Density distribution in units of $1.67 \cdot 10^{-13}$ kg/m^3. Right: Alfvén speed in units of km/s (logarithmic color bar). The black lines depict magnetic field lines. The unit of length $l = 10$ Mm.

is assumed. On the other hand, for the global modeling conducted in Article II and III, the domain consists of a spherical shell with a rotational symmetry in the azimuthal direction.

3.3 Local modeling

A model for investigating the early stages of the dynamics induced by the lift-off of a CME is constructed in Article I. Due to the local nature of the model, a Cartesian domain with translational symmetry is employed, as discussed in the previous section. For the same reason, the effects of the solar wind is neglected, and a static ambient corona under the influence of a constant gravitational acceleration is considered.

The magnetic field of the CME progenitor consists of a detached flux rope produced by an infinitely long and straight uniform current with a given radius. Outside the flux rope, the magnetic field is potential and given as a sum of the field due to the line current and it's image current as well as a background field composed of four line currents placed beneath the solar surface, similar to that of Magara et al. (2000), Chen and Shibata (2000).

The advantage of such a simple configuration is that the free parameters describing the current elements can be determined by an analytical analysis so that the force balance, equation Eq. (3.7), is approximately satisfied inside the flux rope. Ignoring gravity, this can be accomplished in two different ways: either by introducing a perpendicular (toroidal) component making the magnetic field force-free or by adjusting the density distribution so that the pressure gradient balances the Lorentz force. Figure 3.1 shows the distribution of density (left panel) and Alfvén speed (right panel) as well as the field lines of the magnetic field superimposed for

an initial state similar to the one described in Article I (compare with Figure 1 a and b), but with different parameters in order to represent a smaller active region-like environment. The Alfvén speed, v_A, decreases in a quasi-circular fashion away from the active region. For a larger domain, as considered in Article I, a minimum in v_A is obtained at a height $h \sim 0.2R_\odot$ above the coronal base, after which it starts to increase as a function of height. Such a spatial variation of the Alfvén speed is consistent with the semi-empirical model of Warmuth and Mann (2005).

The initially stable flux rope is made to erupt by adding an artificial force acting on the plasma elements of the flux rope determined by a closed path corresponding to a specific value of the component of the vector potential parallel to the axis of translational symmetry. With such a prescription, eruptions starting from identical initial states but with different height-time profiles can be studied. Naturally, such a static equilibrium initial state would also lend itself well to studies of initiation mechanisms. Indeed, a similar configuration has been employed for studying CME initiation in a flux emergence-scenario (Chen and Shibata, 2000). A detailed description of the model setup is provided in section A.1 in the Appendix.

3.4 Two-dimensional global modeling

In order to be able to study the evolution of the eruption-induced coronal dynamics for times beyond a few tens of minutes after the onset of the event, it becomes necessary to consider a model that takes into account features arising due to the globality of the problem, such as the curvature of the Sun and solar wind outflow.

3.4.1 Azimuthal symmetry

In articles II and III, a two-dimensional axisymmetric model in a meridional plane including both poles and stretching from the coronal base up to $r = 30R_\odot$ is constructed. Considering the large extent in the radial direction, the initial state of the model should include a solar wind solution. As shortly discussed in section 3.2.1 and at some length in Article III, additional terms providing heating so that the solar wind is accelerated to velocities typically observed need to be inserted into the model.

In Article II, the common method of choosing $\gamma = 1.05$ is adopted. Wind solutions obtained with such a simple parametrization of the unknown heat input are known to have certain inadequacies, such as not producing a fast polar wind (e.g., Fig. 1 in Article II). Therefore, in Article III, two alternative methods popular from the literature are pursued. In the first method, a spatially dependent polytropic index chosen so that the speeds of the MHD wind solution matches that

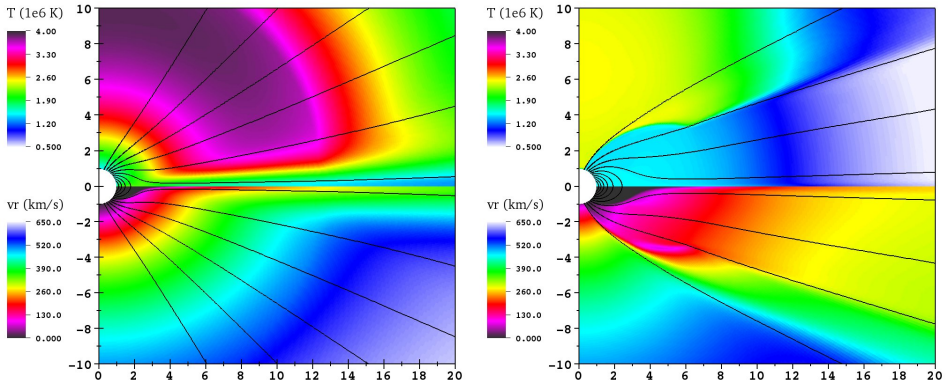

Figure 3.2: Steady-state solar wind solutions obtained with two different heating prescriptions. Left: Model employing a spatially varying polytropic index based on the WSA model. Right: Model employing a heating/cooling source term with a target temperature. Upper halves depict temperature in units of MK, lower halves radial speed in units of km/s. Note that the palettes are the same, and the magnetic field lines (black curves) originate from the same location at the lower boundary.

given by the empirical Wang-Sheeley-Arge (WSA) model (Arge and Pizzo, 2000) is adopted, while in the second method an additional energy source

$$Q = \rho q_0 (T_0 - T) \exp\left(-\frac{(r - R_\odot)^2}{\sigma^2}\right) \tag{3.8}$$

is employed. The effect of Eq. (3.8) is to add (or remove) heat so that the plasma is driven towards the target temperature $T_0(\mathbf{r})$. Additionally, the heating scale height σ is spatially nonuniform.

Figure 3.2 displays the self-consistently produced steady-state solutions obtained with the two heating prescriptions. In both cases, the simulations were run until a converged state was reached, employing the same boundary conditions as well as initial condition consisting of a spherically symmetric hydrodynamic Parker solution and a dipole magnetic field. Therefore, the difference of the obtained solutions is solely due to the difference in the prescribed heating.

Altering the equations governing the physics, either by reducing the polytropic index below the expected value of $\gamma = 5/3$ or by the introduction of new source terms, naturally changes the behavior of the system, and the consequences for the dynamics of the particular problem under study must be understood. For instance, for applications involving shocks, the way in which the Rankine-Hugioniot relations are modified needs to be addressed. If the polytropic index is changed, the maximum attainable compression is likewise altered according to

$$r_{\max} = \frac{\gamma + 1}{\gamma - 1}. \tag{3.9}$$

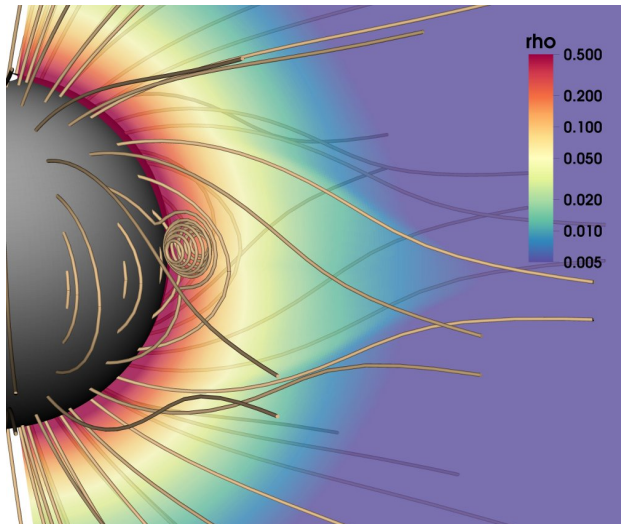

Figure 3.3: Magnetic field lines of the initial state corresponding to the polytropic axisymmetric wind solution (Fig. 3.2 (left)) extended in the azimuthal direction with a spherical CME progenitor superimposed. The colored backdrop indicates the density distribution. Note the logarithmic color bar.

Therefore, although using a spatially variable polytropic index or a temperature-dependent energy source term can represent the required heating in steady-state solar wind configurations, their applicability in cases of dynamical disturbed situations must be evaluated. Such a discourse is undertaken in Article III.

Since the focus in Article II and Article III is on studying the shock structure induced by an erupting CME and not in the initiation, a circular non-equilibrium structure with a higher density and a non-zero radial velocity is simply superimposed on the steady-state solar wind solution. A similar model has been employed by, e.g., Chané et al. (2005), Jacobs et al. (2005)

3.5 Towards three-dimensional global modeling

Two-dimensional azimuthally symmetric coronal models are efficient tools for studying coronal large-scale dynamics due to the highly beneficial trade-off between realism and the computational workload that they offer: all the physics governing the dynamics that would be included in a full three-dimensional calculation are inherently included in the two-dimensional case as well, but with the significant practical difference that the computing power of a standard desktop computer of today is sufficient to solve the two-dimensional system in a reasonable amount of time. Yet, in order to be able to engage in studies of specific events and compare the simulation results to actual observations rather than concentrating on fundamental physics, three-dimensional models are inevitable.

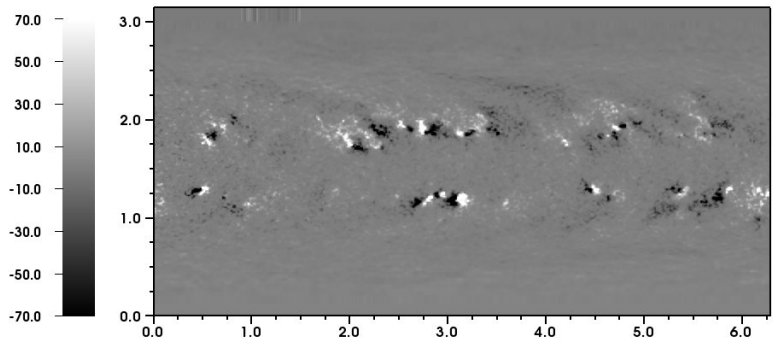

Figure 3.4: Modified GONG synoptic map of the radial component of the photospheric magnetic field corresponding to Carrington rotation 2011. The unit of the color bar is Gauss.

3.5.1 Axisymmetric wind solution in three dimensions

In a first approach towards three-dimensional modeling, the steady-state solar wind solution obtained from the axisymmetric solution can be extended in the azimuthal direction and used as the initial condition for a simulation employing a fully three-dimensional CME eruption model. Such a model could be used to study eruptive events in a solar minimum-like corona, as well as to assess the effects introduced by assuming axisymmetry.

Figure 3.3 plots selected magnetic field lines as well as the background density distribution of the axisymmetric solution presented in the left panel in Fig. 3.2 extended in the azimuthal direction. The flux rope structure is given by exactly the same mathematical prescription as the one used in Article III (Eq. (7) in the article), with the extension in the azimuthal direction performed by assuming the CME to be spherical. As a result, in the $\phi = 90^{\circ}$ plane, the two- and three-dimensional initial conditions are identical, and produces a magnetic field configuration that is confined inside a sphere. A similar CME model has recently been employed by Shen et al. (2011).

3.5.2 Event-oriented three-dimensional modeling

In order to take a step towards a less idealized model of the solar corona, the assumption of a dipolar magnetic field needs to be relaxed. One way of achieving this is by employing a reconstruction method in which the coronal magnetic field is extrapolated based on observed photospheric magnetograms, bringing the simulation a step closer towards an event-oriented model.

Adopting the most widely used reconstruction method, the initial magnetic field is obtained by employing the potential field source surface (PFSS) method. The map of the radial magnetic field needed as input for the PFSS model is obtained from

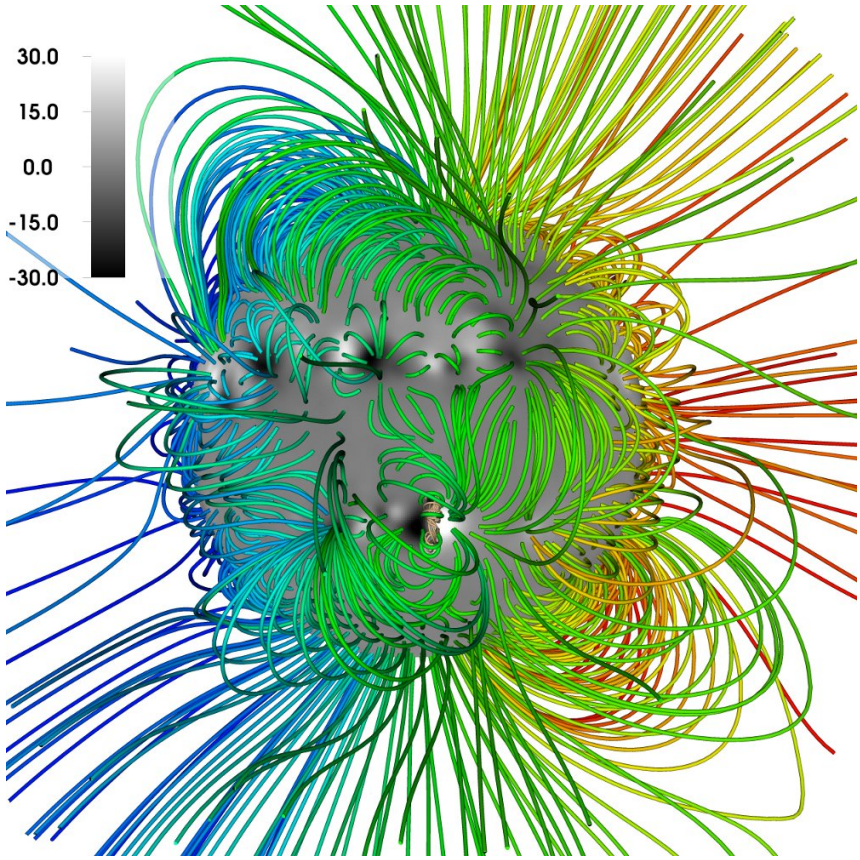

Figure 3.5: Radial component of the magnetic field at $r = 1.031 R_\odot$ (the lower boundary of the simulation) and selected magnetic field lines of the initial configuration. The unit of the color bar is Gauss.

a photospheric synoptic line-of-sight magnetogram provided by the Global Oscillation Network Group (GONG). For this study, the synoptic map corresponding to Carrington rotation 2111 is chosen. In order to make the magnetogram more suitable as input for the MHD calculation, the original data is modified according to the following steps:

1. The absolute maximum values of the radial magnetic field is restricted to $|B_r| \leq 70$ G.
2. The 360×180 longitude-$\sin$(latitude) grid is remapped to a 720×360 uniform longitude-latitude grid by using a bi-linear interpolation in order to smooth the map.
3. The discrete monopole contribution is subtracted

Figure 3.4 shows the resulting map of the radial component of the magnetic field.

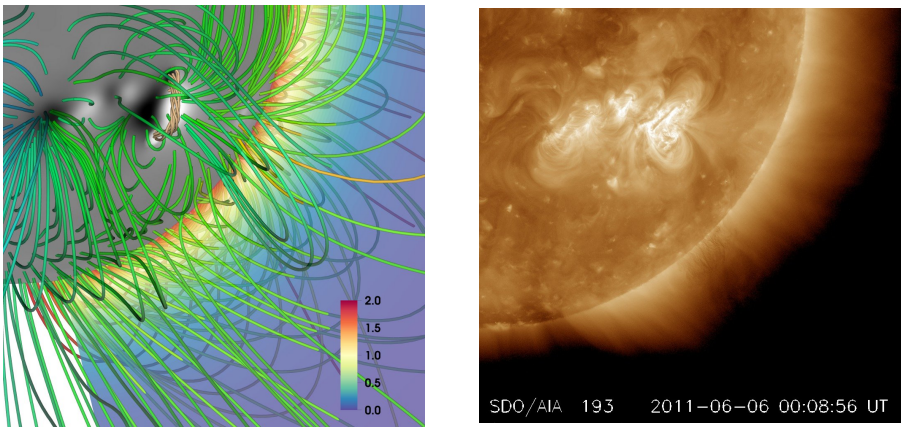

Figure 3.6: Left: Zoom-in on the flux rope structure. The backdrop shows the density distribution, in units of $1.67 \cdot 10^{-13}$ kg/m^3. Right: AIA 193 Å image roughly 30 hours before eruption (`http://sdo.gsfc.nasa.gov/data/aiahmi/`).

Using this map, the magnetic scalar potential that produces a magnetic field whose radial component at $r = R_\odot$ matches the input radial field and that becomes purely radial at the source surface located at $r = 2.5R_\odot$ is calculated using a finite-difference method detailed by Tóth et al. (2011). The advantage of the finite-difference method compared to a spherical harmonics expansion approach is that the input magnetogram is exactly recovered as the radial field at the lower boundary, and ringing due to the Gibbs phenomenon does not appear (e.g., Tran, 2009, for details).

With the initial magnetic field given as a potential field, the pressure is chosen so that it balances gravity. Specifically, the temperature is chosen to as

$$T(r, \theta, \phi) = T_\mathrm{c} \left(\frac{R_\odot}{r} \right)^{\frac{1}{2}} \tag{3.10}$$

which determines the density

$$\rho(r, \theta, \phi) = \rho_0 \left(\frac{r}{R_\odot} \right)^{\frac{1}{2}} \exp \left[\frac{2GMm}{k_\mathrm{B} T_\mathrm{c} R_\odot} \left(\left(\frac{R_\odot}{r} \right)^{\frac{1}{2}} - \left(\frac{R_\odot}{r_0} \right)^{\frac{1}{2}} \right) \right] \tag{3.11}$$

with $\rho_0 = 2.89 \cdot 10^{-13}$ kg/m^3 corresponding to an electron density $n_\mathrm{e} = 1.5 \cdot 10^8$ cm^{-3}, $r_0 = 1.035R_\odot$ and $T_\mathrm{c} = 1.5 \cdot 10^6$ K. Thus, with $\mathbf{v} = 0$, the initial condition is in static equilibrium, thereby excluding a solar wind outflow from the model. Nevertheless, the PFSS model mimics the effect of the solar wind on the magnetic field by producing a configuration that becomes radial at the source surface.

The final step is then to specify the means by which an eruption is generated. Keeping to the idea of making the model more event-specific, a modification of

the model of Titov and Démoulin (1999) is employed. In the original model, an analytic force-free equilibrium magnetic field configuration is constructed by embedding a semicircular flux rope produced by a toroidal current into a bipolar field. The model is modified by removing the point-charge sources and the infinite line current responsible for generating the bipolar field. Instead, the PFSS potential field of the source active region provides the overlying strapping field. A similar CME model has been employed in several studies (e.g., Loesch et al., 2011, and references therein).

The flux rope is oriented such that the neutral line of the model lines up with the neutral line of the magnetogram, and the size of the flux rope is chosen so that the configuration resembles somewhat the filament structure that erupted producing the June 7, 2011 event. Finally, the current of the flux rope is chosen so that the flux rope is in a sufficiently out-of-equilibrium state to drive the eruption. The parameters used in the simulation are given in section A.2. In contrast to the calculations including the solar wind presented in the previous sections, this model is better suited for studying the waves induced in the low corona for times within a few tens of minutes after the onset.

Figure 3.5 visualizes the topology of the magnetic field of the initial state. Further, the density and temperature distribution are shown in Fig. 3.6 zooming in on the flux rope structure. Also, a SDO/AIA 193 Å EUV imaging observation roughly 30 hours before the eruption onset is shown. It is important to note that the parameters of the model were not optimized for the event in any way. In fact, the simulation with the parameters described above was the sole run conducted for this study.

Chapter 4

Methods of Computational MHD

The increasing interest in using computer simulations as aids in understanding the highly non-linear dynamics of systems consisting of plasmas in space physics, astrophysics as well as in engineering has lead to a rapid growth of the field of computational magnetohydrodynamics. As a consequence, a myriad of methods to numerically solve the equations of MHD have been proposed and employed in a multitude of physical settings. Therefore, the first step in constructing a numerical MHD model of the system of interest is to select the computational algorithms best suited for the task given the nature of the flows occurring in the system.

In order to be able to address the type of questions posed in this thesis, the MHD solver needs to fulfill a number of specific criteria. First, the method must be able to capture shocks and discontinuities without producing numerical instabilities. Second, to conduct simulations in a global domain in a natural way, the use of spherical coordinates is advantageous. Third, the large gradients occurring near the solar surface generally necessitates the use of non-uniform grids and a method with high spatial accuracy. Also, the numerical scheme should be able to accommodate various boundary conditions in addition to fulfilling the general requirements of accuracy, robustness, efficiency and simplicity.

The finite volume (FV) method is a versatile discretization technique widely used in computational fluid dynamics (CFD). The popularity of the method stems from the inherent shock capturing properties of the method as well as from the fact that, apart from structured grids that employ a logically rectangular indexing, grids obtained from a more general tesselation procedure can readily be used without sacrificing simplicity. For these reasons, the FV method is the discretization approach of choice for the MHD solver developed in this thesis. As will be shown in the following sections, the developed FV algorithm is able to fulfill most of the criteria laid out above to a satisfactory degree.

The FV method is particularly suited for solving conservation laws. Indeed, as noted in chapter 3.1, the equations of ideal MHD constitute a set of conservation

laws. Thus, the extensive body of research devoted to solving hyperbolic conservation laws can be applied to the MHD equations. Due to the specific mathematical structure of the MHD system, however, care must be taken in doing so. In fact, for multidimensional systems, the MHD equations cannot be viewed as a simple extension of the Euler equations of gas dynamics with just a larger number of variables. This is a consequence of the structure of the induction equation and the divergence-free property of the magnetic field. Therefore, the MHD system is more properly represented by two coupled subsystems

$$\partial_t \mathbf{u}(\mathbf{r}, t) + \nabla \cdot \mathcal{F}(\mathbf{u}, \mathbf{B}) = 0, \tag{4.1}$$

$$\partial_t \mathbf{B}(\mathbf{r}, t) + \nabla \times \mathbf{E}(\mathbf{u}, \mathbf{B}) = 0, \tag{4.2}$$

together with the non-evolutionary constraint

$$\nabla \cdot \mathbf{B} = 0 \tag{4.3}$$

on the magnetic field (e.g., Londrillo and Del Zanna, 2000, 2004). This separation reflects the different nature of the variables: the array $\mathbf{u}$ contains scalar variables whereas the components of the magnetic field form a pseudo-vector. At discontinuities this difference becomes explicit. The first subsystem, Eq. (4.1), results in Rankine-Hugoniot jump conditions analogous to that of the Euler system. On the other hand, the component of the magnetic field normal to the surface of discontinuity is continuous, and jump conditions exist only for the tangential components. Thus, the general methods developed for hyperbolic conservation laws are directly applicable to Eq. (4.1) only, while another algorithm must be applied to the induction equation so that the different smoothness properties of the magnetic field manifested by the divergence free condition, Eq. (4.3), are consistently taken into account.

In the next subsection, the methods used to solve the first subsystem are presented, while the MHD-specific issues are discussed in section 4.2. The goal of this chapter is not only to present the specific methods employed in this work, but also to discuss some of the available alternative methods as well as highlight a selection of promising recent advances.

4.1 Constructing the FV scheme

The majority of the numerical methods developed for solving partial differential equations (PDEs) rely on mesh-based techniques, i.e., the (spatio-temporal) domain of interest Ω is *discretized* into a set of elements or cells Ω_c such that $\cup\, \Omega_c \simeq \Omega$. A key step in constructing the algorithm is then to choose the manner in which the PDEs are satisfied on the discrete level.

Due to the feature of non-linear conservation laws that discontinuities may develop in finite time even when the initial data is smooth, the emphasis is on seeking *weak solutions* to the conservation laws which is equivalent to requiring that $\mathbf{u}$

obey the integral form of Eq. (4.1). Averaging Eq. (4.1) over a volume V bounded by a surface S yields the integral form

$$\frac{d}{dt}\langle \mathbf{u} \rangle(t) + \frac{1}{V} \oint_S \mathcal{F} \cdot d\mathbf{S} = 0 \tag{4.4}$$

where $\langle \cdot \rangle$ denotes a volume-average,

$$\langle \mathbf{u} \rangle(t) = \frac{1}{V} \int_V \mathbf{u}(\mathbf{r}, t)\, dV. \tag{4.5}$$

The essential idea of the finite volume method is to utilize the integral form, Eq. (4.4), as the basis for the discretization. Thus, for each spatial cell Ω_c, the volume-average $\langle u \rangle$ of each component of $\mathbf{u}$ averaged over that cell is stored. The temporal evolution of $\langle u \rangle$ in each cell is given by Eq. (4.4) via the total flux of u through the surface of the cell. In this manner, the conservative property of the continuum equation is carried over to the discrete level of the numerical algorithm.

To concretize the discussion above and illustrate the actual steps required in constructing a finite volume numerical scheme, consider the Cartesian two-dimensional conservation law

$$\partial_t \mathbf{u} + \partial_x \mathbf{F} + \partial_y \mathbf{G} = 0 \tag{4.6}$$

on the spatial domain Ω discretized by a set of rectangular cells each of size $\Delta x \times \Delta y$. For the cell Ω_{ij} of extent $[x_{i-\frac{1}{2}}, x_{i+\frac{1}{2}}] \times [y_{j-\frac{1}{2}}, y_{j+\frac{1}{2}}]$ where $x_{i\pm\frac{1}{2}} \equiv x_i \pm \Delta x/2$, $y_{j\pm\frac{1}{2}} \equiv y_j \pm \Delta y/2$ and (x_i, y_j) denotes the coordinates of the cell center, the integral form of the conservation law gives

$$\partial_t \widehat{\mathbf{u}}_{ij} = -\frac{\overline{\mathbf{F}}_{i+\frac{1}{2},j} - \overline{\mathbf{F}}_{i-\frac{1}{2},j}}{\Delta x} - \frac{\overline{\mathbf{G}}_{i,j+\frac{1}{2}} - \overline{\mathbf{G}}_{i,j-\frac{1}{2}}}{\Delta y} \tag{4.7}$$

where $\widehat{\cdot}$ denotes an area-average and $\overline{\cdot}$ denotes a line-average, i.e., $\widehat{\mathbf{u}}_{ij}$ is the cell-average of $\mathbf{u}$ in Ω_{ij} and

$$\overline{\mathbf{F}}_{i\pm\frac{1}{2},j} = \frac{1}{\Delta y} \int_{y_{j-\frac{1}{2}}}^{y_{j+\frac{1}{2}}} \mathbf{F}(\mathbf{u}(x_{i\pm\frac{1}{2}}, y, t))\, dy \tag{4.8}$$

$$\overline{\mathbf{G}}_{i,j\pm\frac{1}{2}} = \frac{1}{\Delta x} \int_{x_{i-\frac{1}{2}}}^{x_{i+\frac{1}{2}}} \mathbf{G}(\mathbf{u}(x, y_{j\pm\frac{1}{2}}, t))\, dx \tag{4.9}$$

are line-averaged fluxes. Equation (4.7) shows that the FV-discretized conservation law retains the form of the continuum equation at the discrete level. It is important to note that Eq. (4.7) together with Eq. (4.8) and Eq. (4.9) is exact: the only operation so far has been to divide space into a regular mesh. The same idea can be applied to the temporal dimension as well. Integrating Eq. (4.7) in time from t_n to $t_n + \Delta t = t_{n+1}$ yields

$$\widehat{\mathbf{u}}_{ij}(t_{n+1}) = \widehat{\mathbf{u}}_{ij}(t_n) - \frac{\Delta t}{\Delta x}\left[\widehat{\mathbf{F}}_{i+\frac{1}{2},j} - \widehat{\mathbf{F}}_{i-\frac{1}{2},j}\right] - \frac{\Delta t}{\Delta y}\left[\widehat{\mathbf{G}}_{i,j+\frac{1}{2}} - \widehat{\mathbf{G}}_{i,j-\frac{1}{2}}\right] \tag{4.10}$$

where

$$\widehat{\mathbf{F}}_{i\pm\frac{1}{2},j} = \frac{1}{\Delta t \Delta y} \int_{t_n}^{t_{n+1}} \int_{y_{j-\frac{1}{2}}}^{y_{j+\frac{1}{2}}} \mathbf{F}(\mathbf{u}(x_{i\pm\frac{1}{2}}, y, t))\, dy\, dt \tag{4.11}$$

and similarly for $\widehat{\mathbf{G}}_{i,j\pm\frac{1}{2}}$. Again, the relation given by Eq. (4.10) is exact.

Following the path laid out above would eventually lead to a *fully discrete* numerical scheme. In contrast, a *semi-discrete* scheme will instead be pursued by using the method of lines approach. Since the right-hand side of Eq. (4.7) is a purely spatial operation, the equation can be viewed as a system of ordinary differential equations (ODEs)

$$\partial_t \widehat{\mathbf{u}}_{ij}(t) = L(\mathbf{u}(t))|_{ij} \tag{4.12}$$

with L denoting the spatial operator. Thus, the spatial and temporal calculations are separated, which simplifies the analysis considerably.

Although the discussion so far has been exact, approximations become inevitable in order for the analysis to proceed. The aim is to arrive at a numerical scheme that is accurate to order r in the one-step error. In other words, denoting by $\mathfrak{H}$ the algorithm that marches the set of cell averages a time Δt forward in time, it should satisfy

$$\mathfrak{H}(\widehat{\mathbf{w}}(t)) - \widehat{\mathbf{w}}(t + \Delta t) = \mathcal{O}(h^{r+1}) \tag{4.13}$$

where $\widehat{\mathbf{w}}$ are the (area) cell-averages of the exact solution, and h is the size of the spatial grid, $h = \max(\Delta x, \Delta y)$. Employing the semi-discrete framework, Eq. (4.13) is satisfied provided that an rth order accurate method in time to solve the system of ODEs of Eq. (4.12) is available and the exact spatial operation L is known. While the former requirement can be fulfilled by, e.g., Runge-Kutta (RK) methods as discussed in section 4.1.4, it is in general not possible to fulfill the latter requirement. Nevertheless, Eq. (4.13) is still satisfied if L is replaced by $\mathcal{L}$ operating on the cell-averages that approximates the exact spatial operator,

$$\mathcal{L}(\widehat{\mathbf{u}}) = L(\mathbf{u}) + \mathcal{O}(h^r). \tag{4.14}$$

In the two-dimensional Cartesian case of Eq. (4.7) the right-hand side provides the exact operator L. Analogously, the operator $\mathcal{L}$ is defined as

$$\mathcal{L}(\widehat{\mathbf{u}})|_{ij} = -\frac{\overline{\boldsymbol{\mathcal{F}}}_{i+\frac{1}{2},j} - \overline{\boldsymbol{\mathcal{F}}}_{i-\frac{1}{2},j}}{\Delta x} - \frac{\overline{\boldsymbol{\mathcal{G}}}_{i,j+\frac{1}{2}} - \overline{\boldsymbol{\mathcal{G}}}_{i,j-\frac{1}{2}}}{\Delta y} \tag{4.15}$$

where $\overline{\boldsymbol{\mathcal{F}}}$ and $\overline{\boldsymbol{\mathcal{G}}}$ are (numerical) approximations to the exact fluxes Eq. (4.8) and Eq. (4.9), respectively. Due to their central role in specifying the numerical algorithm, the approximations are often dubbed as *numerical flux functions*.

In order to arrive at an algorithm for computing the spatial operator $\mathcal{L}$, the need for approximations becomes evident from the fact that point values of $\mathbf{u}$ are needed at the cell edges in order to compute the fluxes in Eq. (4.8) and Eq. (4.9), while

it is only the cell-averaged quantities $\widehat{\mathbf{u}}$ that are available. Thus, a procedure of computing (local) point values from the available cell-averaged quantities is needed. In other words, a function $\mathbf{p}(x, y, t)$ that *reconstructs* the cell-averages $\widehat{\mathbf{u}}$ and approximates the point-wise solution $\mathbf{u}$ to a desired accuracy,

$$\mathbf{p}(x, y, t; \{\widehat{\mathbf{u}}(t)\}) - \mathbf{u}(x, y, t) = \varepsilon_1(x, y)h^{r_1}, \tag{4.16}$$

is needed. Assuming that such a function can be constructed, the next step is to compute the integrals in Eq. (4.8) and Eq. (4.9). This can be accomplished, for instance, by employing an appropriate quadrature rule,

$$\overline{\mathbf{F}}_{i\pm\frac{1}{2},j} = \sum_{k=1}^{K} a_k \mathbf{F}(\mathbf{u}(x_{i\pm\frac{1}{2}}, y_k, t)) + \varepsilon_2(x_{i\pm\frac{1}{2}}, y_\eta)h^{r_2} \tag{4.17}$$

where a_k are the weights of the quadrature, and $y_\eta \in [y_{j-\frac{1}{2}}, y_{j+\frac{1}{2}}]$. Casper and Atkins (1993) provides a detailed discussion of the error arising from this step. Upon using the reconstruction function,

$$\mathbf{F}(\mathbf{u}) = \mathbf{F}(\mathbf{p}) + \varepsilon_3(x, y)h^{r_1} \tag{4.18}$$

where $\varepsilon_3 = \mathcal{O}(\varepsilon_1)$, and the approximated flux becomes

$$\overline{\mathbf{F}}_{i\pm\frac{1}{2},j} = \sum_{k=1}^{K} a_k \left[\mathbf{F}(\mathbf{p}(x_{i\pm\frac{1}{2}}, y_k, t)) + \varepsilon_3(x_{i\pm\frac{1}{2}}, y_k)h^{r_1}\right] + \varepsilon_2(x_{i\pm\frac{1}{2}}, y_\eta)h^{r_2}. \tag{4.19}$$

Computing the first term of the right hand side of Eq. (4.7) gives

$$\begin{aligned}\frac{\overline{\mathbf{F}}_{i+\frac{1}{2},j} - \overline{\mathbf{F}}_{i-\frac{1}{2},j}}{\Delta x} &= \frac{1}{\Delta x}\sum_{k=1}^{K} a_k \left[\mathbf{F}(\mathbf{p}(x_{i+\frac{1}{2}}, y_k, t)) - \mathbf{F}(\mathbf{p}(x_{i-\frac{1}{2}}, y_k, t))\right] \\ &\quad + \sum_{k=1}^{K} a_k \left[\varepsilon_3'(x_\eta, y_k)\right] h^{r_1} + \varepsilon_2'(x_\eta, y_\eta)h^{r_2}.\end{aligned} \tag{4.20}$$

Thus, if the numerical flux $\overline{\boldsymbol{\mathcal{F}}}_{i\pm\frac{1}{2},j}$ in Eq. (4.15) is chosen as

$$\overline{\boldsymbol{\mathcal{F}}}_{i\pm\frac{1}{2},j} = \sum_{k=1}^{K} a_k \mathbf{F}(\mathbf{p}(x_{i\pm\frac{1}{2}}, y_k, t)) \tag{4.21}$$

and similarly for $\overline{\boldsymbol{\mathcal{G}}}_{i,j\pm\frac{1}{2}}$, and the reconstruction and quadrature procedures are performed so that $r_1 = r_2 = r$, then $\mathcal{L}$ satisfies Eq. (4.14) and the construction of an rth order accurate scheme has been accomplished.

It is important to note that in the analysis presented above the solution was assumed to be smooth. Therefore, the algorithm needs to be modified so that in

smooth regions the considerations above still hold and, additionally, possible discontinuities in the solution should be accounted for. In fact, jumps at cell interfaces occur naturally as a result of the local nature of the reconstruction procedure. That is, the reconstruction function $\mathbf{p}$ is constructed on a cell-to-cell basis, with a different function $\mathbf{p}_{ij}$ constructed in each cell $\Omega_{i,j}$. Therefore, the reconstruction function differs from the one in the neighboring cells, resulting in jumps for the interface values given by the different functions. Near discontinuities, the jump is of size $\mathcal{O}(1)$ while in smooth regions it is of size $\mathcal{O}(h^r)$.

A discontinous initial condition evolves in time by decaying to a set of wave structures. As will be elucidated in section 4.1.3, the flux function $\mathbf{F}(\mathbf{u})$ in Eq. (4.21) must therefore be replaced by a function $\mathfrak{F}(\mathbf{u}_L, \mathbf{u}_R)$ that accounts for the fact that information propagates in the characteristic directions. The standard method for achieving this is by solving the Riemann problem defined by the two states $\mathbf{u}_L$ and $\mathbf{u}_R$.

With such a modification, the final expression for the numerical flux function is

$$\overline{\boldsymbol{\mathcal{F}}}_{i\pm\frac{1}{2},j} = \sum_{k=1}^{K} a_k \mathfrak{F}\left(\mathbf{p}_{i-\frac{1}{2}\pm\frac{1}{2},j}(x_{i\pm\frac{1}{2}}, y_k, t), \mathbf{p}_{i+\frac{1}{2}\pm\frac{1}{2},j}(x_{i\pm\frac{1}{2}}, y_k, t)\right). \quad (4.22)$$

The recipe for computing the spatial operator $\mathcal{L}$ is then complete once the reconstruction method, Riemann solver and quadrature rule have been specified.

4.1.1 Alternative discretization methods

The advantage of the finite volume method is the ability of the method to yield conservative discretizations on complex meshes. Although the discussion in the previous section used rectangular cells, meshes consisting of triangular (tetrahedral in 3-D) cells could equally well be used. When considering higher-order schemes in multiple dimensions the reconstruction procedure and computation of the flux integral become increasingly more complex. For this reason, the primary choice for most practitioners using the FV method has been to employ approximations accurate to second order in which point values and volume averaged values are largely interchangeable and spatial integrals can be replaced by point values using the midpoint rule. Another disadvantage is the relative difficulty to apply the method to PDEs of mixed type which often arise in applications.

An alternative to the finite volume method exhibiting largely reversed advantages and disadvantages is provided by Finite Difference Methods (FDMs). Although being often the primary discretization alternative for many PDEs and ODEs, the FDM has not been popular for discretizing conservation laws. This can be attributed to the fact that pointwise values are ambiguously defined at discontinuities, and FDMs approximate the PDEs in a pointwise manner. The FDM can,

however, be applied in a specific manner to the case of conservation laws to obtain a scheme to which the afore-mentioned anti-pointwise bias should not be applied.

Consider, for ease of exposition, the one-dimensional conservation law

$$\frac{\partial \mathbf{u}}{\partial t} + \frac{\partial \mathbf{F}}{\partial x} = 0 \tag{4.23}$$

conservatively discretized in a pointwise fashion as

$$\frac{\partial \mathbf{u}(x_i, t)}{\partial t} + \frac{\mathbf{H}(x_{i+\frac{1}{2}}, t) - \mathbf{H}(x_{i-\frac{1}{2}}, t)}{\Delta x} = 0. \tag{4.24}$$

The function $\mathbf{H}$ is related to the flux $\mathbf{F}$ by

$$\mathbf{F}(\mathbf{u}(x_i, t)) = \frac{1}{\Delta x} \int_{x_{i-\frac{1}{2}}}^{x_{i+\frac{1}{2}}} \mathbf{H}(\xi, t)\, d\xi \equiv \overline{\mathbf{H}}(x_i, t). \tag{4.25}$$

Applied in this way, this specific FDM yields a conservative discretization that is a mathematically transformed version of the discretization given by the FVM. Thus, at the discrete level, the values $\mathbf{u}(x_i, t)$ are not the true pointwise values, but instead approximations obtained by applying the inverse volume averaging operator to $\langle \mathbf{u} \rangle$ (Merriman, 2003).

Completely analogous to FV schemes, the conservative FD scheme needs a reconstruction procedure in order to obtain pointwise values of $\mathbf{H}$ from the known averages $\overline{\mathbf{H}}$. Also, similar to the FV case, a procedure that accounts for the fact that information propagates in the characteristic directions must be constructed in order to obtain a stable numerical scheme.

When applying the conservative FD scheme to multiple dimensions or higher orders, the differences to the FV schemes become apparent. In fact, the multidimensional procedure is simply a sum of the contributions of each dimension which are all treated analogous to the one-dimensional case above. As a consequence, the reconstruction procedure remains one-dimensional, being identical for all dimensions separately. Therefore, the computational complexity in the multidimensional case is exactly the same as in the one-dimensional case per point per direction. The big disadvantage of the conservative FDM is, however, that it can only be applied to uniform or certain smooth meshes without relaxing the requirement of strict conservation.

Finding a discretization method that would combine the advantageous characteristics of FV and FD in one would be highly desirable. Steps in such a direction have been taken by the construction of quadrature-free FV schemes (Dumbser et al., 2007) as well as advances in applying the discontinuous Galerkin method (e.g., Dumbser and Munz, 2006, Balsara et al., 2007).

4.1.2 Reconstruction algorithms

A crucial step for calculating accurate approximations of the flux through the cell surfaces is to obtain an accurate pointwise representation of the solution $\mathbf{u}(\mathbf{r}, t)$ given the set of cell averages $\{\langle \mathbf{u} \rangle(t)\}$. A considerable amount of work has been devoted to this task, as it has proved a challenge to fulfill the requirement that the reconstruction procedure should yield a highly accurate approximation in smooth regions while at the same time providing sharp non-oscillatory transitions at discontinuities.

The reconstruction problem is closely related to the classical interpolation problem. Consider the (one-dimensional) function $u(x)$ for which the cell average values $\{\langle u \rangle_i\}$ are known, and define the primitive function of $u(x)$ as

$$U(x) = \int_{x_{-\frac{1}{2}}}^{x} u(\xi)\, d\xi \tag{4.26}$$

where $x_{-\frac{1}{2}}$ is any arbitrary fixed point. Knowing all the cell averages, the point values of U are known at all cell edges since

$$U(x_{i+\frac{1}{2}}) = \sum_{l=0}^{i} \int_{x_{l-\frac{1}{2}}}^{x_{l+\frac{1}{2}}} u(\xi)\, d\xi = \sum_{l=0}^{i} \Delta x \langle u \rangle_l. \tag{4.27}$$

Therefore, a function $P(x)$ interpolating U can be constructed that can be used to obtain an approximation to $u(x)$ by computing the derivative: $u(x) \approx p(x) \equiv P'(x)$. This procedure yields a consistent approximation of u in the sense that the cell average of $p(x)$ returns the data $\langle u \rangle$.

Typically, $p(x)$ (or P) is chosen to be a polynomial function. In Godunov's method, a constant reconstruction is adopted so that $p_i(x) = \langle u \rangle_i$ which yields a spatially first-order method. Superficially, achieving higher-order approximations is then a simple matter of increasing the degree of the polynomial. The task is made more complicated due to Godunov's theorem which states that numerical schemes that depend linearly on the input data and that are monotone can be at most first-order accurate. Thus, non-linearity must be introduced for achieving stable high-order schemes.

A widely popular approach of introducing non-linearity, especially for second-order schemes, is by invoking *limiters* in the reconstruction procedure. Consider the linear reconstruction function

$$p_i(x) = \langle u \rangle_i + s_i(x - x_i), \quad x \in [x_{i-\frac{1}{2}}, x_{i+\frac{1}{2}}] \tag{4.28}$$

where s_i approximates the derivative of u in the cell i. If s_i is calculated using finite differences with a fixed stencil, such as central or one-sided differences, the reconstruction will yield oscillatory results at discontinuities. This can be avoided by suitably limiting the slope based on the local smoothness of the solution.

In fact, the large body of mathematical work that has been devoted to the study of the properties of numerical schemes for one-dimensional scalar conservation laws provides prescriptions of how the limiting should be performed. Of particular use are so called Total Variation Diminishing (TVD) methods that provide a means of constructing robust limiters.

The total variation of a function $u = u(x)$ is defined as

$$TV(u) = \int_{-\infty}^{\infty} |u'(x)|\, dx \tag{4.29}$$

and for discrete functions $\{u_i\}$ it is defined as $TV(u) = \sum_i |u_{i+1} - u_i|$. A fundamental property of the exact solution of the scalar version of Eq. (4.23) is that the total variation does not increase with time,

$$TV(u(t_2)) \leq TV(u(t_1)) \tag{4.30}$$

and is said to be TVD. For the case of a scalar linear flux function, this property can be shown to be shared by the numerical scheme if the slopes are calculated as

$$s_i = \left(\frac{u_{i+1} - u_i}{\Delta x} \right) \varphi(r_i) \tag{4.31}$$

where $r_i = (u_i - u_{i-1})/(u_{i+1} - u_i)$ is the ratio of left- and right-sided differences and φ is a *limiter function* that satisfies the criteria

$$0 \leq \varphi(r) \leq 2, \quad 0 \leq \varphi(r) \leq 2r, \quad \varphi(1) = 1 \tag{4.32}$$

derived by Sweby (1984) using the TVD theorem of Harten (1983). Armed with these criteria it is straight-forward to construct suitable limiters and several have been proposed in the literature, the limiter of van Leer (van Leer, 1974)

$$\varphi(r) = \frac{r + |r|}{1 + |r|} \tag{4.33}$$

being one example.

Although the TVD property holds only in the restricted case of scalar conservation laws in one dimension, the prescription of Eq. (4.31) together with a limiter turns out to give excellent non-oscillatory results even for more general equations. Due to their favorable combination of simplicity, efficiency and robustness, schemes that use TVD limiters have become extremely popular.

The TVD limiters achieve the non-oscillatory behavior by ensuring that any reconstructed value at any time does not lie outside the range of the input data by switching on a cell-to-cell basis between constant and linear reconstruction. The drawback of this is that at smooth extrema the method degenerates to first-order accuracy regardless of the accuracy to which the slopes s_i are computed. This is known as the clipping phenomenon of TVD limiters. To overcome this deficiency,

higher-order reconstruction methods must be employed. Indeed, a large number of such methods have been pursued. In recent years, the weighted essentially non-oscillatory (WENO) (see e.g., Shu, 2009, for a review) approach of using adaptive stencils as well as filtering techniques such as the monotonicity preserving method (Suresh and Huynh, 1997) have received much attention.

4.1.2.1 Reconstruction for systems in multiple dimensions

The discussion of the reconstruction so far was limited to the scalar one-dimensional case. For systems of equations in multiple dimensions, the reconstruction algorithm must accordingly be generalized.

Constructing a high-order, non-oscillatory genuinely multi-dimensional reconstruction algorithm is a highly non-trivial task. For this reason, a pragmatic approach of using one-dimensional reconstructions on a dimension-by-dimension basis is often applied. For FV schemes, such a procedure yields formally at most a second-order method. To reach higher orders, cross terms in the reconstruction polynomial must be included. Without elaborating on the subject, a notable idea has been presented by Balsara et al. (2009), wherein the WENO method is applied using five candidate stencils in order to arrive at fourth-order accurate approximations of terms such as $\partial_{xy}u$, and eight stencils for the $\partial_{xyz}u$ term.

When considering systems of equations, it is not strictly necessary to apply the reconstruction procedure to the set of conserved quantities $\mathbf{u}$ directly. Depending on the specific problem, another set of variables $\mathbf{u}'$ derived from $\mathbf{u}$ might behave more smoothly than $\mathbf{u}$, with increased accuracy as a result if the reconstruction is applied to $\mathbf{u}'$ instead. Generally, accurate results are obtained if a costly local characteristic decomposition is performed and the reconstruction is applied to the characteristic variables. Indeed, for higher-order ($r \gtrsim 3$) methods, the characteristic reconstruction is often inevitable in order to achieve non-oscillatory results (e.g., Qiu and Shu, 2002).

4.1.3 Upwinding the numerical flux

A natural consequence of the finite volume discretization method is the appearance of discontinuous data across cell interfaces. Consider the interface $x_{i+\frac{1}{2}}$ between cells i and $i+1$. Since the reconstruction function $p_i(x)$ is different for each cell, two values $u^L_{i+\frac{1}{2}} = p_i(x_{i+\frac{1}{2}})$ and $u^R_{i+\frac{1}{2}} = p_{i+1}(x_{i+\frac{1}{2}})$ will be produced for the interface that, in general, are non-equal regardless of which reconstruction method is used. In a finite time, the jump in the data evolves into a set of structures propagating away from the cell interface. The flux due to the waves should then be accounted for by the numerical flux computation. Algorithmically, this is done by replacing the flux function by an *upwinded* flux function $\mathfrak{F}$ which is often

taken to be a function of the two distinct interface values,

$$\mathbf{F}(u_{i+\frac{1}{2}}) \rightarrow \mathfrak{F}(u^L_{i+\frac{1}{2}}, u^R_{i+\frac{1}{2}}). \tag{4.34}$$

A widely popular approach to obtain the upwinded flux, originally proposed by Godunov, is by viewing the discontinuous data as comprising a Riemann problem, i.e., a Cauchy problem with two constant states separated by a discontinuity. Then, a Riemann solver of choice provides the needed numerical flux. In general, however, exact Riemann solvers are not available or are too complicated to be of practical use. Thus, approximate Riemann solvers that only partially open the Riemann fan, i.e., consider only a few wave modes, are most often employed.

The popular HLL approximate Riemann solver, proposed by Harten et al. (1983), assumes the structure of the Riemann problem to consist of three constant states separated by two waves. Thus, any other than the two waves propagating with the fastest speed to the left a^- and right a^+ are disregarded. Furthermore, the fastest speeds are assumed to be known a priori. With these assumptions, the resulting numerical flux is obtained as

$$\mathfrak{F}^{HLL} = \begin{cases} \mathbf{F}(\mathbf{u}^L), & a^- \geq 0 \\ \mathbf{F}^*, & a^- < 0 < a^+ \\ \mathbf{F}(\mathbf{u}^R), & a^+ \leq 0 \end{cases} \tag{4.35}$$

where

$$\mathbf{F}^* \equiv \frac{a^+\mathbf{F}(\mathbf{u}^L) - a^-\mathbf{F}(\mathbf{u}^R) + a^+a^-(\mathbf{u}^R - \mathbf{u}^L)}{a^+ - a^-}. \tag{4.36}$$

To determine the fastest wave speeds exactly, the exact solution to the Riemann problem is also needed (see, e.g., the discussion in Miyoshi and Kusano, 2005). In practice, a simplified estimate such as

$$a^- = \min(\lambda_{\min}(\mathbf{u}^L), \lambda_{\min}(\mathbf{u}^R)), \quad a^+ = \max(\lambda_{\max}(\mathbf{u}^L), \lambda_{\max}(\mathbf{u}^R)), \tag{4.37}$$

where $\lambda_{\min}$ and $\lambda_{\max}$ are the smallest and largest eigenvalues of the flux Jacobian of the conservation law, is often employed. If the two speeds are chosen to be equal, $a^+ = -a^- \equiv a$, then the HLL flux reduces to the very popular Rusanov flux (also known as the local Lax-Friedrichs flux).

Due to the inclusion of only two wave modes, the HLL solver suffers from excessive diffusion for systems of equations that admit the existence modes more than two. Thus, attempts at introducing more wave modes into the HLL framework have been carried out. For the case of ideal magnetohydrodynamics, several such schemes have been proposed, including HLLC solvers that use two intermediate states (Gurski, 2004, Li, 2005) as well as multi-stage solvers (Miyoshi and Kusano, 2005).

A different approach to solving the Riemann problem is offered by the famous Roe solver. The basic idea is to write the conservation law $\partial_t \mathbf{u} + \partial_x \mathbf{F} = 0$ in the

quasi-linear form $\partial_t \mathbf{u} + \mathbf{A}\partial_x \mathbf{u} = 0$. The Jacobian matrix $\mathbf{A}$ is then replaced by a constant matrix $\widetilde{\mathbf{A}}$, which causes the original PDE to become a linear system with constant coefficients. The linearized system is then used to define an approximate Riemann problem which is solved exactly. Although the Roe scheme can be highly accurate, it yields non-physical so called rarefaction shocks at sonic or transsonic rarefaction waves. To overcome this, specific entropy fixes must be introduced (e.g., LeVeque, 2002).

Although the idea of the Godunov method to view the discontinuous data at the interface as a Riemann problem has proved to be very fruitful, one can ask whether the assumption of constant states could be relaxed. Indeed, the idea of considering *Generalized* or *Derivative* Riemann problems in which the initial data consists of two piecewise smooth functions, typically polynomials, separated by a discontinuity has recently gained attention. In fact, investigations in this topic have led to the construction of a new class of fully discrete schemes, so called ADER schemes (for a short overview, see Dumbser et al., 2008). Although relatively new, the methods have shown to be very promising in many respects. Mentioning only one such example, Balsara et al. (2010) have demonstrated the method to be twice as fast as a semi-discrete Runge-Kutta-based scheme of equal accuracy.

4.1.4 Time integration

With the methods pertaining to the calculation of the spatial semi-discretization of the finite volume scheme described in the previous sections, the problem of integrating the system of ODEs of Eq. (4.12) can be addressed. The applied methods are generally catalogued as being explicit, implicit or semi-implicit depending on the manner in which the solution at different time-steps are inter-connected. In this thesis, only explicit methods are employed. Of the variety of schemes that could be considered, the Strong Stability Preserving (SSP) Runge-Kutta schemes are chosen due to the existence of a rich theoretical understanding of their properties as well as their widespread use.

When stability properties, such as the behavior of the total variation of the numerical schemes, are analyzed they are most often done so assuming a simple first-order forward Euler time integration. When using an arbitrary higher order temporal discretization, however, the derived properties are not necessarily carried over. SSP time discretizations are methods that preserve stability properties, such as TVD, whenever the same property is satisfied using forward Euler integration. Therefore, the SSP approach allows the analysis of stability properties for the spatial and temporal discretizations to be treated independently of each other, similar to the way the analysis of accuracy is separated by using the method of lines (section 4.1).

The schemes used in this work are the optimal SSP-RK(m, p) schemes cataloged by Gottlieb et al. (2009). Here, m denotes the number of stages of the method

and p the order of the method. The schemes are optimal in the sense of the size of the time-steps and cost of the method. As discussed in section 4.1, both the temporal and spatial solution operators must be p:th order accurate in order for the entire numerical scheme to be of order p. The optimal two-stage second-order SSP-RK$(2,2)$ method given by

$$\begin{aligned}\langle \mathbf{u} \rangle^{*} &= \langle \mathbf{u} \rangle^{(n)} + \Delta t L(\langle \mathbf{u} \rangle^{(n)}) \\ \langle \mathbf{u} \rangle^{(n+1)} &= \frac{1}{2}\langle \mathbf{u} \rangle^{(n)} + \frac{1}{2}\langle \mathbf{u} \rangle^{*} + \frac{1}{2}\Delta t L(\langle \mathbf{u} \rangle^{*})\end{aligned} \tag{4.38}$$

provides the time-integration for a second order scheme, while the optimal three-step third-order SSP-RK$(3,3)$ method

$$\begin{aligned}\langle \mathbf{u} \rangle^{*} &= \langle \mathbf{u} \rangle^{(n)} + \Delta t L(\langle \mathbf{u} \rangle^{(n)}) \\ \langle \mathbf{u} \rangle^{**} &= \frac{3}{4}\langle \mathbf{u} \rangle^{(n)} + \frac{1}{4}\langle \mathbf{u} \rangle^{*} + \frac{1}{4}\Delta t L(\langle \mathbf{u} \rangle^{*}) \\ \langle \mathbf{u} \rangle^{(n+1)} &= \frac{1}{3}\langle \mathbf{u} \rangle^{(n)} + \frac{2}{3}\langle \mathbf{u} \rangle^{**} + \frac{2}{3}\Delta t L(\langle \mathbf{u} \rangle^{**})\end{aligned} \tag{4.39}$$

would be the choice for a third-order scheme. In the equations above the superscript denotes the time-level, i.e., $\langle \mathbf{u} \rangle^{*} = \langle \mathbf{u} \rangle(t_{*})$. Both methods allow for a timestep of the same size as the forward Euler method. It is interesting to note that no explicit four-stage fourth-order SSP-RK method exists (e.g., Gottlieb et al., 2009). Therefore, to reach orders of accuracy of four or higher, m must be larger than p.

Since the time-step of explicit methods is restricted by the fastest time-scale in the system, the preferred applications where explicit methods are favored are those involving non-stiff time-accurate problems. On the other hand, implicit methods overcome the CFL restriction at the expense of requiring the solution of large systems of equations at each time-step. In the semi-implicit approach, only the stiff part of the equations is treated implicitly. The implicit and semi-implicit methods are advantageous, for example, when considering systems with widely different time-scales or for obtaining steady-state solutions. Although significantly larger time-steps can be used with implicit or semi-implicit methods from the point of view of stability, retaining a sufficient accuracy places a limit on the permissible size of the time-step also for these methods. Therefore, whether such methods yield an advantage over explicit methods is highly problem-dependent.

4.2 Constrained transport for divergence-free fields

By applying the finite volume method using the algorithms described in section 4.1, any multi-dimensional system of hyperbolic conservation laws can, in principle, be numerically solved. When considering the MHD equations in a multi-dimensional setting, the problem of accommodating the divergence-free evolution of the magnetic field into the numerical algorithm must be addressed.

A pragmatic approach to the problem is to update the magnetic field using exactly the same algorithm as applied to the other variables. In other words, the methods of section 4.1 are applied to the hyperbolic form of Eq. (4.2) given by

$$\partial_t \mathbf{B} + \nabla \cdot (\mathbf{vB} - \mathbf{Bv}) = 0 \tag{4.40}$$

assuming $\mathbf{E} = -\mathbf{v} \times \mathbf{B}$ and $\nabla \cdot \mathbf{B} = 0$. In general, this will result in a magnetic field with a non-zero divergence on the discrete level which causes unphysical acceleration of the plasma parallel to the field. Then, in order to prevent the accumulation of numerical errors due to the non-vanishing divergence, some additional strategy is introduced. Such strategies include projecting the magnetic field to the space of divergence-free fields by solving a Poisson equation at every nth time-step or introducing additional terms into the model equations to damp and/or transport the divergence to the edges of the computational domain (e.g., Dedner et al., 2002).

A different approach is to carry the structure of Eq. (4.2) over to the discrete level so that the evolution of the magnetic field remains divergence-free to machine precision in the chosen discretization in the case that the initial field is divergence-free. Algorithms sharing this property are generally called *constrained transport* (CT) methods after Evans and Hawley (1988). Moreover, the CT method can be constructed in such a way that the reconstruction and upwind properties of the scheme are consistent with the divergence-free constraint and therefore consistently take into account the different smoothness property of the magnetic field. Schemes with these properties are denoted *consistent constrained transport* (CCT) methods in this thesis.

To illustrate the construction of the CCT scheme, consider the z-component of Eq. (4.2) in a Cartesian setting,

$$\partial_t B_z + \partial_x E_y - \partial_y E_x = 0, \tag{4.41}$$

and let the domain be discretized by rectangular cuboids of size $\Delta x \times \Delta y \times \Delta z$. The discrete evolution equation is now obtained by considering the integral form of Eq. (4.41):

$$\partial_t \widehat{B}_{z;i,j,k+\frac{1}{2}} = -\frac{\overline{E}_{y;i+\frac{1}{2},j,k+\frac{1}{2}} - \overline{E}_{y;i-\frac{1}{2},j,k+\frac{1}{2}}}{\Delta x} + \frac{\overline{E}_{x;i,j+\frac{1}{2},k+\frac{1}{2}} - \overline{E}_{x;i,j-\frac{1}{2},k+\frac{1}{2}}}{\Delta y} \tag{4.42}$$

where

$$\widehat{B}_{z;i,j,k\pm\frac{1}{2}} = \frac{1}{\Delta x \Delta y} \int_{x_{i-\frac{1}{2}}}^{x_{i+\frac{1}{2}}} \int_{y_{j-\frac{1}{2}}}^{y_{j+\frac{1}{2}}} B_z(x, y, z_{k\pm\frac{1}{2}}, t)\, dx\, dy \tag{4.43}$$

$$\overline{E}_{y;i\pm\frac{1}{2},j,k\pm\frac{1}{2}} = \frac{1}{\Delta y} \int_{y_{j-\frac{1}{2}}}^{y_{j+\frac{1}{2}}} E_y(x_{i\pm\frac{1}{2}}, y, z_{k\pm\frac{1}{2}}, t)\, dy \tag{4.44}$$

$$\overline{E}_{x;i,j\pm\frac{1}{2},k\pm\frac{1}{2}} = \frac{1}{\Delta x} \int_{x_{i-\frac{1}{2}}}^{x_{i+\frac{1}{2}}} E_x(x, y_{j\pm\frac{1}{2}}, z_{k\pm\frac{1}{2}}, t)\, dx \tag{4.45}$$

Thus, the discrete magnetic field data in the CCT formalism are the surface-averaged magnetic field components $\widehat{B}$ evolved by line-averaged electric field components $\overline{E}$. Since the magnetic field components are located at the cell faces, the method yields a so-called *staggered* discretization.

The preservation of the volume-averaged divergence of the magnetic field is a fundamental built-in property of the CCT method. Integrating $\nabla \cdot \mathbf{B}$ over the cell $\Omega_{i,j,k}$ of volume $V = \Delta x \Delta y \Delta z$ yields

$$\begin{aligned}\langle \nabla \cdot \mathbf{B} \rangle_{i,j,k} &\equiv \frac{1}{\Delta x \Delta y \Delta z} \int_V \nabla \cdot \mathbf{B} \, dV \\ &= \frac{\widehat{B}_{x;i+\frac{1}{2},j,k} - \widehat{B}_{x;i-\frac{1}{2},j,k}}{\Delta x} + \frac{\widehat{B}_{y;i,j+\frac{1}{2},k} - \widehat{B}_{y;i,j-\frac{1}{2},k}}{\Delta y} + \frac{\widehat{B}_{z;i,j,k+\frac{1}{2}} - \widehat{B}_{z;i,j,k-\frac{1}{2}}}{\Delta z}\end{aligned}$$

Taking the time-derivative and using the discretized induction equations, i.e., Eq. (4.42) for $\partial_t \widehat{B}_z$ and similar expressions for $\partial_t \widehat{B}_x$ and $\partial_t \widehat{B}_y$, gives exactly the result

$$\partial_t (\langle \nabla \cdot \mathbf{B} \rangle)_{i,j,k} = 0.$$

Therefore, the magnetic field will remain divergence-free up to machine precision if the initial field is divergence-free. It is also to be noted that due to the staggered collocation, the continuity property of the normal component of the magnetic field in the Rankine-Hugoniot jump conditions at the cell faces is naturally satisfied in the CCT method.

Following a path similar to the derivation of the FV algorithm, the semi-discrete update of the face-averaged magnetic field components is given by an equation analogous to Eq. (4.42) where the exact line-averaged electric fields are replaced by numerical approximations $\overline{\mathcal{E}}$. Thus, the essential step is to find such approximations with sufficient accuracy and stability properties, just as in the numerical flux computation for the FV scheme. Again, since the need is to find electric fields line-averaged along the cell face edges, reconstruction procedures must be applied to obtain the necessary variables at the face edges. Moreover, the mixing of volume-averaged and face-averaged quantities complicates the algorithms.

Finding appropriate approximations to the line-averaged electric fields has proved to be a challenge. In most approaches, the algorithm used for calculating the numerical fluxes in the FV sub-scheme is also applied to the induction equation and the electric fields are then obtained by some arithmetic average of the resulting fluxes. In other words, the relation

$$\partial_t \mathbf{B} = -\nabla \times \mathbf{E} = \nabla \cdot \begin{pmatrix} 0 & E_z & -E_y \\ -E_z & 0 & E_x \\ E_y & -E_x & 0 \end{pmatrix} \tag{4.46}$$

is used, and upon using the FV scheme numerical fluxes $\widehat{\boldsymbol{\mathcal{F}}}$, $\widehat{\boldsymbol{\mathcal{G}}}$ and $\widehat{\boldsymbol{\mathcal{H}}}$ are obtained. Then, as done by several practitioners (e.g., Balsara and Spicer, 1999, Ziegler,

2004), the electric field $\overline{\mathcal{E}}_{z;i+\frac{1}{2},j+\frac{1}{2},k}$ (approximating $\overline{E}_{z;i+\frac{1}{2},j+\frac{1}{2},k}$) is obtained by averaging the numerical fluxes from adjacent faces:

$$\overline{\mathcal{E}}_{z;i+\frac{1}{2},j+\frac{1}{2},k} = \frac{1}{4}\left(-\widehat{\boldsymbol{\mathcal{F}}}_{y;i+\frac{1}{2},j,k} - \widehat{\boldsymbol{\mathcal{F}}}_{y;i+\frac{1}{2},j+1,k} + \widehat{\boldsymbol{\mathcal{G}}}_{x;i,j+\frac{1}{2},k} + \widehat{\boldsymbol{\mathcal{G}}}_{x;i+1,j+\frac{1}{2},k}\right). \tag{4.47}$$

Since the numerical fluxes are defined at different locations, this amounts to calculating a spatial average. Various methods to avoid this have been considered. For instance, Balsara (2004) reconstructs the needed variables to the cell face edge in consideration and calculates the numerical fluxes at that point, and then averages each such contribution from the four neighboring cells. Following a somewhat simpler idea, Gardiner and Stone (2005) project the face-centered numerical fluxes to the location of the electric field components at the face edges, and then calculate a local average. The problem with using a procedure that averages numerical fluxes is that the obtained electric field is not properly upwinded. To overcome the resulting numerical instabilities, Balsara et al. (2009) and Gardiner and Stone (2005) propose to use switches that essentially alter between different algorithms depending on the local flow characteristics in a more or less ad hoc fashion. Although such schemes can function well, a natural extension of the upwinded and non-oscillatory FV base scheme to the calculation of the electric fields would be highly desirable.

The construction of a method by which this can be accomplished is the main subject of Article V. The main observation is that in order to arrive at an approximation for the electric field that does not use ad hoc face to edge interpolations, it is necessary to consider the inherent multi-dimensionality of the problem at the face edges. In other words, at the face edge where $\overline{E}_{z;i+\frac{1}{2},j+\frac{1}{2},k}$ is located, the four states due to the cells $\Omega_{i,j,k}, \Omega_{i+1,j,k}, \Omega_{i,j+1,k}$ and $\Omega_{i+1,j+1,k}$ constitute a two-dimensional Riemann problem that must be reflected in the approximation to the electric field. The approach in Article V is to consider a Riemann fan consisting only of the fastest propagating waves, similar to the HLL approximate Riemann solver. Then, in the semi-discrete limit, an averaging of the two Riemann fans can be calculated. The result (Eq. (2.40) in Article V) is

$$\begin{aligned}\overline{\mathcal{E}}_{z;\xi} = {} & \frac{a_\xi^- b_\xi^- \overline{E}_{z;\xi}^{\,i+1,j+1,k} - a_\xi^- b_\xi^+ \overline{E}_{z;\xi}^{\,i+1,j,k} - a_\xi^+ b_\xi^- \overline{E}_{z;\xi}^{\,i,j+1,k} + a_\chi^+ b_\chi^+ \overline{E}_{z;\xi}^{\,i,j,k}}{(a_\xi^+ - a_\xi^-)(b_\xi^+ - b_\xi^-)} \\ & - \frac{a_\xi^+ a_\xi^-}{a_\xi^+ - a_\xi^-}\left[\overline{p}_{2;\xi}^{\,i+1,j,k} - \overline{p}_{2;\xi}^{\,i,j,k}\right] + \frac{b_\xi^+ b_\xi^-}{b_\xi^+ - b_\xi^-}\left[\overline{p}_{1;\xi}^{\,i,j+1,k} - \overline{p}_{1;\xi}^{\,i,j,k}\right]\end{aligned} \tag{4.48}$$

where the index $i+\frac{1}{2}, j+\frac{1}{2}, k$ is denoted by ξ, a_ξ and b_ξ are the signal speeds in the x_1 and x_2 directions, respectively, and p indicates the reconstructed magnetic field components. Additionally, the superscripted index denotes the cell from which the reconstruction function is to be employed.

Examining Eq. (4.48), it is seen that it reduces to the correct one-dimensional flux for cases that are aligned with the coordinate axes x or y or with the diagonal $x-y$. As an inherent four-state formula with two independent diffusion terms, a similar formula could not be obtained by any simple averaging procedure. Furthermore, Eq. (4.48) gives the electric field directly without a need to consider the numerical fluxes of the hyperbolic form of the induction equation.

It is interesting to note the connection between Eq. (4.48) and the method derived for solving 2D Hamilton-Jacobi equations presented by Kurganov et al. (2002). Since in the CCT formalism the staggered magnetic field components can equivalently be represented by the vector potential, each component of the induction equation in terms of the vector potential for a given velocity field has the form of a Hamilton-Jacobi equation,

$$\partial_t \mathbf{A} + \mathbf{E}(\partial_{x_i} A_j) = 0. \tag{4.49}$$

Therefore, upwind methods used to solve such equations can be applied to the induction equation. This relation was recently used to derive a CCT method by Ziegler (2011).

4.2.1 Reconstructing the magnetic field

In order to calculate the electric field at the cell face edges, the magnetic field and velocity need to be reconstructed to those locations. While the velocity field can be reconstructed using the procedures discussed in section 4.1.2, the magnetic field needs to be treated differently due to the different smoothness properties.

Consider the x-oriented face at $x_{i+\frac{1}{2}}$ of cell $\Omega_{i,j,k}$. Due to the staggered co-location of the magnetic field, the component $\widehat{B}_{x;i+\frac{1}{2},j,k}$ is available at the face, and provides a (second-order) approximation to $B_x(x_{i+\frac{1}{2}}, y_j, z_k)$. Therefore, no additional reconstruction of B_x is needed for a second-order calculation of the FV numerical flux function $\boldsymbol{\mathcal{F}}_{i+\frac{1}{2},j,k}$. The B_x component is also needed at the edges for the electric field calculation, which necessitates transverse reconstructions. For a second order scheme following the TVD methodology, this can be constructed as

$$B_x(x_{i+\frac{1}{2}}, y, z) = \widehat{B}_{x;i+\frac{1}{2},j,k} + (\delta_y B_x)_{i+\frac{1}{2},j,k}(y - y_j) + (\delta_z B_x)_{i+\frac{1}{2},j,k}(z - z_k) \tag{4.50}$$

where the slopes are calculated and limited as in section 4.1.2. By including higher-order polynomials, as for instance cataloged in Balsara et al. (2009), the order of accuracy can be increased.

In order to calculate the numerical fluxes in the y and z directions, B_x must also be reconstructed to the other faces. In a pragmatic approach (e.g., Ziegler, 2004,

2011), B_x can be obtained at any point in the cell by linearly interpolating in the x-direction the two face values $B_x(x_{i\pm\frac{1}{2}}, y, z)$ given by Eq. (4.50). For instance, at the $(x_i, y_{j+\frac{1}{2}}, z_k)$ position, this amounts to the following averaging:

$$B_x(x_i, y_{j+\frac{1}{2}}, z_k) = \frac{1}{2}\left(\widehat{B}_{x;i+\frac{1}{2},j,k} + \frac{\Delta y}{2}(\delta_y B_x)_{i+\frac{1}{2},j,k} + \widehat{B}_{x;i-\frac{1}{2},j,k} + \frac{\Delta y}{2}(\delta_y B_x)_{i-\frac{1}{2},j,k}\right) \tag{4.51}$$

Such a procedure does not give an analytically divergence-free field which would facilitate the construction of prolongation and restriction operations for adaptively refined meshes. In order to obtain such a reconstruction, quadratic terms need to be included in the expression for B_x (e.g., Balsara et al., 2009).

4.3 Extension to curvilinear geometries

When conducting simulations of the solar corona on a global scale, i.e., when the spatial domain extends over a large fraction of the solar radius in each direction and the solar surface (or the base of the corona) defines a boundary of the domain, it becomes necessary to include the curvature of the Sun in the model. Including a curved surface as a domain boundary brings about the need to refine the numerical algorithm to handle such boundaries.

Loosely speaking, three different strategies exist to tackle the problem. In the first approach, a specialized treatment is applied to cells near the boundary whereas the standard Cartesian algorithm on a rectangular mesh is retained away from the boundary. In the second approach, the rectangular mesh is abandoned in favor of a more general gridding technique so that the mesh conforms to the boundary surface, however, retaining the Cartesian coordinate system. The third approach is to write the equations using curvilinear coordinates suited to the problem and discretizing the domain using a regular rectangular mesh in the curvilinear basis.

The path chosen in this thesis is to approximate the Sun as a sphere and solve the MHD equations using spherical coordinates. Therefore, the numerical methods described in the previous sections must be generalized to accommodate orthogonal curvilinear coordinate systems. This task was undertaken in Article IV for the finite volume scheme and in Article V for the CCT scheme, and will be discussed next.

When considering coordinate systems where the coordinate surfaces are curved, the components of the metric tensor are no longer given by the Kronecker delta. For orthogonal coordinates, the metric is diagonal with components $g_{ii} = h_i^2$ where h_i are the metric scale factors. For such systems, the conservation law (Eq.

(4.1)) becomes

$$\frac{\partial \mathbf{u}}{\partial t} + \frac{1}{h_1 h_2 h_3}\left[\frac{\partial}{\partial x_1}\left(h_2 h_3 \mathbf{F}\right) + \frac{\partial}{\partial x_2}\left(h_1 h_3 \mathbf{G}\right) + \frac{\partial}{\partial x_3}\left(h_1 h_2 \mathbf{H}\right)\right] = \mathbf{S} \quad (4.52)$$

where x_i are the curvilinear coordinates and $\mathbf{S}$ is a geometrical source term which is a function of $\mathbf{u}$ and the scale factors h_i and their derivatives.

The construction of a FV scheme to solve Eq. (4.52) can, in principle, be performed by suitably applying the methods described in section 4.1. In contrast to following a heuristic path, the approach in Article IV is to account for the geometric terms in a rigorous way by performing a systematic derivation of a FV method for solving Eq. (4.52). The algorithm is constructed by utilizing the semi-discrete limit, as well as accounting only for the fastest propagating waves due to the discontinuous data at the cell interfaces. With these assumptions, a numerical spatial operator $\mathcal{L}$ analogous to Eq. (4.15) of arbitrary order can be derived. The result can be written as

$$\begin{aligned}\mathcal{L}|_{i,j,k} = \langle \boldsymbol{\mathcal{S}} \rangle_{i,j,k} - \frac{1}{V_{i,j,k}}\Big[& A_{1;i+\frac{1}{2},j,k}\widehat{\boldsymbol{\mathcal{F}}}_{i+\frac{1}{2},j,k} - A_{1;i-\frac{1}{2},j,k}\boldsymbol{\mathcal{F}}_{i-\frac{1}{2},j,k} \\ + & A_{2;i,j+\frac{1}{2},k}\widehat{\boldsymbol{\mathcal{G}}}_{i,j+\frac{1}{2},k} - A_{2;i,j-\frac{1}{2},k}\widehat{\boldsymbol{\mathcal{G}}}_{i,j-\frac{1}{2},k} \\ + & A_{3;i,j,k+\frac{1}{2}}\widehat{\boldsymbol{\mathcal{H}}}_{i,j,k+\frac{1}{2}} - A_{3;i,j,k-\frac{1}{2}}\widehat{\boldsymbol{\mathcal{H}}}_{i,j,k-\frac{1}{2}}\Big]\end{aligned} \quad (4.53)$$

where $V_{i,j,k}$ denotes the volume of the cell and $A_{\eta;\chi}$ the area of the cell face in the η-direction at the position given by the index χ. The numerical fluxes in the x_1 direction are

$$\widehat{\boldsymbol{\mathcal{F}}}_{\xi} = \frac{a_{\xi}^{+}\widehat{\mathbf{F}}_{\xi}^{-} - a_{\xi}^{-}\widehat{\mathbf{F}}_{\xi}^{+}}{a_{\xi}^{+} - a_{\xi}^{-}} + \frac{a_{\xi}^{+}a_{\xi}^{-}}{a_{\xi}^{+} - a_{\xi}^{-}}\left[\widehat{\mathbf{u}}_{\xi}^{+} - \widehat{\mathbf{u}}_{\xi}^{-}\right] \quad (4.54)$$

where ξ denotes the subscript $\xi \equiv i \pm \frac{1}{2}, j, k$ and

$$\begin{aligned}\widehat{\mathbf{F}}_{i-\frac{1}{2},j,k}^{\pm} \equiv & \frac{1}{A_{1;i-\frac{1}{2},j,k}}\int_{x_{2;j-\frac{1}{2}}}^{x_{2;j+\frac{1}{2}}}\int_{x_{3;k-\frac{1}{2}}}^{x_{3;k+\frac{1}{2}}} d\eta d\sigma \times \\ & h_2(x_{1;i-\frac{1}{2}},\eta,\sigma)h_3(x_{1;i-\frac{1}{2}},\eta,\sigma)\mathbf{F}(\mathbf{p}_{i-\frac{1}{2}\pm\frac{1}{2},j,k}(x_{1;i-\frac{1}{2}},\eta,\sigma))\end{aligned} \quad (4.55)$$

is the face-averaged flux at the $x_{1;i-\frac{1}{2}}$ face in the cell $\Omega_{i,j,k}$. Similarly, $\widehat{\mathbf{u}}_{\xi}^{\pm}$ denote the two face-averages of $\mathbf{u}$ obtained by integrating the two reconstruction functions of the adjacent cells at their common interface.

While Eq. (4.53), Eq. (4.54) and Eq. (4.55) define the spatial solution operator for the FV base scheme, the CCT method also needs to be modified in a similar manner. To illustrate, consider the third component of the induction equation

(equation (2.2) in Article V). A direct application of the Kelvin-Stokes theorem yields the spatial discretization

$$\partial_t \widehat{\mathcal{B}}_{3;i,j,k\pm\frac{1}{2}} = -\frac{L_{2;i+\frac{1}{2},j,k\pm\frac{1}{2}}\overline{\mathcal{E}}_{2;i+\frac{1}{2},j,k\pm\frac{1}{2}} - L_{2;i-\frac{1}{2},j,k\pm\frac{1}{2}}\overline{\mathcal{E}}_{2;i-\frac{1}{2},j,k\pm\frac{1}{2}}}{A_{3;i,j,k\pm\frac{1}{2}}} + \frac{L_{1;i,j+\frac{1}{2},k\pm\frac{1}{2}}\overline{\mathcal{E}}_{1;i,j+\frac{1}{2},k\pm\frac{1}{2}} - L_{1;i,j-\frac{1}{2},k\pm\frac{1}{2}}\overline{\mathcal{E}}_{1;i,j-\frac{1}{2},k\pm\frac{1}{2}}}{A_{3;i,j,k\pm\frac{1}{2}}} \quad (4.56)$$

where $L_{\nu;\chi}$ is the length of the ν-directed face edge at the coordinates given by the index χ. With this discretization, the time-derivative of the volume-averaged divergence, given by

$$\begin{aligned}(\langle\nabla\cdot\boldsymbol{\mathcal{B}}\rangle_{i,j,k})V_{i,j,k} =& A_{1;i+\frac{1}{2},j,k}\widehat{\mathcal{B}}_{1;i+\frac{1}{2},j,k} - A_{1;i-\frac{1}{2},j,k}\widehat{\mathcal{B}}_{1;i-\frac{1}{2},j,k} \\ &+ A_{2;i,j+\frac{1}{2},k}\widehat{\mathcal{B}}_{2;i,j+\frac{1}{2},k} - A_{2;i,j-\frac{1}{2},k}\widehat{\mathcal{B}}_{2;i,j-\frac{1}{2},k} \\ &+ A_{3;i,j,k+\frac{1}{2}}\widehat{\mathcal{B}}_{3;i,j,k+\frac{1}{2}} - A_{3;i,j,k-\frac{1}{2}}\widehat{\mathcal{B}}_{3;i,j,k-\frac{1}{2}}, \end{aligned} \quad (4.57)$$

is exactly zero. Properly upwinded electric fields are then obtained in a manner analogous to the Cartesian case by performing an averaging over two Riemann fans.

4.4 The second-order scheme

Having introduced the various algorithms needed for performing the specific individual tasks described in the previous sections, the entire scheme making up the numerical MHD solver employed in this thesis can now be assembled. A key decision in this process is the choice of the order of accuracy of the scheme. Considering the design criteria laid out in the beginning of the chapter, a good compromise between accuracy and simplicity was deemed to be provided by a second-order scheme. The specifics of the numerical algorithm are detailed next.

The semi-discrete methodology allows the algorithm to be presented and implemented in a logically straight-forward way. With the second-order SSP Runge-Kutta scheme, Eq. (4.38), being the primary choice for the temporal integration, the overall flow of the program is illustrated by Fig. 4.1.

The calculation of the spatial operator $\mathcal{L}$ differs depending on whether the FV scheme or the CCT scheme is applied. In the case of the FV scheme, the operator is given by Eq. (4.53), with Eq. (4.54) and Eq. (4.55) providing the formulas for the x_1-direction. To second-order, Eq. (4.55) can be evaluated with a midpoint rule, giving

$$\widehat{\mathbf{F}}^{\pm}_{i-\frac{1}{2},j,k} \approx \mathbf{F}(\mathbf{p}_{i-\frac{1}{2}\pm\frac{1}{2},j,k}(x_{1;i-\frac{1}{2}}, \widehat{x2}_{i-\frac{1}{2}}, \widehat{x3}_{i-\frac{1}{2}})) \quad (4.58)$$

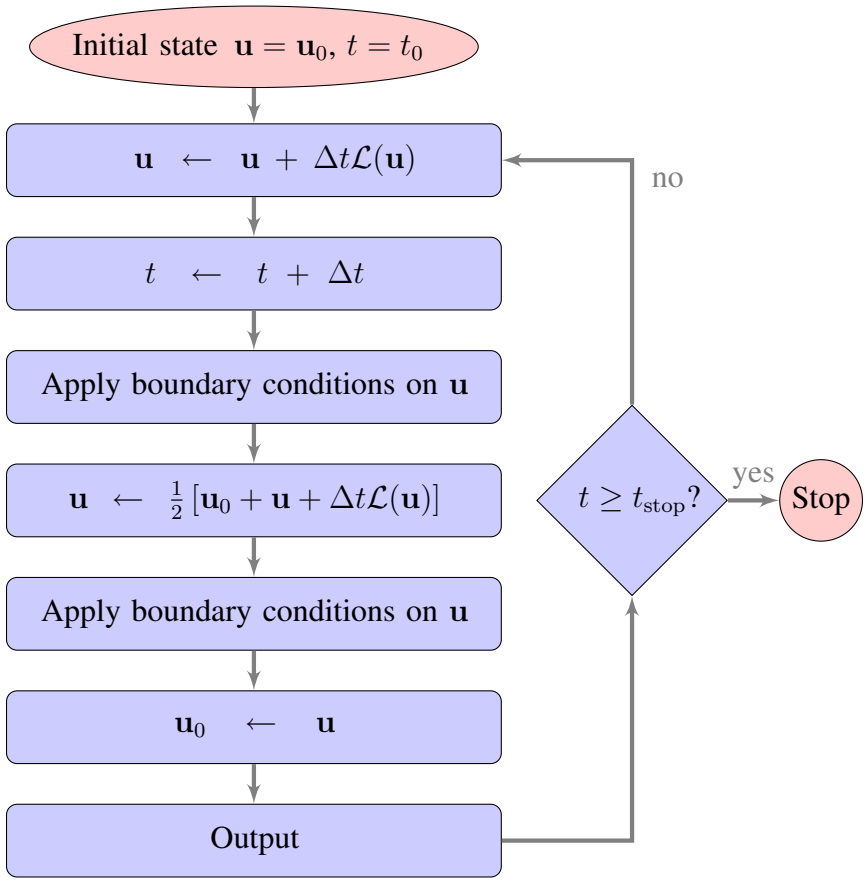

Figure 4.1: Flow-schematic of the computation of the second-order algorithm.

where the input to the reconstruction function are the coordinates x_2 and x_3 area-averaged over the face at $x_{1;i-\frac{1}{2}}$ in the cell $\Omega_{i,j,k}$. The reconstruction function $\mathbf{p}$ is chosen to be a linear function with a TVD limiter in accordance with the second-order assumption, i.e.

$$\mathbf{p}_{i,j,k}(x_1, x_2, x_3) = \langle \mathbf{u} \rangle_{i,j,k} + \sum_{l=1}^{3} \mathbf{s}_l (x_l - \langle x \rangle_{l;i,j,k}) \tag{4.59}$$

where $\mathbf{s}_l$ is a limited approximation for the derivative of $\mathbf{u}$ in the direction x_l. For the x_1-direction it is given by

$$\mathbf{s}_1 = \text{limiter}\left(\frac{\mathbf{u}_{i+1,j,k} - \mathbf{u}_{i,j,k}}{\langle x \rangle_{1;i+1,j,k} - \langle x \rangle_{1;i,j,k}}, \frac{\mathbf{u}_{i+1,j,k} - \mathbf{u}_{i-1,j,k}}{\langle x \rangle_{1;i+1,j,k} - \langle x \rangle_{1;i-1,j,k}}, \frac{\mathbf{u}_{i,j,k} - \mathbf{u}_{i-1,j,k}}{\langle x \rangle_{1;i,j,k} - \langle x \rangle_{1;i-1,j,k}}\right) \tag{4.60}$$

where the function limiter is any one of the standard slope limiters, e.g., the minmod function or the van Leer limiter.

When $\mathbf{u}$ in Fig. 4.1 represents the face-averaged magnetic field components, $\mathcal{L}$ is instead given by the CCT method. For $\widehat{\mathcal{B}_3}$ (approximating $\widehat{B_3}$), it is given by an expression identical to Eq. (4.56) with the upwinded electric field components given by an expression analogous to Eq. (4.48) Evaluating the line integral to second order gives the formula

$$\overline{E}_{2;i+\frac{1}{2},j,k+\frac{1}{2}} \approx E_2(x_{1;i+\frac{1}{2}}, \overline{x}_{2;i+\frac{1}{2},j,k+\frac{1}{2}}, x_{3;k+\frac{1}{2}}) \tag{4.61}$$

The reconstruction of the components of the magnetic field follows the pragmatic method discussed in section 4.2.1. For instance, at the $x_{1;i+\frac{1}{2}}$ face, the $\mathcal{B}_1$ component is given by

$$\begin{aligned} &\mathcal{B}_1(x_{1;i+\frac{1}{2}}, x_2, x_3) \\ &= \widehat{\mathcal{B}}_{1;i+\frac{1}{2},j,k} + (\delta_2 \mathcal{B}_1)_{i+\frac{1}{2},j,k}(x_2 - \widehat{x_{2j}}) + (\delta_3 \mathcal{B}_1)_{i+\frac{1}{2},j,k}(x_3 - \widehat{x_{3k}}) \end{aligned} \tag{4.62}$$

With all quantities consistently evaluated to second order, the recipe for calculating the full spatial operator $\mathcal{L}$ is completed.

4.5 Further remarks

In the calculations presented in chapter 5, additional measures that improve the accuracy of the solution have been applied. These methods are shortly introduced in this section.

4.5.1 Splitting the magnetic field

In many applications, the magnetic field $\mathbf{B}$ can be characterized as being composed of a field $\mathbf{B}_1$ superposed on a background field $\mathbf{B}_0$,

$$\mathbf{B} = \mathbf{B}_0 + \mathbf{B}_1. \tag{4.63}$$

Especially in cases where additional information regarding $\mathbf{B}_0$ is available, it is advantageous to apply the decomposition to the MHD equations that are solved numerically. In all of the applications considered in this thesis, the magnetic field of the ambient corona includes a strong contribution from a potential magnetic field produced by time-independent subphotospheric sources. Therefore, the decomposition given by Eq. (4.63) with $\mathbf{B}_0$ such that $\partial_t \mathbf{B}_0 = 0$ and $\nabla \times \mathbf{B}_0 = 0$ is explicitly inserted into the MHD equations, and only the dynamic part $\mathbf{B}_1$ is solved for. As a result, the accuracy and robustness of the solution is considerably improved. The resulting equations are given, for instance, by Gombosi et al. (2002).

4.5.2 Employing stretched grids

In order to accurately capture large gradients appearing in the simulations, employing a mesh with a high resolution in areas of particular interest is imperative. In most of the modeling considered in this work, a rectilinear mesh is employed in which the mesh spacing varies from one cell to the next. Typically, in the simulations using spherical coordinates, the grid is finest closest to the solar surface as well as at the equator.

As long as the variation of the mesh spacing is performed for each coordinate separately, the resulting grid retains the logically rectangular indexing, and the scheme described in the previous section can still be directly applied. However, the calculation of the slopes in the reconstruction procedure need to be altered so that the varying grid size is taken into account in order for the slope estimates to retain their formal order of accuracy in smooth regions of the flow. Another subtle issue to be considered is that the limiters may not retain their stability property if they are applied unmodified to an irregular grid (Berger et al., 2005).

Chapter 5

Results and Discussion

In this chapter, the main findings of the numerical calculations of erupting CMEs embedded in the model environments introduced in chapter 3 are presented with a focus on the waves and shocks generated by the eruption. A central quantity in this context is the relative change of the density compared to the background ambient density,

$$r_{\mathrm{c}}(\mathbf{r}, t) = \rho(\mathbf{r}, t)/\rho(\mathbf{r}, t = 0). \tag{5.1}$$

By plotting r_{c} at a given time, the compression ratio along the entire shock front for that time can be distinguished.

5.1 Overview of eruption dynamics

The onset of the CME induces a rich set of highly non-trivial dynamical features in the surrounding corona. Nevertheless, for the parameter regimes considered, the response of the plasma to the expanding eruption is similar in all the studied models in a number of respects. The common features of the dynamics can be summarized as follows:

- The rise and expansion of the erupting structure causes a wave ahead of it to be quickly formed.
- For a large area ahead of the eruption complex, depending on the profile of the Alfvén speed, the wave steepens to form a shock.
- As the CME continues to push the plasma ahead of it, the shock strength becomes highest at the leading edge and decreases towards the flanks of the erupting structure. The leading shock structure reaches down and sweeps the solar surface, however, decreasing in strength or degenerating to a fast-mode wave at the surface.

- Immediately behind the shock front, a highly compressed post-shock region with an elevated temperature is formed, being most prominent at the leading edge.
- In the vicinity of the flux rope, a region with a lower temperature is formed. In the non-axisymmetric case, a current sheet with an elevated temperature is formed below the flux rope.

5.2 Driven vs. blast wave scenario

The left panels in Fig. 5.1 present the dynamics induced by the lift-off of the flux rope in the Cartesian local model described in section 3.3. The shock wave, although driven by the flux rope rising under the influence of the artificial force, propagates in all directions from the driver and retains a quasi-circular shape. It nevertheless remains strongest near the leading edge of the shock. Thus, based on geometry alone, the shock cannot be distinguished from that of a blast wave for the parameter regime considered. This is further illustrated in the right panels of Fig. 5.1 that presents an identical simulation with the exception that for $t > 70$ s, the direction of the artificial force is reversed causing the flux rope to rapidly decelerate and come to a halt. Such a scenario can be considered to correspond to that of a filament failing to erupt due to the confining overlying field such as has been observed by the Transition Region and Coronal Explorer (TRACE) (Ji et al., 2003) and theoretically investigated by Török and Kliem (2005). The figures show that even in such a case, a propagating shock wave can be launched. The geometry of the wave front is very similar, but the shock is weaker and loses its strength as it expands freely into the medium. In order to follow the shock for a longer period of time, a larger domain must be considered as in Article I. Carrying out such a calculation reveals that at later times, the shock becomes more elongated in the direction of the driver and loses its initial quasi-circular shape (see Figure 2 in Article I). This is due to the spatial variation of the Alfvén speed v_A: away from the eruption site along the solar surface v_A decreases, while for heights above $\sim 0.2R_\odot$ the surface v_A increases. Indeed, when entering the region of increasing v_A, the shock starts to escape from the driver (e.g., Figure 3 in Article I). In this sense, the shock acts more like a freely propagating than a driven wave at this stage. Beyond a few solar radii where v_A is expected to reach it's maximum (e.g., Warmuth and Mann, 2005, Evans et al., 2008), the situation reverses again as the ejecta starts to catch up with the shock.

The results show that depending on the spatial distribution of the Alfvén speed and the motion of the driver, the shock can at times act as a freely propagating blast-type wave, while at other times the wave is driven. As a consequence, the speed and location of the ejecta and an associated type II burst, if generated at the shock nose where the shock is strongest, need not be correlated in any simple way.

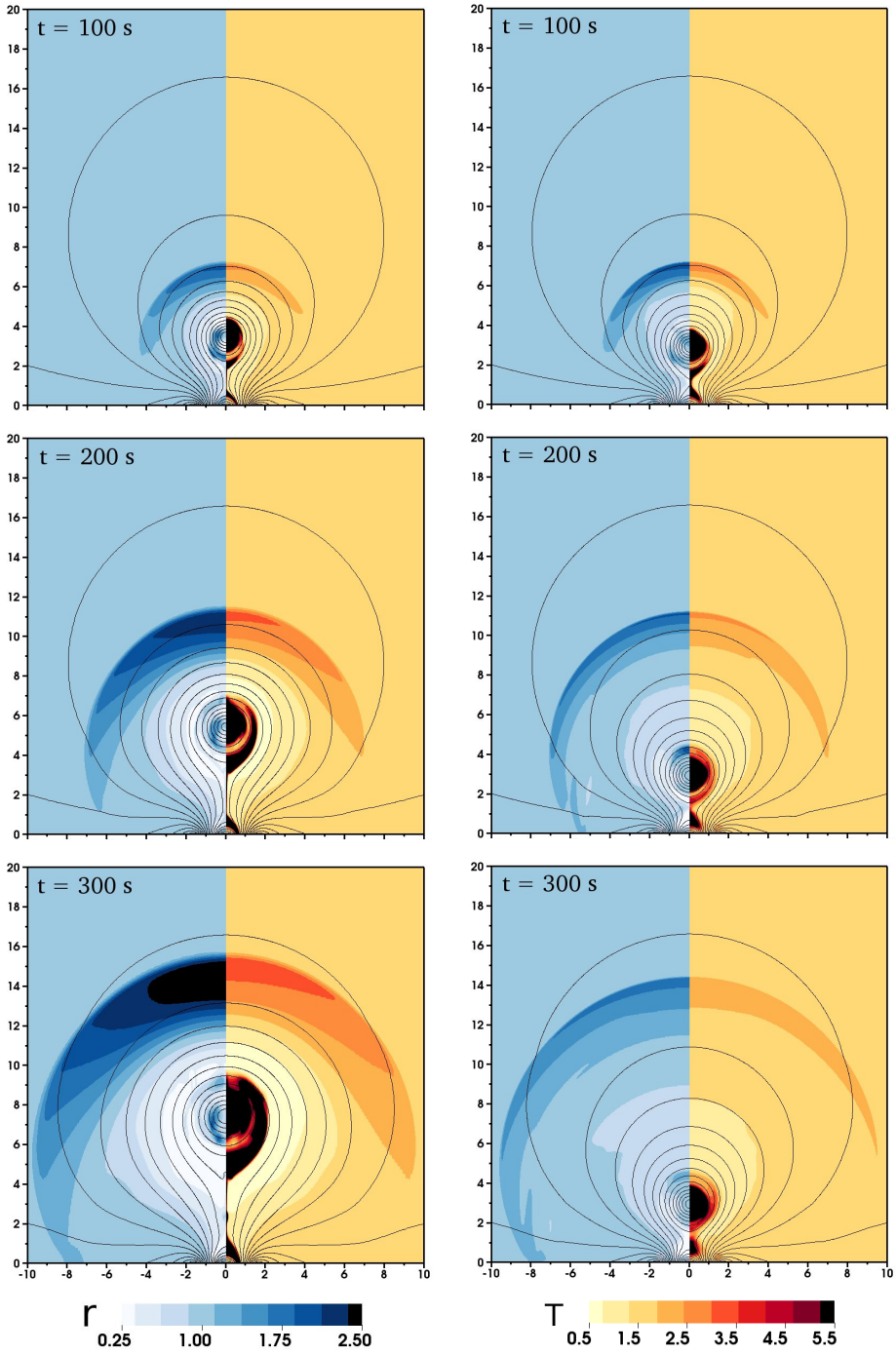

Figure 5.1: Result of the local model at times (from top to bottom) $t = 100$, 200, 300 s. Left: Eruptive event. Right: Confined event. The left halves of the images (blue colors) correspond to r_c, while right halves (red colors) to the temperature in units of MK. Unit of length $l = 10$ Mm.

In the blast vs. driven wave debate of coronal shocks, the flare-related blast wave is often quoted to be caused by the pressure pulse associated with the flare energy release. Since the AR environment is characterized by a low beta plasma it is, however, not clear that the pressure pulse would be able to generate a wave (e.g., Vršnak and Cliver, 2008). The failed eruption simulation result suggests another possibility: if the Alfvén speed decreases sufficiently rapidly, even a relatively small structure that starts to rise but fails to erupt might be able to launch a coronal wave.

5.3 CME - EIT wave - cavity connection

The numerical experiments conducted with the local models show that, within a few minutes from the eruption onset, the flanks of the shock front map all the way down to the coronal base, sweeping the surface as the front expands. Depending on the specific parameters, the shock generally degenerates to a large-amplitude fast-mode wave propagating roughly at the speed of the local magnetosonic speed. This characteristic is consistent with that of a number of well-observed EIT waves.

As described in the previous section, the kinematics of the wave front is sensitive to the spatial distribution of the Alfvén speed. In contrast, the region of depleted density and temperature formed around the flux rope and current sheet depends on the successive stretching of the field lines surrounding the flux rope. Therefore, the feature is attached to the motion of the ejecta, and resembles the expanding bubble or cavity region observed in EUV images in conjunction with CMEs (e.g., Fig. 2.3). Indeed, for the failed eruption, no such cavity is formed. An EIT wave not showing any dimming could be interpreted as evidence for a blast-wave type wave.

The CME-EIT wave connection can effectively be studied using the event-oriented three-dimensional model discussed in section 3.5.2. Figure 5.2 shows the development of the compression ratio at the height $r = 1.05R_{\odot}$. As can be seen, the density enhancement exhibits a complex behavior, with a clear directionality, being stronger in the North-South direction. Later in the event, when the wave enters the concentration of active region fields in the north, the front is broken up into several fronts as the wave refracts due to the high Alfvén speed.

Figure 5.3 shows a side view of the eruption at $t = 2.5$ min. In the left image, an isosurface of $r_{\mathrm{c}} = 1.5$ that visualizes the 3-D structure of the shock is shown. The shock front, although appearing quasi-spherical, rapidly obtains an elongated shape in the direction of the flux rope motion. The shock dome clearly maps down to the surface producing the compression depicted in Fig. 5.2. Later, when the skirt of the shock reaches the region of higher Alfvén speed to the north, the $r_{\mathrm{c}} = 1.5$ isosurface no longer maps all the way down to the surface, but instead terminates higher up. This is also the case for the shock in the east-west direction.

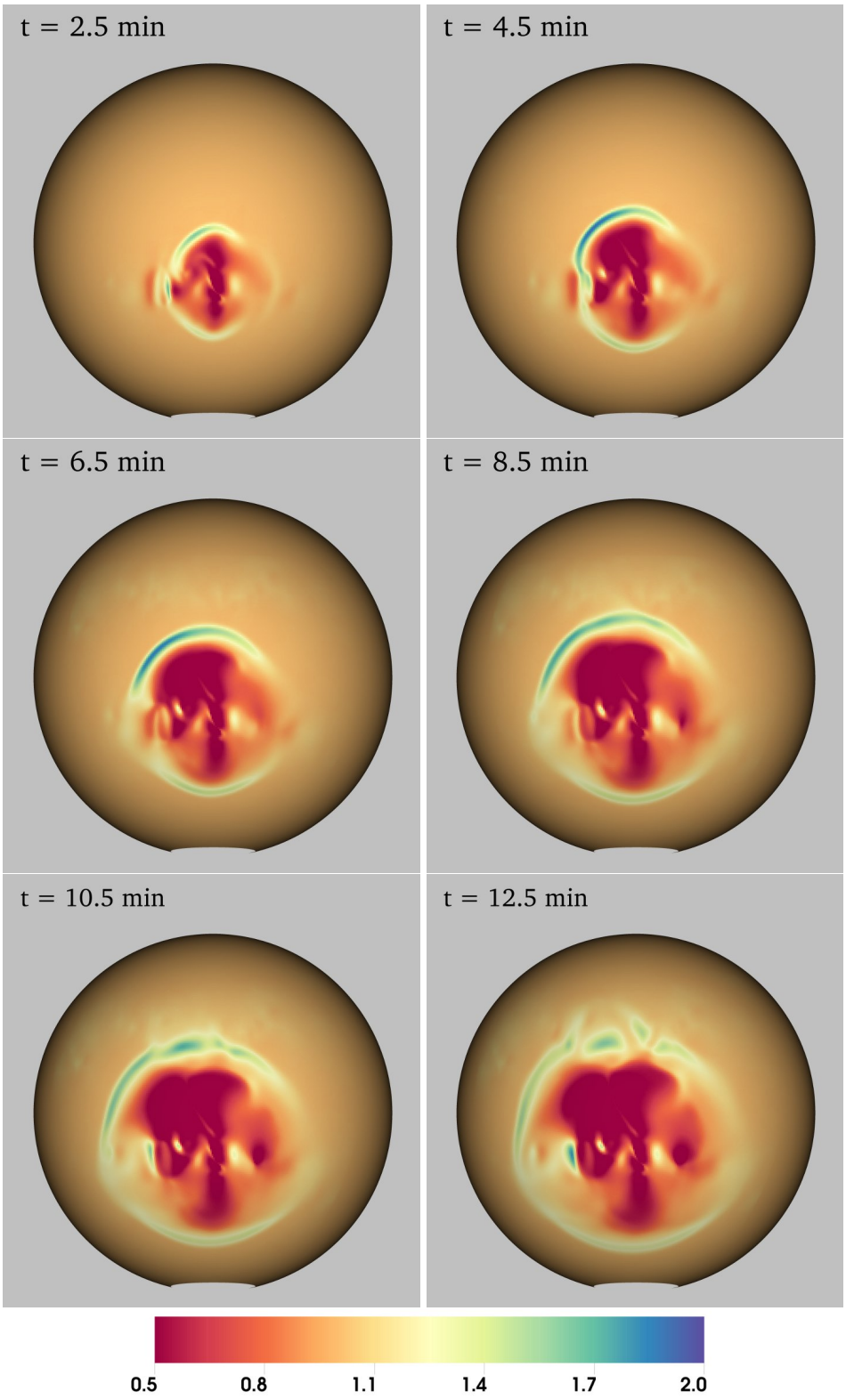

Figure 5.2: Developement of r_c at height $r = 1.05 R_\odot$.

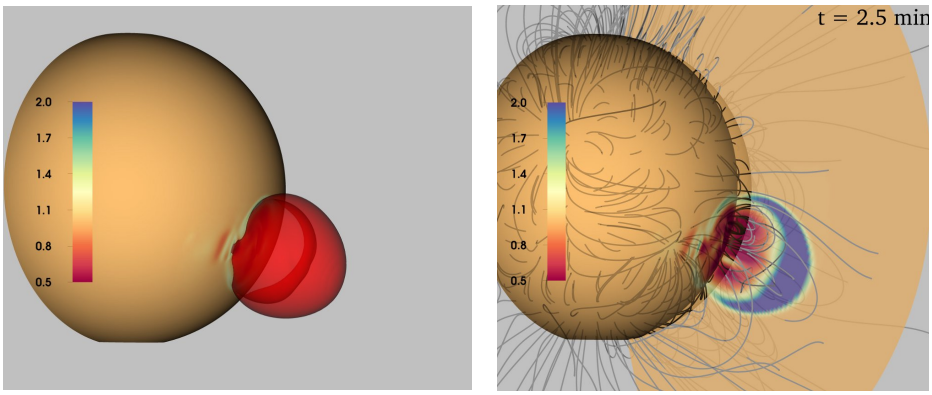

Figure 5.3: Side view at $t = 2.5$ min after onset. The red dome is the isosurface of $r_c = 1.5$. In the right image, a meridional slice of the compression is shown as well as a number of field lines. Also, in both images the compression ratio at $r = 1.05R_\odot$ similar to that in Fig. 5.2 is shown.

Figure 5.4 shows SDO/AIA EUV difference images of the corresponding actual event (Li et al., 2012). The morphology of the image at 06:26 UT shows a clear qualitative similarity with Fig. 5.3. The image to the right in Fig. 5.3 taken seven minutes later shows a complex break up of the wave front. Comparing to Fig. 5.2, this is seen to occur in the simulation at a roughly consistent time. This indicates that the time scales in the simulation are in qualitative agreement with those of the observations. Furthermore, it is interesting to note that the wave front indicated as the secondary wave in the right image in Fig. 5.4 refracts in an eastwardly direction. This is also the case in the simulation for the eastern part of the wave front.

The comparison of the simulation and observations strongly indicate that the outermost EUV wave structure in the observations corresponds to the skirt of the CME-driven shock. The simulations are therefore in accordance with the hybrid interpretation of EIT waves (Patsourakos and Vourlidas, 2012, Cheng et al., 2012). However, it must be noted that the actual observable quantity to compare with is the line-of-sight emission measure. Recently, three-dimensional MHD calculations taking this into account reach similar conclusions regarding the nature of the EIT waves (Downs et al., 2011, Selwa et al., 2012).

5.4 Dependence on heating formulations

As discussed in section 3.4, in order to obtain a realistic solar wind solution that closely reproduces the conditions of the plasma environment in the inner heliosphere, a variety of methods to heat the corona to the observed temperatures and drive the solar wind have been employed in MHD calculations. The effect that altering the governing physics of the simulation has on the dynamics of shocks

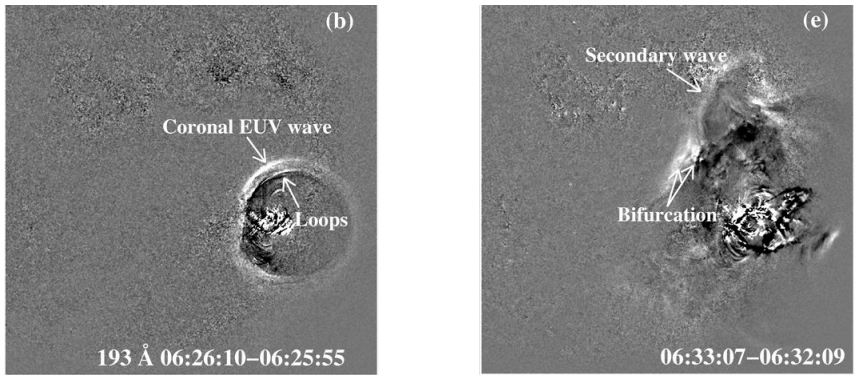

Figure 5.4: Two SDO/AIA 193 Å running difference images of the 2011 June 7 event (Li et al., 2012).

propagating in the solar wind needs to be addressed. A comparative study was undertaken in Article III.

Consider the steady-state wind model using a non-adiabatic polytropic index, shown in the left panel of Fig. 3.2 and hereafter designated P1. The identical steady-state solution can be retained even using $\gamma = 5/3$ by introducing an energy source term Q into Eq. (3.3) that balances the change in the polytropic index, and is given by

$$Q = \nabla \cdot \left[\mathbf{v}_{\mathrm{P1}} P_{\mathrm{P1}} \left(\frac{1}{\gamma - 1} - \frac{1}{\Gamma - 1} \right) \right] \tag{5.2}$$

where $\Gamma = \Gamma(\mathbf{r})$ is the spatially varying polytropic index used in model P1 and $\mathbf{v}_{\mathrm{P1}}$ and P_{P1} are the steady-state velocity and pressure distributions of model P1, respectively. Thereby, the effect of the reduced polytropic index on the dynamics can be studied. The simulation run using Eq. (5.2) is designated P2.

Figure 5.5 shows the temperature and compression ratio at 20 minutes after the onset for both models. The calculation is otherwise identical to that presented in Figures 2 and 3 in Article III, but the flux rope is launched closer to the equator in order to facilitate the comparison to the three-dimensional analogue discussed in the next section. The plot reveals that model P1 compresses the plasma considerably more than model P2, which in turn heats the plasma to higher temperatures than model P1. Noteworthy is that it is not just the shock compression that is affected; also the post-shock regions differ considerably both in temperature and in compression.

The simulations show that when the polytropic index is lowered, the kinetic energy of the shock is transferred increasingly into compressing the plasma rather than heating it. This is consistent with that expected from the Rankine-Hugoniot relations. Furthermore, in the case of model P2, the $r = 4$ limit for standard ideal-MHD with $\gamma = 5/3$ is not violated. This can be understood by noting that

the energy source term, Eq. (5.2), used in P2 is time-independent and behaves smoothly at the shock. Therefore, the integral of the source term over the shock in the Rankine-Hugoniot analysis vanishes, and the ordinary jump conditions are retained. This demonstrates the applicability of the equivalent heating source term approach: the pragmatic method by which momentum and/or energy is added for obtaining the solar wind solution can be chosen at will, and for dynamic simulations involving large flows, an equivalent heat source should be used in order to retain the compressive behavior of an adiabatic gas.

5.5 Comparing 3D and axisymmetric simulations

Ignoring variations of the flow variables in the azimuthal direction in steady-state models of solar wind can be argued to approximate conditions during solar minimum when the coronal plasma appears less asymmetric than during times of higher magnetic activity. The assumption of axisymmetry is clearly not valid for eruptive phenomena even during solar minimum conditions. Therefore, depending on the application, an evaluation of the effect of the symmetry on the dynamics needs to be conducted. For the calculations presented in the previous section, this can be done by repeating the solar wind solution in the azimuthal direction and specifying the 3-D realization of the eruptive structure, as described in section 3.5.1.

Figure 5.6 shows the result of such a three-dimensional experiment corresponding to the two axisymmetric cases in Fig. 5.5. In the plotted meridional plane, the initial conditions are identical to those in the axisymmetric case. While the overall dynamics is similar, there are indeed noticeable differences. In the three-dimensional setting, the shock strength is consistently smaller along the entire front. The front as a whole is more bow shock-like than the quasi-circular shape in the axisymmetric case. Both effects can be attributed to the fact that the plasma is no longer forced to deflect only in the north-south direction as in the axisymmetric case, but can also flow in the azimuthal direction. The effect of the distribution of the energy over a larger area is most clearly visible in the temperature plots for the case of an adiabatic polytropic index. In the axisymmetric case, the shock downstream is heated to temperatures beyond 10 MK for a large area, while in the three-dimensional case only the shock nose is heated to corresponding temperatures.

The way in which the erupting Sun-encircling torus-structure in the axisymmetric case is extended in the azimuthal direction in the three-dimensional case naturally affects the solution considerably. It is conceivable that by a variation of the parameters of the model CME, a better correspondence could be achieved. In fact, an investigation along these lines has been conducted by Jacobs et al. (2007) for the case of a purely hydrodynamical model CME. A motivation for such an undertaking is the need for very high resolution of the shock structure arising, for

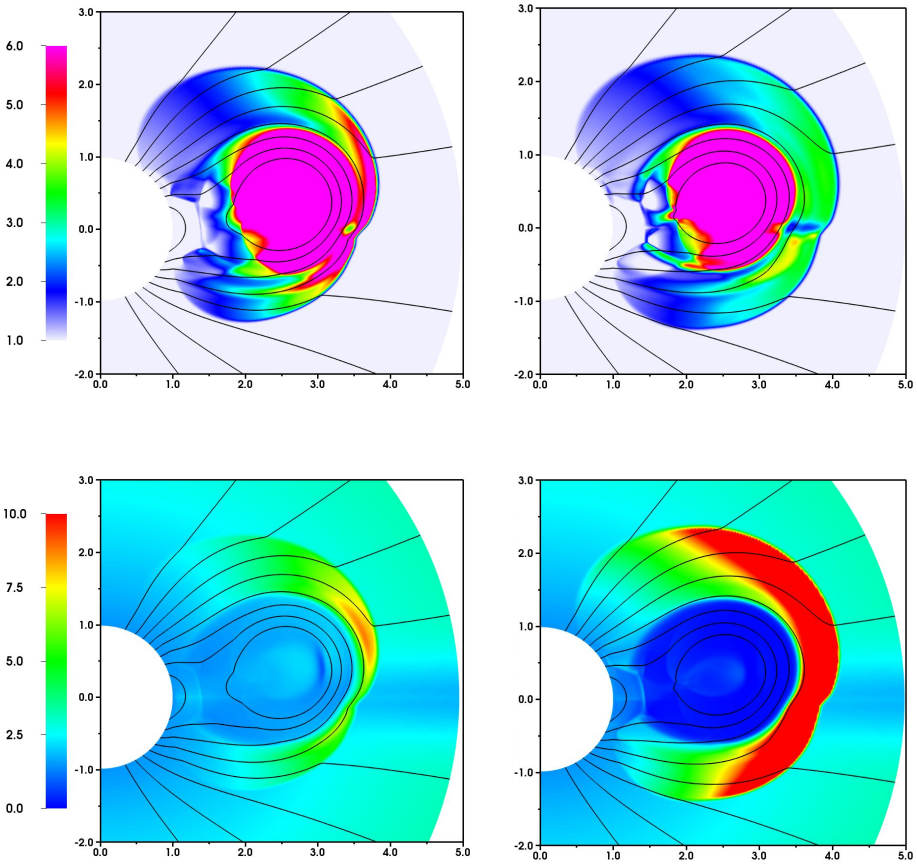

Figure 5.5: Top: Compression ratio r_c. Bottom: Temperature in units of MK. Left images show the results for wind model P1, while the right images for P2. All images are at $t = 20$ min after onset. Note the clipping of the palette.

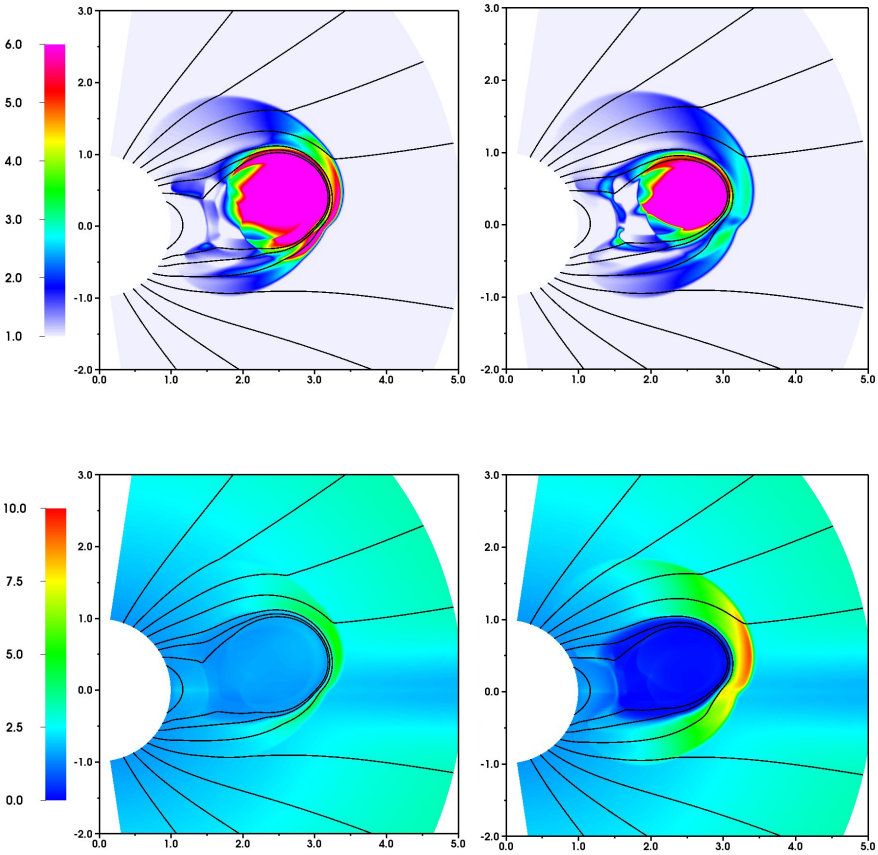

Figure 5.6: Same as Fig. 5.5 presented for the three-dimensional generalization.

instance, if the MHD simulation data is used as input to kinetic simulations.

5.6 Implications for particle acceleration

Although magnetohydrodynamic simulations naturally cannot directly address the ability of the shock to produce energetic particles, a qualitative assessment by comparing to known theoretical results is nevertheless worthwhile.

A feature common in closed field regions for both the local and global models is the appearance of a collapsing trap in which an upstream field line becomes connected to the shock at two points. Such a geometry has been found favorable for particle acceleration (Sandroos and Vainio, 2006). In the local model, this happens so that the part of the field line left upstream is in the region of the laterally expanding part of the shock. In fact, the footpoints of these field lines map to the surface a distance outward from the field lines connecting to the reconnecting current sheet. Therefore, if the current sheet is assumed to predominantly accelerate electrons and the shock accelerates ions, the geometry is consistent with gamma rays being emitted outside of the hard X-ray sources, as has been observed by the Reuven Ramaty High Energy Solar Spectroscopic Imager (RHESSI) (Lin et al., 2003) (see also discussion in Article I).

An example of the collapsing trap configuration in the global setting can be seen in Fig. 5.7 (right) for the outermost closed field line. The evolution of the shock obliquity for that field line is interesting: the shock starts with a quasi-parallel phase which is followed by a quasi-perpendicular phase. Performing test-particle simulations, Sandroos and Vainio (2009a) found that in the first quasi-parallel phase, due to the lower injection threshold, the shock injects thermal particles to the acceleration process which the quasi-perpendicular phase can accelerate efficiently. In fact, in their model, Sandroos and Vainio (2009b) found acceleration to the highest energies for such geometries.

The asymmetry of the eruption causes an interesting effect when comparing the potential acceleration sites on open field lines for the two hemispheres. In the north, the shock reaches the open field lines very quickly, and remains quasi-parallel for the field lines closest to the equator. South of the current sheet, however, the shock reaches the open field lines almost an hour into the event and experiences a longer quasi-perpendicular phase. Therefore, particle emission from the south would be delayed, but could nonetheless produce a larger event due to the more favorable geometry.

These results show that, even under relatively simple coronal conditions, a non-trivial evolution of the shock properties on coronal field lines occurs. Therefore, the evolution of parameters most crucial to particle acceleration at shocks, such as the compression ratio and obliquity, need to be more accurately taken into account in models and simulations of particle acceleration than has been customary.

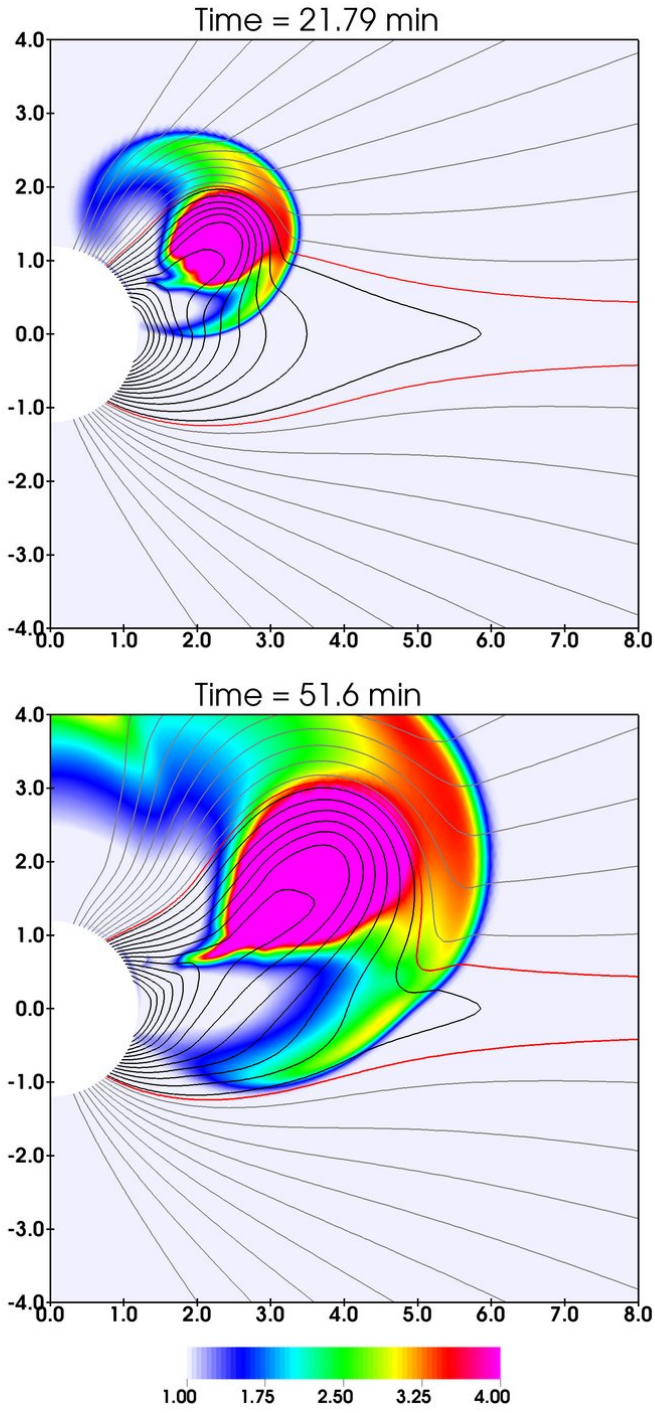

Figure 5.7: r_c at two times separated by roughly half an hour. Black curves show closed magnetic field lines, while gray curves show open field lines. The red curves indicate the boundary between open and closed fields. The colorbar is the same in both images.

Chapter 6

Conclusions

6.1 Summary and conclusions

In this thesis, a study of the characteristics of large-amplitude waves and shocks occurring in the solar corona as a response to eruptive phenomena has been conducted. The method chosen for the task was that of fluid plasma simulations. The goal of the work was to construct a magnetohydrodynamic simulation tool capable of modeling the complex CME-induced dynamics for eruptions taking place in realistic pre-event configurations. To this end, the project has been a success. The main findings can be summarized as follows:

- The MHD models are able to qualitatively reproduce many features observed during the CME lift-off such as shock domes in front of the ejecta connecting to a wave resembling an EIT-wave sweeping the surface in addition to a cavity region surrounding the flux rope.
- The event-oriented simulation is able to reach a high level of agreement with the EUV observations. The evolution of the skirt of the shock resembles very closely the evolution of the EIT wave, and a spherical shock structure similar in morphology to the EUV dome is produced.
- The shock dynamics is often complex: depending on the variations in the Alfvén speed in the corona, the ejection can at times act as the driver of the shock, while at other times the shock may propagate freely. Failed eruptions also have the potential of launching coronal waves.
- Comparing with recent test particle simulations, highly interesting and non-trivial evolution of shock geometries with the potential for efficient particle acceleration were found. Models of particle acceleration that more accurately take into account the evolution of parameters most crucial to particle acceleration need to be constructed.

- The method by which momentum and energy is added in order to achieve a realistic solar wind solution in MHD simulations significantly alters the properties and dynamics of shocks in the low corona. An equivalent heating formulation yielding shock properties consistent with theory and available coronal shock observations was developed.

- The same mathematical framework used to derive a robust semi-discrete finite volume scheme for hyperbolic conservation laws in orthogonal curvilinear coordinates can be used to derive an upwinded non-oscillatory constrained transport scheme for divergence-free vector fields. In particular, a prescription of an arbitrary-order scheme was obtained.

6.2 Future prospects

The work presented in this thesis could be expanded in a natural way in several directions. Starting from the low corona, a more realistic modeling of the thermodynamics, in which anisotropic heat conduction as well as radiative losses are included, is needed. Only then can synthetic line-of-sight EUV images taking into account instrument response functions be produced that can directly be compared on a quantitative level to observations. Such models have been pursued by Lionello et al. (2009), Downs et al. (2010). The fundamental unsolved problem of coronal heating must be circumvented in some manner in such modeling. The works above apply purely empirical source terms that include a number of free parameters that need to be tuned in order to reach an agreement with the observations. Finding the appropriate parameters is, however, an arduous and time-consuming task that currently limits the applicability of such models to selected case studies.

The coronal heating problem is most relevant to the solar wind modeling too. The current state of the art MHD solar wind models of the inner heliosphere utilize the empirical WSA model as the basis from which the amount of required heating is derived. The latest idea is to use the WSA model to provide boundary conditions for the Alfvén wave pressure in an MHD model including WKB Alfvén waves in order to obtain realistic values of the solar wind at 1 AU (van der Holst et al., 2010). It is interesting to note that although WKB Alfvén waves have been included in multidimensional MHD models for more than a decade, models that relax the WKB assumption and instead consider a spectrum of waves have not yet been constructed.

A significant idealization in the current MHD models of CMEs is the method by which the eruption is generated. Although the use of velocity fields obtained directly from sequences of observed (vector) magnetograms have been identified as a crucial ingredient for more realistic simulations, attempts at such calculations have not yet been reported. With increasing computational resources as well as

developments in the observational methods, such calculations can be expected in the coming years.

Looking further into the future, global multi-fluid models are a viable option for going beyond (ideal) MHD. Such models are, however, not only extremely challenging from a computational point-of-view but also theoretically not as well understood.

In the meantime, the time is ripe for coupled models that can significantly narrow the gap between fluid and particle descriptions. Indeed, a highly valuable tool not only for fundamental physics but also for space weather applications would be coupling MHD modeling with (test-)particle simulations.

Nevertheless, the primary driver of breakthroughs in the understanding of the nature of solar coronal phenomena has been, and will be, the implementation of new experiments. With new data, new directions of inquiry have ensued. Yet, with advancements in the theoretical understanding and improvements of the numerical simulations, model calculations are – in a future not too distant – approaching a state of maturity where they have the potential to offer new insights and, subsequently, clues of signatures to look for in multiwavelength data.

Appendix A

Details of the Model Initial Configurations

In this appendix, details of the additional modeling work conducted for the introduction part of the thesis are given.

A.1 Local model

The configuration of the two-dimensional local model presented in section 3.3 is described next. The coordinate system is chosen so that x is the horizontal coordinate running along the solar surface, y is the vertical coordinate increasing upward with $y = 0$ the bottom of the simulation (the coronal base), and z is parallel to the invariant axis.

The magnetic vector potential of a straight circular line current of radius R carrying a uniformly distributed current I is obtained from Ampère's law as

$$\mathbf{A}_{\rm in}(x, y; I, R, x_0, y_0) = -\frac{\mu_0 I}{4\pi}\left(\frac{r}{R}\right)^2 \mathbf{e}_z \tag{A.1}$$

where $r^2 = (x - x_0)^2 + (y - y_0)^2$ and (x_0, y_0) is the center of the line current. On the other hand, the magnetic vector potential of the magnetic field produced by an infinitely thin line current is given by

$$\mathbf{A}_{\rm out}(x, y; I, L, x_0, y_0) = -\frac{\mu_0 I}{4\pi}\left[1 + \ln\left(\frac{r}{L}\right)^2\right] \mathbf{e}_z \tag{A.2}$$

where an arbitrary constant L with dimensions of length has been included.

The magnetic field of the flux rope in the local model is chosen as

$$\mathbf{B}_{\rm fr} = \nabla \times \mathbf{A}_{\rm fr} + B_z \mathbf{e}_z \tag{A.3}$$

with

$$\mathbf{A}_{\rm fr}(x,y;I,R,h) = \begin{cases} \mathbf{A}_{\rm in}(x,y;I,R,0,h), & r \le R \\ \mathbf{A}_{\rm out}(x,y;I,R,0,h), & r > R \end{cases} \tag{A.4}$$

where h is the height of the flux rope above the surface. The toroidal field component is chosen so that the field is exactly force-free, and is given by

$$B_z = \begin{cases} -\frac{\mu_0 I}{2\pi R}\sqrt{2\left(1-\left(\frac{r}{R}\right)^2\right)}, & r \le R \\ 0, & r > R \end{cases} \tag{A.5}$$

Note that, in contrast to the force-free field in the model currently under consideration, in Article I the force balance is achieved by adjusting the density distribution inside the flux rope (see Eq. (9) in Article I).

The flux rope is embedded in a background magnetic field. First, in order for the background field to determine the component of the magnetic field normal to the surface at the surface, an image field $\mathbf{B}_{\rm i}$ is added. This is accomplished when the vector potential of the flux rope plus image current at $y = 0$ is a constant, giving

$$\mathbf{B}_{\rm i} = \nabla \times \mathbf{A}_{\rm out}(x,y;-I,R,0,-h). \tag{A.6}$$

Note that this assumes that $h > R$. The background field consists of four line currents, $\mathbf{B}_{\rm bg} = \nabla \times \mathbf{A}_{\rm bg}$, with

$$\begin{aligned} \mathbf{A}_{\rm bg} = {} & \mathbf{A}_{\rm out}(x,y;I_{\rm bg},R,x_{{\rm bg};1},y_{\rm bg}) + \mathbf{A}_{\rm out}(x,y;I_{\rm bg},R,-x_{{\rm bg};1},y_{\rm bg}) \\ & + \mathbf{A}_{\rm out}(x,y;-I_{\rm bg},R,x_{{\rm bg};2},y_{\rm bg}) + \mathbf{A}_{\rm out}(x,y;-I_{\rm bg},R,-x_{{\rm bg};2},y_{\rm bg}). \end{aligned} \tag{A.7}$$

The choice of the background current $I_{\rm bg}$ is subtle: it should balance the upward-directed Lorentz force exerted by the magnetic field of the image current on the flux rope so that the system remains in approximate equilibrium also when the background field and image field are present. The latter two produce contributions to the magnetic field at the flux rope that are roughly horizontal but oppositely directed. At $x = 0$ the field is exactly horizontal. If $I_{\rm bg}$ if is chosen such that the horizontal components vanish, the equilibrium is retained. Enforcing this at the flux rope center at $(x,y) = (0,h)$ gives the background current

$$I_{\rm bg} = \frac{I}{4}\frac{\left(x_{{\rm bg};1}^2 + (h-y_{\rm bg})^2\right)\left(x_{{\rm bg};2}^2 + (h-y_{\rm bg})^2\right)}{h(h-y_{\rm bg})(x_{{\rm bg};2}^2 - x_{{\rm bg};1}^2)}. \tag{A.8}$$

Since $\mathbf{v} = 0$ and the magnetic field is (approximately) force-free, the pressure gradient force should cancel gravity. Choosing the initial temperature to be uniform and applying the ideal gas law $P = (\rho/m)k_{\rm B}T_0$, the force balance results in an exponentially decreasing density

$$\rho(x,y) = \rho_0 \exp(-y/H) \tag{A.9}$$

where $H = k_{\mathrm{B}}T_0/mg_\odot$ is the scale height.

Finally, the eruption is driven by imposing an artificial force acting on the flux rope. This is done by adding an external force density $\mathbf{f}_{\mathrm{acc}}$ to the equations: (see Eq. (3.2) and Eq. (3.3))

$$\mathbf{f}_{\mathrm{acc}} = \begin{cases} a(t)\cos\left(\frac{\pi}{2}\cdot\frac{A_{z;\mathrm{c}}-A_z}{A_{z;\mathrm{c}}-A_{z;\mathrm{acc}}}\right)\mathrm{sgn}(v_{\mathrm{fr}}-v_y), & A_z < A_{z;\mathrm{acc}} \text{ and } y > y_{\mathrm{above}} \\ 0, & \text{otherwise} \end{cases} \tag{A.10}$$

Here, A_z is the z-component of the magnetic vector potential, $A_{z;\mathrm{c}}$ is the value of the vector potential at the flux rope center in the initial configuration, $A_{z;\mathrm{acc}}$ is the value of the vector potential that defines the boundary within which the force should act and at a height above y_{above}, v_y is the velocity in the y-direction, v_{fr} is the velocity that the flux rope should attain and $a(t) = a_0 + ta_1$ is the acceleration.

All quantities at the boundaries were kept fixed to the initial values except at the $y = 0$ boundary where B_x in the ghost cell was chosen so that the z-component of the current density $J_z(x, y = 0) = 0$ while all other quantities were held fixed.

The parameters of the simulation are given in table A.1. Furthermore, in the confined eruption simulation, for times $t > t_{\mathrm{dec}}$ the aritificial force is altered by changing the parameters so that $a(t) = a_0 + t_{\mathrm{dec}}a_1$ and $v_{\mathrm{fr}} = 0$. The time when the rapid deceleration started was $t_{\mathrm{dec}} = 70$ s.

A.2 Event-oriented model

The background configuration of the event-oriented model was detailed in section 3.5.2. In this section, the construction of the non-equilibrium flux rope is described.

The starting point is the flux rope configuration detailed in Titov and Démoulin (1999), hereafter denoted TD99. Removing the subphotospheric line current as well as the magnetic charges results in a flux rope with a rotational symmetry produced by a ring current I. The poloidal field is given by $\mathbf{B}_p = \nabla \times \left(A_I\hat{\boldsymbol{\theta}}\right)$ where A_I is given by Eq. (31) in TD99, and the toroidal unit vector $\hat{\boldsymbol{\theta}}$ by Eq. (17) in TD99. The toroidal field is given by Eq. (16) in TD99 with the contribution of the line current removed:

$$\mathbf{B}_t = \begin{cases} \frac{\mu_0 I}{2\pi a}\sqrt{2\left(1-\left(\frac{\rho}{a}\right)^2\right)}\hat{\boldsymbol{\theta}}, & \rho \le a \\ 0, & \rho > a \end{cases} \tag{A.11}$$

where ρ is the distance from the center of the ring current and given by Eq. (18) in TD99, and a is the thickness (minor radius) of the flux rope. Note the similarity to Eq. (A.5).

Parameter	Value
ρ_0	$1.67 \cdot 10^{-13}$ kg/m^3
T_0	$1.5 \cdot 10^6$ K
I	$-2.5 \cdot 10^{10}$ A
R	$0.5 l_0$
h	$2 l_0$
$x_{\mathrm{bg};1}$	$0.3 l_0$
$x_{\mathrm{bg};2}$	$1.5 l_0$
y_{bg}	$-0.3 l_0$
v_{fr}	200 km/s
a_0	0
a_1	1000 m/s^3
y_{above}	l_0
$A_{z;\mathrm{c}}$	$-0.2 A_0$
$A_{z;\mathrm{acc}}$	$-0.15 A_0$
A_0	69550 Tm
l_0	10 Mm
m	$0.6 m_p$
γ	$5/3$

Parameter	Value
I	$-2 \cdot 10^{11}$ A
R	$0.12 R_\odot$
a	$0.03 R_\odot$
d	$0.02 R_\odot$
α_x	1.95 rad
α_y	0.05 rad
α_z	-1.55 rad

Table A.1: Left: parameters for the local model. Top: parameters for the flux rope in the event-oriented model.

The flux rope needs to be rotated and translated to the specified position, in this case NOAA AR 11226. This is done by transforming the (Sun-centered Cartesian) (x, y, z) system to a new (x', y', z') system. This is obtained by rotating the system by angles $\alpha_x, \alpha_y, \alpha_z$ about the z,y and x axis, respectively, after which a translation in the new z-direction by an amount $R_\odot$ is perfomed. In the new primed system, the equations given above are applied, and the resulting magnetic field is then transformed back to the original unprimed system.

The parameters were chosen as given in table A.1. In the table, R is the major radius of the flux rope and d is the distance of the flux rope symmetry axis to the surface.

Bibliography

C. N. Arge and V. J. Pizzo. Improvement in the prediction of solar wind conditions using near-real time solar magnetic field updates. *Journal of Geophysical Research*, 105:10465–10480, 2000. doi: 10.1029/1999JA000262.

A. Asai, T. T. Ishii, H. Isobe, R. Kitai, K. Ichimoto, S. UeNo, S. Nagata, S. Morita *et al.* First Simultaneous Observation of an Hα Moreton Wave, EUV Wave, and Filament/Prominence Oscillations. *Astrophysical Journal Letters*, 745:L18, 2012. doi: 10.1088/2041-8205/745/2/L18.

K. S. Balasubramaniam, E. W. Cliver, A. Pevtsov, M. Temmer, T. W. Henry, H. S. Hudson, S. Imada, A. G. Ling *et al.* On the Origin of the Solar Moreton Wave of 2006 December 6. *Astrophysical Journal*, 723:587–601, 2010. doi: 10.1088/0004-637X/723/1/587.

S. D. Bale, M. J. Reiner, J.-L. Bougeret, M. L. Kaiser, S. Krucker, D. E. Larson, and R. P. Lin. The source region of an interplanetary type II radio burst. *Geophysical Research Letters*, 26:1573–1576, 1999. doi: 10.1029/1999GL900293.

D. S. Balsara. Second-Order-accurate Schemes for Magnetohydrodynamics with Divergence-free Reconstruction. *Astrophysical Journal Supplement*, 151:149–184, 2004. doi: 10.1086/381377.

D. S. Balsara and D. S. Spicer. A Staggered Mesh Algorithm Using High Order Godunov Fluxes to Ensure Solenoidal Magnetic Fields in Magnetohydrodynamic Simulations. *Journal of Computational Physics*, 149(2):270 – 292, 1999. doi: 10.1006/jcph.1998.6153.

D. S. Balsara, C. Altmann, C.-D. Munz, and M. Dumbser. A sub-cell based indicator for troubled zones in RKDG schemes and a novel class of hybrid RKDG+HWENO schemes. *Journal of Computational Physics*, 226(1):586 – 620, 2007. doi: 10.1016/j.jcp.2007.04.032.

D. S. Balsara, T. Rumpf, M. Dumbser, and C.-D. Munz. Efficient, high accuracy ADER-WENO schemes for hydrodynamics and divergence-free magnetohydrodynamics. *Journal of Computational Physics*, 228(7):2480 – 2516, 2009. doi: 10.1016/j.jcp.2008.12.003.

D. S. Balsara, C. Meyer, M. Dumbser, H. Du, and Z. Xu. Efficient Implementation of ADER Schemes for Euler and Magnetohydrodynamical Flows on Structured Meshes – Comparison with Runge-Kutta Methods. *ArXiv e-prints*, 2010. URL: `http://arxiv.org/abs/1006.2146`.

A. Bemporad and S. Mancuso. First Complete Determination of Plasma Physical Parameters Across a Coronal Mass Ejection-driven Shock. *Astrophysical Journal*, 720:130–143, 2010. doi: 10.1088/0004-637X/720/1/130.

M. Berger, M. J. Aftosmis, and S. M. Murman. Analysis of slope limiters on irregular grids. *NAS Technical Report*, NAS-05-007, 2005.

I. H. Cairns. Coherent Radio Emissions Associated with Star System Shocks. In M. P. Miralles and J. Sánchez Almeida, editors, *The Sun, the Solar Wind, and the Heliosphere*, 2011.

H. V. Cane, R. A. Mewaldt, C. M. S. Cohen, and T. T. von Rosenvinge. Role of flares and shocks in determining solar energetic particle abundances. *Journal of Geophysical Research (Space Physics)*, 111(A10):A06S90, 2006. doi: 10.1029/2005JA011071.

J. Casper and H. Atkins. A finite-volume high-order eno scheme for two-dimensional hyperbolic systems. *Journal of Computational Physics*, 106(1): 62 – 76, 1993. doi: 10.1006/jcph.1993.1091.

E. Chané, C. Jacobs, B. van der Holst, S. Poedts, and D. Kimpe. On the effect of the initial magnetic polarity and of the background wind on the evolution of CME shocks. *Astronomy and Astrophysics*, 432:331–339, 2005. doi: 10.1051/0004-6361:20042005.

P. F. Chen. Coronal Mass Ejections: Models and Their Observational Basis. *Living Reviews in Solar Physics*, 8:1, 2011. URL: `http://www.livingreviews.org/lrsp-2011-1`.

P. F. Chen and K. Shibata. An Emerging Flux Trigger Mechanism for Coronal Mass Ejections. *Astrophysical Journal*, 545:524–531, 2000. doi: 10.1086/317803.

X. Cheng, J. Zhang, O. Olmedo, A. Vourlidas, M. D. Ding, and Y. Liu. Investigation of the Formation and Separation of an Extreme-ultraviolet Wave from the Expansion of a Coronal Mass Ejection. *Astrophysical Journal Letters*, 745:L5, 2012. doi: 10.1088/2041-8205/745/1/L5.

O. Cohen, I. V. Sokolov, I. I. Roussev, and T. I. Gombosi. Validation of a synoptic solar wind model. *Journal of Geophysical Research (Space Physics)*, 113 (A12):A03104, 2008. doi: 10.1029/2007JA012797.

S. R. Cranmer. Self Consistent Models of the Solar Wind. *ArXiv e-prints*, 2010. URL: `http://arxiv.org/abs/1007.0954`.

A. Dedner, F. Kemm, D. Kröner, C.-D. Munz, T. Schnitzer, and M. Wesenberg. Hyperbolic Divergence Cleaning for the MHD Equations. *Journal of Computational Physics*, 175(2):645 – 673, 2002. doi: 10.1006/jcph.2001.6961.

H. W. Dodson. Position and Development of the Solar Flares of may 8 and 10, 1949. *Astrophysical Journal*, 110:382, 1949. doi: 10.1086/145214.

C. Downs, I. I. Roussev, B. van der Holst, N. Lugaz, I. V. Sokolov, and T. I. Gombosi. Toward a Realistic Thermodynamic Magnetohydrodynamic Model of the Global Solar Corona. *Astrophysical Journal*, 712:1219–1231, 2010. doi: 10.1088/0004-637X/712/2/1219.

C. Downs, I. I. Roussev, B. van der Holst, N. Lugaz, I. V. Sokolov, and T. I. Gombosi. Studying Extreme Ultraviolet Wave Transients with a Digital Laboratory: Direct Comparison of Extreme Ultraviolet Wave Observations to Global Magnetohydrodynamic Simulations. *Astrophysical Journal*, 728:2, 2011. doi: 10.1088/0004-637X/728/1/2.

M. Dumbser and C.-D. Munz. Building Blocks for Arbitrary High Order Discontinuous Galerkin Schemes. *Journal of Scientific Computing*, 27:215–230, 2006. doi: 10.1007/s10915-005-9025-0.

M. Dumbser, M. Käser, V. A. Titarev, and E. F. Toro. Quadrature-free non-oscillatory finite volume schemes on unstructured meshes for nonlinear hyperbolic systems. *Journal of Computational Physics*, 226(1):204 – 243, 2007. doi: 10.1016/j.jcp.2007.04.004.

M. Dumbser, D. S. Balsara, E. F. Toro, and C.-D. Munz. A unified framework for the construction of one-step finite volume and discontinuous Galerkin schemes on unstructured meshes. *Journal of Computational Physics*, 227(18):8209 – 8253, 2008. doi: 10.1016/j.jcp.2008.05.025.

C. R. Evans and J. F. Hawley. Simulation of magnetohydrodynamic flows - A constrained transport method. *Astrophysical Journal*, 332:659–677, 1988. doi: 10.1086/166684.

R. M. Evans, M. Opher, W. B. Manchester, IV, and T. I. Gombosi. Alfvén Profile in the Lower Corona: Implications for Shock Formation. *Astrophysical Journal*, 687:1355–1362, 2008. doi: 10.1086/592016.

T. G. Forbes, J. A. Linker, J. Chen, C. Cid, J. Kóta, M. A. Lee, G. Mann, Z. Mikić *et al.* CME Theory and Models. *Space Science Reviews*, 123:251–302, 2006. doi: 10.1007/s11214-006-9019-8.

P. T. Gallagher and D. M. Long. Large-scale Bright Fronts in the Solar Corona: A Review of "EIT waves". *Space Science Reviews*, 158:365–396, 2011. doi: 10.1007/s11214-010-9710-7.

T. A. Gardiner and J. M. Stone. An unsplit Godunov method for ideal MHD via constrained transport. *Journal of Computational Physics*, 205(2):509 – 539, 2005. doi: 10.1016/j.jcp.2004.11.016.

T. I. Gombosi, G. Tóth, D. L. D. Zeeuw, K. C. Hansen, K. Kabin, and K. G. Powell. Semirelativistic magnetohydrodynamics and physics-based convergence acceleration. *Journal of Computational Physics*, 177(1):176 – 205, 2002. doi: 10.1006/jcph.2002.7009.

N. Gopalswamy, N. Nitta, S. Akiyama, P. Mäkelä, and S. Yashiro. Coronal Magnetic Field Measurement from EUV Images Made by the Solar Dynamics Observatory. *Astrophysical Journal*, 744:72, 2012. doi: 10.1088/0004-637X/744/1/72.

S. Gottlieb, D. Ketcheson, and C.-W. Shu. High Order Strong Stability Preserving Time Discretizations. *Journal of Scientific Computing*, 38:251–289, 2009. doi: 10.1007/s10915-008-9239-z.

K. F. Gurski. An HLLC-Type Approximate Riemann Solver for Ideal Magnetohydrodynamics. *SIAM Journal on Scientific Computing*, 25(6):2165–2187, 2004. doi: 10.1137/S1064827502407962.

A. Harten. High resolution schemes for hyperbolic conservation laws. *Journal of Computational Physics*, 49(3):357 – 393, 1983. doi: 10.1016/0021-9991(83)90136-5.

A. Harten, P. Lax, and B. van Leer. On Upstream Differencing and Godunov-Type Schemes for Hyperbolic Conservation Laws. *SIAM Review*, 25(1):35–61, 1983. doi: 10.1137/1025002.

J. V. Hollweg and P. A. Isenberg. Generation of the fast solar wind: A review with emphasis on the resonant cyclotron interaction. *Journal of Geophysical Research (Space Physics)*, 107:1147, 2002. doi: 10.1029/2001JA000270.

C. Jacobs, S. Poedts, B. Van der Holst, and E. Chané. On the effect of the background wind on the evolution of interplanetary shock waves. *Astronomy and Astrophysics*, 430:1099–1107, 2005. doi: 10.1051/0004-6361:20041676.

C. Jacobs, B. van der Holst, and S. Poedts. Comparison between 2.5D and 3D simulations of coronal mass ejections. *Astronomy and Astrophysics*, 470:359–365, 2007. doi: 10.1051/0004-6361:20077305.

H. Ji, H. Wang, E. J. Schmahl, Y.-J. Moon, and Y. Jiang. Observations of the Failed Eruption of a Filament. *Astrophysical Journal Letters*, 595:L135–L138, 2003. doi: 10.1086/378178.

M. Jin, W. B. Manchester, B. van der Holst, J. R. Gruesbeck, R. A. Frazin, E. Landi, A. M. Vasquez, P. L. Lamy *et al.* A Global Two-temperature Corona and Inner Heliosphere Model: A Comprehensive Validation Study. *Astrophysical Journal*, 745:6, 2012. doi: 10.1088/0004-637X/745/1/6.

I. W. Kienreich, M. Temmer, and A. M. Veronig. STEREO Quadrature Observations of the Three-Dimensional Structure and Driver of a Global Coronal Wave. *Astrophysical Journal Letters*, 703:L118–L122, 2009. doi: 10.1088/0004-637X/703/2/L118.

I. W. Kienreich, A. M. Veronig, N. Muhr, M. Temmer, B. Vršnak, and N. Nitta. Case Study of Four Homologous Large-scale Coronal Waves Observed on 2010 April 28 and 29. *Astrophysical Journal Letters*, 727:L43, 2011. doi: 10.1088/2041-8205/727/2/L43.

R.-S. Kim, N. Gopalswamy, Y.-J. Moon, K.-S. Cho, and S. Yashiro. Magnetic Field Strength in the Upper Solar Corona Using White-light Shock Structures Surrounding Coronal Mass Ejections. *Astrophysical Journal*, 746:118, 2012. doi: 10.1088/0004-637X/746/2/118.

B. Klecker, H. Kunow, H. V. Cane, S. Dalla, B. Heber, K. Kecskemety, K.-L. Klein, J. Kota *et al.* Energetic Particle Observations. *Space Science Reviews*, 123:217–250, 2006. doi: 10.1007/s11214-006-9018-9.

S. A. Knock, I. H. Cairns, P. A. Robinson, and Z. Kuncic. Theory of type II radio emission from the foreshock of an interplanetary shock. *Journal of Geophysical Research*, 106:25041–25052, 2001. doi: 10.1029/2001JA000053.

K. A. Kozarev, K. E. Korreck, V. V. Lobzin, M. A. Weber, and N. A. Schwadron. Off-limb Solar Coronal Wavefronts from SDO/AIA Extreme-ultraviolet Observations: Implications for Particle Production. *Astrophysical Journal Letters*, 733:L25, 2011. doi: 10.1088/2041-8205/733/2/L25.

A. Kurganov, S. Noelle, and G. Petrova. Semidiscrete central-upwind schemes for hyperbolic conservation laws and Hamilton-Jacobi equations. *SIAM Journal on Scientific Computing*, 23(3):707–740, 2002. doi: 10.1137/S1064827500373413.

R. J. LeVeque. *Finite-Volume Methods for Hyperbolic Problems*. Cambridge University Press, 2002.

S. Li. An HLLC Riemann solver for magneto-hydrodynamics. *Journal of Computational Physics*, 203(1):344 – 357, 2005. doi: 10.1016/j.jcp.2004.08.020.

T. Li, J. Zhang, S. Yang, and W. Liu. SDO/AIA Observations of Secondary Waves Generated by Interaction of the 2011 June 7 Global EUV Wave with Solar Coronal Structures. *Astrophysical Journal*, 746:13, 2012. doi: 10.1088/0004-637X/746/1/13.

R. P. Lin, S. Krucker, G. J. Hurford, D. M. Smith, H. S. Hudson, G. D. Holman, R. A. Schwartz, B. R. Dennis *et al.* RHESSI Observations of Particle Acceleration and Energy Release in an Intense Solar Gamma-Ray Line Flare. *Astrophysical Journal Letters*, 595:L69–L76, 2003. doi: 10.1086/378932.

R. Lionello, J. A. Linker, and Z. Mikić. Multispectral Emission of the Sun During the First Whole Sun Month: Magnetohydrodynamic Simulations. *Astrophysical Journal*, 690:902–912, 2009. doi: 10.1088/0004-637X/690/1/902.

C. Loesch, M. Opher, M. V. Alves, R. M. Evans, and W. B. Manchester. Signatures of two distinct driving mechanisms in the evolution of coronal mass ejections in the lower corona. *Journal of Geophysical Research (Space Physics)*, 116:A04106, 2011. doi: 10.1029/2010JA015582.

P. Londrillo and L. Del Zanna. High-Order Upwind Schemes for Multidimensional Magnetohydrodynamics. *Astrophysical Journal*, 530:508–524, 2000. doi: 10.1086/308344.

P. Londrillo and L. Del Zanna. On the divergence-free condition in Godunov-type schemes for ideal magnetohydrodynamics: the upwind constrained transport method. *Journal of Computational Physics*, 195(1):17 – 48, 2004. doi: 10.1016/j.jcp.2003.09.016.

D. M. Long, E. E. DeLuca, and P. T. Gallagher. The Wave Properties of Coronal Bright Fronts Observed Using SDO/AIA. *Astrophysical Journal Letters*, 741: L21, 2011. doi: 10.1088/2041-8205/741/1/L21.

S. Ma, J. C. Raymond, L. Golub, J. Lin, H. Chen, P. Grigis, P. Testa, and D. Long. Observations and Interpretation of a Low Coronal Shock Wave Observed in the EUV by the SDO/AIA. *Astrophysical Journal*, 738:160, 2011. doi: 10.1088/0004-637X/738/2/160.

T. Magara, P. Chen, K. Shibata, and T. Yokoyama. A Unified Model of Coronal Mass Ejection-related Type II Radio Bursts. *Astrophysical Journal Letters*, 538: L175–L178, 2000. doi: 10.1086/312813.

D. Maia, M. Pick, A. Vourlidas, and R. Howard. Development of Coronal Mass Ejections: Radio Shock Signatures. *Astrophysical Journal Letters*, 528:L49–L51, 2000. doi: 10.1086/312421.

G. Mann, T. Classen, and H. Aurass. Characteristics of coronal shock waves and solar type II radio bursts. *Astronomy and Astrophysics*, 295:775, 1995. URL: `http://adsabs.harvard.edu/abs/1995A%26A...295..775M`.

B. Merriman. Understanding the Shu-Osher Conservative Finite Difference Form. *Journal of Scientific Computing*, 19:309–322, 2003. doi: 10.1023/A:1025312210724.

T. Miyoshi and K. Kusano. A multi-state HLL approximate Riemann solver for ideal magnetohydrodynamics. *Journal of Computational Physics*, 208(1):315 – 344, 2005. doi: 10.1016/j.jcp.2005.02.017.

G. E. Moreton. Hα Observations of Flare-Initiated Disturbances with Velocities $\sim$1000 km/sec. *Astronomical Journal*, 65:494, 1960. doi: 10.1086/108346.

G. E. Moreton and H. E. Ramsey. Recent Observations of Dynamical Phenomena Associated with Solar Flares. *Publications of the Astronomical Society of the Pacific*, 72:357, 1960. URL: `http://adsabs.harvard.edu/abs/1960PASP...72..357M`.

G. F. Moreton. Hα Shock Wave and Winking Filaments with the Flare of 20 September 1963. *Astronomical Journal*, 69:145, 1964. doi: 10.1086/109375.

D. Moses, F. Clette, J.-P. Delaboudinière, G. E. Artzner, M. Bougnet, J. Brunaud, C. Carabetian, A. H. Gabriel *et al.* EIT Observations of the Extreme Ultraviolet Sun. *Solar Physics*, 175:571–599, 1997. doi: 10.1023/A:1004902913117.

N. Muhr, B. Vršnak, M. Temmer, A. M. Veronig, and J. Magdalenić. Analysis of a Global Moreton Wave Observed on 2003 October 28. *Astrophysical Journal*, 708:1639–1649, 2010. doi: 10.1088/0004-637X/708/2/1639.

A. Nindos, H. Aurass, K.-L. Klein, and G. Trottet. Radio Emission of Flares and Coronal Mass Ejections. Invited Review. *Solar Physics*, 253:3–41, 2008. doi: 10.1007/s11207-008-9258-9.

A. Nindos, C. E. Alissandrakis, A. Hillaris, and P. Preka-Papadema. On the relationship of shock waves to flares and coronal mass ejections. *Astronomy and Astrophysics*, 531:A31, 2011. doi: 10.1051/0004-6361/201116799.

V. Ontiveros and A. Vourlidas. Quantitative Measurements of Coronal Mass Ejection-Driven Shocks from LASCO Observations. *Astrophysical Journal*, 693:267–275, 2009. doi: 10.1088/0004-637X/693/1/267.

S. Patsourakos and A. Vourlidas. "Extreme Ultraviolet Waves" are Waves: First Quadrature Observations of an Extreme Ultraviolet Wave from STEREO. *Astrophysical Journal Letters*, 700:L182–L186, 2009. doi: 10.1088/0004-637X/700/2/L182.

S. Patsourakos and A. Vourlidas. On the Nature and Genesis of EUV Waves: A Synthesis of Observations from SOHO, STEREO, SDO, and Hinode. *ArXiv e-prints*, 2012. URL: `http://arxiv.org/abs/1203.1135`.

R. Payne-Scott, D. E. Yabsley, and J. G. Bolton. Relative Times of Arrival of Bursts of Solar Noise on Different Radio Frequencies. *Nature*, 160:256–257, 1947. doi: 10.1038/160256b0.

M. Pick, T. G. Forbes, G. Mann, H. V. Cane, J. Chen, A. Ciaravella, H. Cremades, R. A. Howard *et al.* Multi-Wavelength Observations of CMEs and Associated Phenomena. Report of Working Group F. *Space Science Reviews*, 123:341–382, 2006. doi: 10.1007/s11214-006-9021-1.

J. Qiu and C. Shu. On the Construction, Comparison, and Local Characteristic Decomposition for High-Order Central WENO Schemes. *Journal of Computational Physics*, 183(1):187 – 209, 2002. doi: 10.1006/jcph.2002.7191.

D. V. Reames. Particle acceleration at the Sun and in the heliosphere. *Space Science Reviews*, 90:413–491, 1999. doi: 10.1023/A:1005105831781.

A. Sandroos and R. Vainio. Particle acceleration at shocks propagating in inhomogeneous magnetic fields. *Astronomy and Astrophysics*, 455:685–695, 2006. doi: 10.1051/0004-6361:20054754.

A. Sandroos and R. Vainio. Reacceleration of Flare Ions in Coronal and Interplanetary Shock Waves. *Astrophysical Journal Supplement*, 181:183–196, 2009a. doi: 10.1088/0067-0049/181/1/183.

A. Sandroos and R. Vainio. Diffusive shock acceleration to relativistic energies in the solar corona. *Astronomy and Astrophysics*, 507:L21–L24, 2009b. doi: 10.1051/0004-6361/200913228.

M. Selwa, S. Poedts, and C. R. DeVore. Dome-shaped EUV Waves from Rotating Active Regions. *Astrophysical Journal Letters*, 747:L21, 2012. doi: 10.1088/2041-8205/747/2/L21.

F. Shen, X. S. Feng, S. T. Wu, C. Q. Xiang, and W. B. Song. Three-dimensional MHD simulation of the evolution of the April 2000 CME event and its induced shocks using a magnetized plasma blob model. *Journal of Geophysical Research (Space Physics)*, 116:4102, 2011. doi: 10.1029/2010JA015809.

C. Shu. High Order Weighted Essentially Nonoscillatory Schemes for Convection Dominated Problems. *SIAM Review*, 51(1):82 – 126, 2009. doi: 10.1137/070679065.

I. V. Sokolov, I. I. Roussev, T. I. Gombosi, M. A. Lee, J. Kóta, T. G. Forbes, W. B. Manchester, and J. I. Sakai. A New Field Line Advection Model for Solar Particle Acceleration. *Astrophysical Journal Letters*, 616:L171–L174, 2004. doi: 10.1086/426812.

A. Suresh and H. Huynh. Accurate Monotonicity-Preserving Schemes with Runge-Kutta Time Stepping. *Journal of Computational Physics*, 136:83–99, 1997. doi: 10.1006/jcph.1997.5745.

Z. Svestka. Solar flares. *Geophysics and Astrophysics Monographs*, 8, 1976.

P. K. Sweby. High Resolution Schemes Using Flux Limiters for Hyperbolic Conservation Laws. *SIAM Journal on Numerical Analysis*, 21(5):pp. 995–1011, 1984. doi: 10.1137/0721062.

M. Temmer, B. Vršnak, T. Žic, and A. M. Veronig. Analytic Modeling of the Moreton Wave Kinematics. *Astrophysical Journal*, 702:1343–1352, 2009. doi: 10.1088/0004-637X/702/2/1343.

B. J. Thompson, S. P. Plunkett, J. B. Gurman, J. S. Newmark, O. C. St. Cyr, and D. J. Michels. SOHO/EIT observations of an Earth-directed coronal mass ejection on May 12, 1997. *Geophysical Research Letters*, 25:2465–2468, 1998. doi: 10.1029/98GL50429.

B. J. Thompson, J. B. Gurman, W. M. Neupert, J. S. Newmark, J.-P. Delaboudinière, O. C. St. Cyr, S. Stezelberger, K. P. Dere *et al.* SOHO/EIT Observations of the 1997 April 7 Coronal Transient: Possible Evidence of Coronal Moreton Waves. *Astrophysical Journal Letters*, 517:L151–L154, 1999. doi: 10.1086/312030.

V. S. Titov and P. Démoulin. Basic topology of twisted magnetic configurations in solar flares. *Astronomy and Astrophysics*, 351:707–720, 1999. URL: `http://adsabs.harvard.edu/abs/1999A%26A...351..707T`.

T. Török and B. Kliem. Confined and Ejective Eruptions of Kink-unstable Flux Ropes. *Astrophysical Journal Letters*, 630:L97–L100, 2005. doi: 10.1086/462412.

G. Tóth, B. van der Holst, and Z. Huang. Obtaining Potential Field Solutions with Spherical Harmonics and Finite Differences. *Astrophysical Journal*, 732:102, 2011. doi: 10.1088/0004-637X/732/2/102.

T. Tran. *Improving the predictions of solar wind speed and interplanetary magnetic field at the Earth*. PhD thesis, University of California, Los Angeles, 2009. URL: `http://adsabs.harvard.edu/abs/2009PhDT.....13T`.

A. J. Tylka and M. A. Lee. A Model for Spectral and Compositional Variability at High Energies in Large, Gradual Solar Particle Events. *Astrophysical Journal*, 646:1319–1334, 2006. doi: 10.1086/505106.

A. J. Tylka, C. M. S. Cohen, W. F. Dietrich, M. A. Lee, C. G. Maclennan, R. A. Mewaldt, C. K. Ng, and D. V. Reames. Shock Geometry, Seed Populations, and the Origin of Variable Elemental Composition at High Energies in Large Gradual Solar Particle Events. *Astrophysical Journal*, 625:474–495, 2005. doi: 10.1086/429384.

A. J. Tylka, C. M. S. Cohen, W. F. Dietrich, M. A. Lee, C. G. Maclennan, R. A. Mewaldt, C. K. Ng, and D. V. Reames. A Comparative Study of Ion Characteristics in the Large Gradual Solar Energetic Particle Events of 2002 April 21 and 2002 August 24. *Astrophysical Journal Supplement*, 164:536–551, 2006. doi: 10.1086/503203.

Y. Uchida. Propagation of Hydromagnetic Disturbances in the Solar Corona and Moreton's Wave Phenomenon. *Solar Physics*, 4:30–44, 1968. doi: 10.1007/BF00146996.

B. van der Holst, W. B. Manchester, IV, R. A. Frazin, A. M. Vásquez, G. Tóth, and T. I. Gombosi. A Data-driven, Two-temperature Solar Wind Model with Alfvén Waves. *Astrophysical Journal*, 725:1373, 2010. doi: 10.1088/0004-637X/725/1/1373.

B. van Leer. Towards the ultimate conservative difference scheme. II. Monotonicity and conservation combined in a second-order scheme. *Journal of Computational Physics*, 14(4):361 – 370, 1974. doi: 10.1016/0021-9991(74)90019-9.

A. M. Veronig, M. Temmer, B. Vršnak, and J. K. Thalmann. Interaction of a Moreton/EIT Wave and a Coronal Hole. *Astrophysical Journal*, 647:1466–1471, 2006. doi: 10.1086/505456.

A. M. Veronig, N. Muhr, I. W. Kienreich, M. Temmer, and B. Vršnak. First Observations of a Dome-shaped Large-scale Coronal Extreme-ultraviolet Wave. *Astrophysical Journal Letters*, 716:L57–L62, 2010. doi: 10.1088/2041-8205/716/1/L57.

A. Vourlidas and V. Ontiveros. A Review of Coronagraphic Observations of Shocks Driven by Coronal Mass Ejections. In X. Ao and G. Z. R. Burrows, editors, *American Institute of Physics Conference Series*, volume 1183, pages 139–146, 2009. URL: `http://arxiv.org/abs/0908.1996`.

B. Vršnak and E. W. Cliver. Origin of Coronal Shock Waves. Invited Review. *Solar Physics*, 253:215–235, 2008. doi: 10.1007/s11207-008-9241-5.

A. Warmuth. Large-scale Waves and Shocks in the Solar Corona. In K.-L. Klein and A. MacKinnon, editors, *Lecture Notes in Physics, Berlin Springer Verlag*, volume 725, 2007. doi: 10.1007/978-3-540-71570-2_6.

A. Warmuth. Large-scale waves in the solar corona: The continuing debate. *Advances in Space Research*, 45:527–536, 2010. doi: 10.1016/j.asr.2009.08.022.

A. Warmuth. Globally propagating waves in the solar corona. *Plasma Physics and Controlled Fusion*, 53(12):124023, 2011. doi: 10.1088/0741-3335/53/12/124023.

A. Warmuth and G. Mann. A model of the Alfvén speed in the solar corona. *Astronomy and Astrophysics*, 435:1123–1135, 2005. doi: 10.1051/0004-6361:20042169.

A. Warmuth, B. Vršnak, J. Magdalenić, A. Hanslmeier, and W. Otruba. A multiwavelength study of solar flare waves. I. Observations and basic properties. *Astronomy and Astrophysics*, 418:1101–1115, 2004. doi: 10.1051/0004-6361:20034332.

J. P. Wild and L. L. McCready. Observations of the Spectrum of High-Intensity Solar Radiation at Metre Wavelengths. I. The Apparatus and Spectral Types of Solar Burst Observed. *Australian Journal of Scientific Research A Physical Sciences*, 3:387, 1950. URL: `http://adsabs.harvard.edu/abs/1950AuSRA...3..387W`.

M. J. Wills-Davey and G. D. R. Attrill. EIT Waves: A Changing Understanding over a Solar Cycle. *Space Science Reviews*, 149:325–353, 2009. doi: 10.1007/s11214-009-9612-8.

A. N. Zhukov. EIT wave observations and modeling in the STEREO era. *Journal of Atmospheric and Solar-Terrestrial Physics*, 73:1096–1116, 2011. doi: 10.1016/j.jastp.2010.11.030.

U. Ziegler. A central-constrained transport scheme for ideal magnetohydrodynamics. *Journal of Computational Physics*, 196(2):393 – 416, 2004. doi: 10.1016/j.jcp.2003.11.003.

U. Ziegler. A semi-discrete central scheme for magnetohydrodynamics on orthogonal-curvilinear grids. *Journal of Computational Physics*, 230(4):1035 – 1063, 2011. doi: 10.1016/j.jcp.2010.10.022.